2014

Applications of single molecule and nanoparticle imaging in chemical separation, photocatalysis, and drug delivery

Rui Han
Iowa State University

Applications of single molecule and nanoparticle imaging in chemical separation, photocatalysis, and drug delivery

by

Rui Han

A dissertation submitted to the graduate faculty

in partial fulfillment of the requirements for the degree of

DOCTOR OF PHILOSOPHY

Major: Analytical Chemistry

Program of Study Committee:
Ning Fang, Major Professor
Emily Smith
Robert Samuel Houk
Javier Vela
Liang Dong

Iowa State University

Ames, Iowa

2014

TABLE OF CONTENTS

ACKNOWLEDGEMENTS iii

CHAPTER 1. GENERAL INTRODUCTION 1
References 11
Figures 17

CHAPTER 2. ELECTROPHORETIC MIGRATION AND AXIAL DIFFUSION OF INDIVIDUAL NANOPARTICLES IN CYLINDRICAL NANOPORES 21
Abstract 21
Introduction 21
Experimental Section 23
Results and Discussion 26
Conclusion 35
References 36
Figures and Tables 39
Supplementary Information 46

CHAPTER 3. GOLD NANOPARTICLES AS DRUG DELIVERY VEHICLE AND IMAGING CONTRAST PROBES IN STEM CELLS PROLIFERATION . 50
Abstract 50
Introduction 50
Experimental Section 53
Results and Discussion 56
Conclusion 61
References 61
Figures 66

CHAPTER 4. GEOMETRY-ASSISTED THREE-DIMENSIONAL SUPER-LOCALIZATION IMAGING OF SINGLE MOLECULE CATALYSIS ON MODULAR MULTILAYER NANOCATALYSTS 76
Abstract 76
Introduction 76
Results and Discussion 78
Conclusion 84
References 85
Figures 88
Supporting Information 92

CHAPTER 5. GENERAL CONCLUSIONS 109

ACKNOWLEDGEMENTS

First, I would like to thank my advisor Ning Fang. In the last several years, Dr. Fang guided my research and scientific development as a good mentor and also encouraged me when my project progressed slowly and we discussed a lot to resolve the problem.

Also I would like to thank Dr. Edward S. Yeung. I worked with Dr. Yeung for my first two years before he was retired from Ames lab. It's a great research experience to work with Dr. Yeung. I also would like to thank Dr. Mary Jo Schmerr who encourage me to be a good researcher and also to be a good mother. I also want to thank to Dr. Jiwon Ha. Thanks a lot for his help on my research for last 3 years. We shared the same office, and when I was struggled on my stem cell project, he brought me to join the catalysis project. I learned a lot from Jiwon, not only on the knowledge, but how to be a good chemist and how to deal with the bad things in life. I also thank to Dr. Gufeng Wang. I worked with Gufeng on my first project, and he taught me a lot on my research. I also thank to Dr. Changbei Ma, when we were in cover co-lab, with Changbei's help, I got used to with the whole lab. Also Changbei gave me lots of good suggestions and comments on research and life.

I also would like to thank my committee members, Dr. Emily Smith, Dr. Javier Vela Dr. Robert Houk and Dr. Liang Dong, thanks for their guidance and support throughout the course of this research.

In addition, I would also like to thank my friends, colleagues, and my group members. Thanks to all my current and former group Changbei Ma, Wei Sun, Yong Luo, Chang Liu, Bin Dong, Shaobin Zhu, Kuangcai Chen, Ashley Augspurger, and Amanda Nguy.

At last, I want to thank my family. Thanks for my parents, my parents in law and my husband for their support and love.

CHAPTER 1. GENERAL INTRODUCTION

Dissertation Organization

This dissertation includes five chapters. Chapter 1 introduces single molecule and nanoparticle imaging techniques and their applications. Chapter 2 is a study of electrophoretic migration and axial diffusion of single nanoparticles in cylindrical nanopores in which the liquid viscosity was successfully measured. Chapter 3 reports the use of gold nanoparticles as drug delivery carriers and imaging contrast probes to study stem cell proliferation. This is an effort to maximize the capabilities of the recently developed plasmonic nanoparticle imaging techniques in stem cell research. Chapter 4 reports a study of single molecule catalysis on a modular multilayer catalytic platform and demonstrates three-dimensional super-localization imaging of single turnover events on 200-nm nanocatalysts. Chapter 5 summarizes all of the contents in the dissertation.

1. Introduction

Single molecule and nanoparticle detection allows one to examine the heterogeneity of individual molecules and nanoparticles and explore the information hidden in the ensemble experiments. After three decades of intensive development, single molecule and single nanoparticle optical imaging has matured and entered its prime time as an important experimental tool to interrogate chemical and biological systems.

This chapter introduces the applications of single molecule and single nanoparticle imaging, followed by the explanations of the principles of optical microscopy techniques employed in my research.

Single molecule fluorescence imaging will be explained first. Three key factors are usually considered in these experiments: 1) a small number of molecules (sometimes only one) in the illumination volume probed by the light source; 2) sufficiently large fluorescence photon counts from individual fluorophores compared to the background level; 3) detectors with high quantum efficiency and low dark noise. The optimization of the signal-to-noise ratios (SNR) by maximizing the signal and minimizing the background is a routine practice to achieve single molecule imaging.[1] To maximize the signal, new fluorescent probes with higher stability and quantum yield have been developed, including fluorescent dyes, fluorescent proteins, quantum dots, and metal clusters. To minimize the background, one needs to reduce the two main sources of background noise: 1) residual fluorescence signals from the environment, such as optical components, microscope slides and coverslips, and 2) the sample itself due to Rayleigh and Raman scattering from the solvent, impurities in the sample, and red-shifted photons into the single molecule fluorescence spectral region. The first type of background can be minimized by using high-quality optical components and ultraclean, scratch-free substrates, such as high quality fused quartz slides over normal glass slides, while the second type of background is often reduced by purifying the sample and photobleaching the solvent for an extended period before use. Furthermore, minimizing the illumination volume is another efficient method to improve the SNR, e.g., total internal reflection fluorescence microscopy (TIRFM) limits the excitation to the evanescence field of a few hundred nanometers deep, which is much shallower compared with the illumination volume in wide-field fluorescence microscopy.

Although molecular imaging probes have dominated the optical imaging field for decades, their usefulness in biological and chemical applications is often limited by optical saturation and photobleaching. Coincident with the emergence of nanomaterials, more and more nanoparticles

have found use in optical imaging to overcome these limitations. The fast development of particle synthesis and surface modification strategies has resulted in nanoparticle imaging probes of various size, shape and composition. The approaches to detect, localize, and count nanoparticles have been actively developed recently for use in biological and chemical research. Inorganic metal nanoparticles, such as gold, silver, and iron oxide nanoparticles, have been exploited as good candidates for biological applications.[2]

Among all the nanoparticles, gold nanoparticles possess unique optical properties and low cytotoxicity,[3-9] making them especially good optical imaging probes in biological applications.[2,10-15] Gold nanoparticles can be synthesized in a very wide range of diameters, from a few nanometers to several hundred nanometers. Ligand protected gold nanoparticles are usually stable for long periods of time and Gold nanoparticles can be readily modified with biomolecules, including protein, peptide, DNA/RNA, etc. Localized surface plasmon resonance (LSPR) of gold nanoparticles is a remarkable optical property which is responsible for producing strong scattering and absorption signals.

2. Application of Single Molecule and Nanoparticle Imaging

2.1 Biological systems

Single molecules and single nanoparticles are two frequently used probes in biological systems. Behaviors of individual biomolecules in their native environments and their roles in cellular processes have gained the attention from more and more researchers in chemistry and biochemistry.[16] In the traditional methods, such as western blot, perhaps because the protein is not in its native environment, the stoichiometry results are often ambiguous. On the other hand, single molecule detection allows less invasive and more quantitative measurements of reaction

parameters and molecular concentrations, and shows more precise distributions of biomolecules inside cells. Single molecule kinetics/dynamics analysis[17-19] and super-resolution imaging[20-23] are currently the most attractive and actively pursued single molecule analysis methods for cell imaging. Recent examples of single molecule imaging in cells include measuring reaction kinetics by single pair fluorescence resonance energy transfer (spFRET) and tracking single molecule dynamics along the cytoskeleton network or in the plasma membrane.[24-27] Single molecule detection has also been used in counting molecular events in living cells.[28]

Nanoparticles have been used as alternatives to fluorescent probes in optical imaging experiments. Nanoparticle imaging probes usually display better photo-stability for long-term observation. Among the wide variety of nanoparticle probes, gold nanoparticles are good candidates for diagnostic therapy and drug delivery into cells.[29] The cellular uptake of gold nanoparticles depends on nanoparticle size, shape, and surface modification. Uptake pathway of gold nanoparticles into cells includes clathrin-mediated endocytosis, caveolae-dependent endocytosis, pinocytosis macropinocytosis and phagocytosis.[30] Nanoparticle localization and counting have been demonstrated under confocal, dark/bright field, and differential interference contrast (DIC) microscopy. Modified DIC microscopy supplies an opportunity to detect and distinguish gold nanoparticles from other nano-objects in live cells. Gold nanoparticle detection in live cell is based on the wavelength-dependent image contrast. Tracking gold nanoparticle on cell membranes and inside cells during the diffusion, endocytosis, and intracellular transport processes are currently the most significant biological applications.[31-34]

2.2 Microfluidics and nanopores

Miniaturization has been one of the most active research directions in analytical chemistry in the past two decades.[35-38] Microfluidics with sub-millimeter length and micrometer thickness and width has seen many applications in information processing, clinical diagnoses,[39,40] nanomaterial/chemical synthesis,[41,42] biotechnology, and life science.[43-45] The flow velocity is critical to control many phenomena at the single molecule level, such as adsorption and diffusion on or near a functionalized surface and single molecule fluorescence resonance energy transfer. Microfluidics provides a more controllable flow, which enables to optimize the reaction efficiency and supplies longer optical interrogations.[46] Micro-/nano-scale systems with high surface-to-volume ratio transfer mass and heat with the environment fast and effectively, which results in better control over diffusion and temperature. The most widely used material in microfluidics includes glass and poly(dimethylsiloxane) (PDMS), which are both transparent in the visible range. Furthermore, PDMS with elastomeric property enables flow control and object manipulation, which can be used to build integrated multi-functional microfluidic systems.

The properties of microfluidic devices have made them highly useful in single molecule and nanoparticle imaging experiments. They have been used extensively in the research projects I have been involved with.

Nanopores with a diameter from several nanometers to several hundred nanometers have been employed in chemical and biophysical studies. Molecular transport, including diffusion, migration and adsorption/desorption, in nano-confined environments is different from that in bulk solution, and it is essential in our efforts to understand chemical separations[47-49], controlled drug release, catalysis[50], enzymatic reactions and trans-cell membranes processes. Nanopores material includes biological pores, such as protein pores[51-53], polymer nanopores[54,55], inorganic nanopores (e.g.,

silicon/silicon dioxide nanopores[56,57], alumina nanopores[58,59], titanium dioxide nanopores[60-62] and graphene nanopores[63-65]). Among all of these nanopores, inorganic aluminum oxide membranes, which have uniformly-structured nanoscale pores with a diameter from 20 nm to 200 nm, are of particular interest in my research. The alumina membranes have high thermal and chemical resistance and excellent mechanical properties. Aluminum oxide porous membranes have been used in my research to study the diffusion, migration and translocation of single protein and DNA molecules.[66-69] Others have also used them in various research fields, including chemistry,[70] biology,[71,72] medicine,[73,74] and electronic engineering.[75]

2.3 Photocatalysis

Single molecule catalysis is a relatively new way of studying individual turnover events on single nanocatalysts. Single molecule imaging in catalysis is based on the product fluorescence signal, e.g. amplex red, a non-fluorescent molecule, is catalyzed by gold or platinum nanoparticles to resorufin with strong fluorescence emission.[75-80] GC-MS and electrochemical mass spectrometry are conventional, non-optical methods to detect the catalyzed products in pollutant removal experiment, such as the catalysis of CO_2 to CO.[81,82] Metal nanoparticles, such as Pd, Pt, Au, Ag, Cu, Ni, Fe, etc., are most widely applied nanocatalysts. Some biomolecules can also be used as catalyst, such as horseradish peroxidase which is a protein and electron donor in the catalysis of amplex red to resorufin.

3. Single Molecule and Nanoparticle Imaging Techniques

3.1 Epi-fluorescence microscopy

Epi-fluorescence microscopy is the simplest form of wide-field microscopy imaging. In this mode, the illumination light passes through the entire depth of the sample in a relatively large field of view. It allows the parallel detection of many molecules of interest; however, it often suffers from poor image contrasts when compared to other more advanced modes. The basic principle of the epi-illumination is shown in Figure 1.

3.2 Total internal reflection fluorescence microscopy (TIRFM)

TIRFM is a type of wide-field optical microscopy technique used to observe fluorescent objects at the interface between two media of different refractive indexes. In TIRFM, the incident light beam illuminates the two medium from a high (n_1) to low (n_2) refractive indexes with an incident angle greater than the critical angle. The critical angle is given by:

$$\theta_c = \sin^{-1}(n_2 / n_1)$$

Under this condition, the incident light beam is total internal reflected back to the high refractive index medium. The evanescent filed is generated and propagates parallel to the interface. This electromagnetic field extends only a few hundred nanometers into the low refractive index medium. The evanescent filed decreases exponentially as the distance from the interface increases. The excitation depth is related with the incident angle (θ), the excitation wavelength (λ), and the refractive indexes, as shown in the following equation:

$$d(\theta) = \frac{\lambda}{4\pi\sqrt{(n_1 \sin\theta)^2 - n_2^{\,2}}}$$

The evanescent field intensity (I) exponentially decays with the vertical distance (z) from the interface and drops to 1/e of the value at the interface over the depth (d):

$$I_{(z)} = I_{(0)}\, e^{-z/d(\theta)}$$

There are two type of TIRFM, the objective type and prism type. As shown in Figure 2, the prism type makes it convenient to adjust the incident angle more accurately, while the objective type TIRFM provide an easy access for detecting cells and tissue samples. Since the first visualization of single fluorophore molecules on the glass surface was demonstrated in 1995, TIRFM has become a reliable and powerful technique for studying single molecule dynamics at liquid/solid surfaces and cell membranes.

3.3 Confocal microscopy

In epi-fluorescence microscopy, the excitation volume at z direction is essentially the entire sample depth. This illumination scheme results in relatively high fluorescence background from outside of the focal plane, and therefore, lower SNR. To reject the interference from the out of focus background, confocal microscopy is invented. By restricting the detection volume, the technique prevents overlying or nearby emitters from contributing to the detected signal. Point detectors are often used on a confocal microscope, such as avalanche photodiodes (APD), which allows a microsecond temporal resolution.

Photodecomposition and photobleaching of single molecules within the small detection volume under intense laser excitation can be a limitation of confocal microscopy for single molecule imaging. Fluorescent nanoparticles can be good probes for dynamic tracking due to improved photostability. Nanoparticles have been tracked in living cells or on cell membranes with confocal microscopy. A confocal image is created by raster scanning the sample stage underneath

the laser spot, typically with a motorized piezo stage. One primary advantage of confocal imaging is that it offers a better resolution along the z direction, which enables the optical sectioning of thick samples. By multiple scanning in the z direction, the three-dimensional structure of the sample can be reconstructed.

3.4 Differential interference contrast (DIC) microscopy

DIC microscopy is a visible light microscope with interferometric functionality to increase the contrast of transparent samples.[84,85]Theschematic drawing is shown in Figure 3.[83,84] DIC microscopy components include a pair of polarizer-analyzer and two Nomarski prisms. The illumination light beam passes the first polarizer and initially polarized by 45°. Then polarized illumination light beams are split into two orthogonal beams with lateral displacement, of which the distance is called shear distance. The shear distance is smaller than the resolution of the microscope. Then two light beams are focused and guided to the specimen by a condenser. Because of the shear distance between the two beams, they experience different optical density. Then the two beams are recombined at the second Nomarski prism and the shear distance is removed. The recombined beams interfere to produce amplitude contrast when they pass the analyzer. Gold nanoparticles show good contrast and this contrast depends on the wavelengths, which makes gold nanoparticles a good imaging probe in living cells. Chapter 3 reports the use of gold nanoparticles as drug delivery carriers and imaging contrast probes to study stem cell proliferation.

3.5 Super-resolution microscopy

Wide-field microscopy allows one to detect single molecules and nanoparticles with a spatial resolution ~250nm due to the diffraction of light. The resolution can be calculated with the following equation.

$$d = \frac{1.22\lambda}{N.A.(\text{obj}) + N.A.(\text{cond.})}$$

where λ: wavelength; N.A.(obj.): objective numerical aperture; N.A.(cond.): condenser numerical aperture. Numerical aperture is also defined by (α): N.A. = n • sin (α), where n is the medium refractive index and α is the aperture angle. By using larger N.A. objective and condenser one can achieve better resolution within the diffraction limitation.

There are several super-resolution microscopy techniques to break the fundamental barrier of light diffraction, such as stochastic optical reconstruction microscopy (STORM), photoactivated localization microscopy (PALM), stimulated emission depletion (STED) microscopy, and scanning probe microscopy (SPM).

A brief introduction of STORM is provided here because many concepts used in STORM are used in my research.

STORM and PALM are similar techniques demonstrated by different groups.[85-91] To perform STORM or PALM, photoactivatible fluorophores and two lasers are applied. The first laser at a longer wavelength and higher power is used to bring the fluorophores to dark state while the second laser at a short wavelength reverse the dark-state fluorophores back to the excitable state. Local fluorophores are excited one by one randomly, as shown in Figure 4. The fluorescence spot give the point spread function. Gaussian functions are fit to the spots and generate highly accurate positions of individual molecules. The final images are reconstructed by accumulating the positional information of individual molecules, and the lateral resolution can be improved to20~30

nm. 3D STORM has also been demonstrated by inserting a cylindrical lens in the optical path in front of the detector to purposely induce astigmatism, and the resolution in axial direction can be improved to 50~60 nm.[92]

References

(1) Weiss, S. *Science* **1999**, *283*, 1676.

(2) De, M.; Ghosh, P. S.; Rotello, V. M. *Advanced Materials* **2008**, *20*, 4225.

(3) Anker, J. N.; Hall, W. P.; Lyandres, O.; Shah, N. C.; Zhao, J.; Van Duyne, R. P. *Nature Materials* **2008**, *7*, 442.

(4) Jain, P. K.; Huang, X. H.; El-Sayed, I. H.; El-Sayed, M. A. *Accounts of Chemical Research* **2008**, *41*, 1578.

(5) Stewart, M. E.; Anderton, C. R.; Thompson, L. B.; Maria, J.; Gray, S. K.; Rogers, J. A.; Nuzzo, R. G. *Chemical Reviews* **2008**, *108*, 494.

(6) Chourpa, I.; Lei, F. H.; Dubois, P.; Manfait, M.; Sockalingum, G. D. *Chemical Society Reviews* **2008**, *37*, 993.

(7) Grant, S. A.; Spradling, C. S.; Grant, D. N.; Fox, D. B.; Jimenez, L.; Grant, D. A.; Rone, R. J. *Journal of Biomedical Materials Research Part A* **2014**, *102*, 332.

(8) Lewinski, N.; Colvin, V.; Drezek, R. *Small* **2008**, *4*, 26.

(9) Shukla, R.; Bansal, V.; Chaudhary, M.; Basu, A.; Bhonde, R. R.; Sastry, M. *Langmuir* **2005**, *21*, 10644.

(10) Mandal, S.; Bakeine, G. J.; Krol, S.; Ferrari, C.; Clerici, A. M.; Zonta, C.; Cansolino, L.; Ballarini, F.; Bortolussi, S.; Stella, S.; Protti, N.; Bruschi, P.; Altieri, S. *Applied Radiation and Isotopes* **2011**, *69*, 1692.

(11) Pissuwan, D.; Niidome, T.; Cortie, M. B. *Journal of Controlled Release* **2011**, *149*, 65.

(12) Mandal, D. *Advances in Experimental Medicine and Biology* **2010**, 435.

(13) Mallick, K.; Witcomb, M. *Journal of Nanoscience and Nanotechnology* **2010**, 225.

(14) Ghosh, P.; Han, G.; De, M.; Kim, C. K.; Rotello, V. M. *Advanced Drug Delivery Reviews* **2008**, *60*, 1307.

(15) Venditti, I.; Fontana, L.; Fratoddi, I.; Battocchio, C.; Cametti, C.; Sennato, S.; Mura, F.; Sciubba, F.; Delfini, M.; Russo, M. V. *Journal of Colloid and Interface Science* **2014**, *418*, 52.

(16) Xia, T.; Li, N.; Fang, X. H. *Annual Review of Physical Chemistry*. **2013**, *64*, 459.

(17) Murakoshi, H.; Iino, R.; Kobayashi, T.; Fujiwara, T.; Ohshima, C.; Yoshimura, A.; Kusumi, A. *Proceedings of the National Academy of Sciences of the United States of America* **2004**, *101*, 7317.

(18) James, J. R.; White, S. S.; Clarke, R. W.; Johansen, A. M.; Dunne, P. D.; Sleep, D. L.; Fitzgerald, W. J.; Davis, S. J.; Klenerman, D. *Proceedings of the National Academy of Sciences of the United States of America* **2007**, *104*, 17662.

(19) Levi, V.; Gratton, E. *Cell Biochem Biophys* **2007**, *48*, 1.

(20) Dietz, M. S.; Fricke, F.; Kruger, C. L.; Niemann, H. H.; Heilemann, M. *ChemPhysChem* **2014**, *15*, 671.

(21) Hu, Y. S.; Zimmerley, M.; Li, Y.; Watters, R.; Cang, H. *ChemPhysChem* **2014**, *15*, 577.

(22) Bates, M.; Huang, B.; Dempsey, G. T.; Zhuang, X. W. *Science* **2007**, *317*, 1749.

(23) Huang, B.; Bates, M.; Zhuang, X. W. In *Annual Review of Biochemistry*; Annual Reviews: Palo Alto, 2009; Vol. 78, p 993.

(24) Wabuyele, M. B.; Farquar, H.; Stryjewski, W.; Hammer, R. P.; Soper, S. A.; Cheng, Y. W.; Barany, F. *Journal of the American Chemical Society*. **2003**, *125*, 6937.

(25) Koopmans, W. J. A.; Brehm, A.; Logie, C.; Schmidt, T.; van Noort, J. *Journal of Fluorescence*. **2007**, *17*, 785.

(26) Tezuka-Kawakami, T.; Gell, C.; Brockwell, D. J.; Radford, S. E.; Smith, D. A. *Biophysical Journal*. **2006**, *91*, L42.

(27) de Keijzer, S.; Galloway, J.; Harms, G. S.; Devreotes, P. N.; Iglesias, P. A. *Biochimica et Biophysica Acta (BBA) - Biomembranes* **2011**, *1808*, 1701.

(28) Sako, Y.; Hiroshima, M.; Pack, C. G.; Okamoto, K.; Hibino, K.; Yamamoto, A. *Wiley interdisciplinary reviews. Systems biology and medicine* **2012**, *4*, 183.

(29) Mayhew, T. M.; Muhlfeld, C.; Vanhecke, D.; Ochs, M. *Annals of Anatomy*. **2009**, *191*, 153.

(30) Alkilany, A.; Murphy, C. *Journal of Nanoparticle Research* **2010**, *12*, 2313.

(31) Astolfo, A.; Arfelli, F.; Schultke, E.; James, S.; Mancini, L.; Menk, R. H. *Nanoscale* **2013**, *5*, 3337.

(32) Lasne, D.; Blab, G. A.; Berciaud, S.; Heine, M.; Groc, L.; Choquet, D.; Cognet, L.; Lounis, B. *Biophysical Journal* **2006**, *91*, 4598.

(33) Rong, G. X.; Wang, H. Y.; Skewis, L. R.; Reinhard, B. M. *Nano Letters* **2008**, *8*, 3386.

(34) Sun, L. L.; Liu, D. J.; Wang, Z. X. *Langmuir* **2008**, *24*, 10293.

(35) Craighead, H. G. *Science* **2000**, *290*, 1532.

(36) Quake, S. R.; Scherer, A. *Science* **2000**, *290*, 1536.

(37) Sackmann, E. K.; Fulton, A. L.; Beebe, D. J. *Nature* **2014**, *507*, 181.

(38) Mark, D.; Haeberle, S.; Roth, G.; von Stetten, F.; Zengerle, R. *Chemical Society Reviews* **2010**, *39*, 1153.

(39) Prakash, M.; Gershenfeld, N. *Science* **2007**, *315*, 832.

(40) Weaver, J. A.; Melin, J.; Stark, D.; Quake, S. R.; Horowitz, M. A. *Nature Physics* **2010**, *6*, 218.

(41) Huebner, A.; Sharma, S.; Srisa-Art, M.; Hollfelder, F.; Edel, J. B.; Demello, A. *Lab on a Chip* **2008**, *8*, 1244.

(42) Makgwane, P. R.; Ray, S. S. *Journal of Nanoscience and Nanotechnology* **2014**, *14*, 1338.

(43) Di Carlo, D.; Wu, L. Y.; Lee, L. P. *Lab on a Chip* **2006**, *6*, 1445.

(44) Vasdekis, A. E.; O'Neil, C. P.; Hubbell, J. A.; Psaltis, D. *Biomacromolecules* **2010**, *11*, 827.

(45) Chung, K.; Kim, Y.; Kanodia, J. S.; Gong, E.; Shvartsman, S. Y.; Lu, H. *Nature Methods* **2011**, *8*, 171.

(46) Gambin, Y.; VanDelinder, V.; Ferreon, A. C. M.; Lemke, E. A.; Groisman, A.; Deniz, A. A. *Nature Methods* **2011**, *8*, 239.

(47) Jubery, T. Z.; Prabhu, A. S.; Kim, M. J.; Dutta, P. *Electrophoresis* **2012**, *33*, 325.

(48) Wang, J. R.; Ma, J.; Ni, Z. H.; Zhang, L.; Hu, G. Q. *RSC Advances* **2014**, *4*, 7601.

(49) Joo, S. W.; Lee, S. Y.; Liu, J.; Qian, S. Z. *ChemPhysChem* **2010**, *11*, 3281.

(50) Takale, B. S.; Bao, M.; Yamamoto, Y. *Organic & Biomolecular Chemistry* **2014**, *12*, 2005.

(51) Bayley, H.; Jayasinghe, L. *Molecular membrane biology* **2004**, *21*, 209.

(52) Bayley, H.; Cremer, P. S. *Nature* **2001**, *413*, 226.

(53) Rhee, M.; Burns, M. A. *Trends in Biotechnology* **2007**, *25*, 174.

(54) Vlassiouk, I.; Siwy, Z. S. *Nano Letters* **2007**, *7*, 552.

(55) Ali, M.; Schiedt, B.; Healy, K.; Neumann, R.; Ensinger, W. *Nanotechnology* **2008**, *19*, 085713.

(56) Storm, A. J.; Chen, J. H.; Ling, X. S.; Zandbergen, H. W.; Dekker, C. *Nature Materials* **2003**, *2*, 537.

(57) Chen, G. S.; Boothroyd, C. B.; Humphreys, C. J. *Philosophical Magazine A* **1998**, *78*, 491.

(58) Masuda, H.; Fukuda, K. *Science* **1995**, *268*, 1466.

(59) Nielsch, K.; Choi, J.; Schwirn, K.; Wehrspohn, R. B.; Gösele, U. *Nano Letters* **2002**, *2*, 677.

(60) Qiao, Y.; Bao, S. J.; Li, C. M.; Cui, X. Q.; Lu, Z. S.; Guo, J. *ACS Nano* **2008**, *2*, 113.

(61) Liu, Y. B.; Gan, X. J.; Zhou, B. X.; Xiong, B. T.; Li, J. H.; Dong, C. P.; Bai, J.; Cai, W. M. *Journal of Hazardous Materials* **2009**, *171*, 678.

(62) Koganti, V. R.; Dunphy, D.; Gowrishankar, V.; McGehee, M. D.; Li, X. F.; Wang, J.; Rankin, S. E. *Nano Letters* **2006**, *6*, 2567.

(63) Merchant, C. A.; Healy, K.; Wanunu, M.; Ray, V.; Peterman, N.; Bartel, J.; Fischbein, M. D.; Venta, K.; Luo, Z. T.; Johnson, A. T. C.; Drndic, M. *Nano Letters* **2010**, *10*, 2915.

(64) Ganzhorn, M.; Klyatskaya, S.; Ruben, M.; Wernsdorfer, W. *ACS Nano* **2013**, *7*, 6225.

(65) Feng, P. X. *Nature nanotechnology* **2013**, *8*, 897.

(66) Ma, C.; Han, R.; Qi, S.; Yeung, E. S. *Journal of chromatography. A* **2012**, *1238*, 11.

(67) Ma, C.; Yeung, E. S. *Analytical Chemistry* **2009**, *82*, 478.

(68) Ma, C.; Yeung, E. S. *Analytical Chemistry* **2009**, *82*, 654.

(69) Han, R.; Wang, G.; Qi, S.; Ma, C.; Yeung, E. S. *The Journal of Physical Chemistry C* **2012**, *116*, 18460.

(70) Lee, H. J.; Yasukawa, T.; Suzuki, M.; Taki, Y.; Tanaka, A.; Kameyama, M.; Shiku, H.; Matsue, T. *Sensors and Actuators B: Chemical* **2008**, *131*, 424.

(71) Venkatesan, B. M.; Dorvel, B.; Yemenicioglu, S.; Watkins, N.; Petrov, I.; Bashir, R. *Advanced Materials* **2009**, *21*, 2771.

(72) Chen, P.; Gu, J.; Brandin, E.; Kim, Y.-R.; Wang, Q.; Branton, D. *Nano Letters* **2004**, *4*, 2293.

(73) Losic, D.; Simovic, S. *Expert opinion on drug delivery* **2009**, *6*, 1363.

(74) Gultepe, E.; Nagesha, D.; Sridhar, S.; Amiji, M. *Advanced drug delivery reviews* **2010**, *62*, 305.

(75) Sambur, J. B.; Chen, P. *Annual Review of Physical Chemistry* **2014**, *65*, 395.

(76) Wang, J.; Chen, P.; Pan, H.; Xiong, Z.; Gao, M.; Wu, G.; Liang, C.; Li, C.; Li, B.; Wang, J. *ChemSusChem* **2013**, *6*, 2181.

(77) Andoy, N. M.; Zhou, X.; Choudhary, E.; Shen, H.; Liu, G.; Chen, P. *Journal of the American Chemical Society* **2013**, *135*, 1845.

(78) Ochoa, M. A.; Zhou, X.; Chen, P.; Loring, R. F. *The Journal of chemical physics* **2011**, *135*, 174509.

(79) Chen, P.; Zhang, X.; Miao, Z.; Han, B.; An, G.; Liu, Z. *Journal of Nanoscience and Nanotechnology* **2009**, *9*, 2628.

(80) Ha, J. W.; Ruberu, T. P. A.; Han, R.; Dong, B.; Vela, J.; Fang, N. *Journal of the American Chemical Society* **2014**, *136*, 1398.

(81) Iablokov, V.; Beaumont, S. K.; Alayoglu, S.; Pushkarev, V. V.; Specht, C.; Gao, J.; Alivisatos, A. P.; Kruse, N.; Somorjai, G. A. *Nano Letters* **2012**, *12*, 3091.

(82) Reske, R.; Duca, M.; Oezaslan, M.; Schouten, K. J. P.; Koper, M. T. M.; Strasser, P. *The Journal of Physical Chemistry Letters* **2013**, *4*, 2410.

(83) Trattner, S.; Kashdan, E.; Feigin, M.; Sochen, N. *J. Journal of the Optical Society of America A: Optics, Image Science, and Vision.* **2014**, *31*, 968.

(84) Zarubiieva, I.; Hwang, G. B.; Lee, J. S.; Bae, G. N.; Oh, Y. M.; Park, S. W.; Lee, T. J.; Lee, H. J.; Woo, D. H.; Lee, S.; Cho, M. O.; Kim, J. K.; Jun, S. C.; Kim, J. H. *Aerosol and Air Quality Research* **2013**, *13*, 1145.

(85) van de Linde, S.; Loeschberger, A.; Klein, T.; Heidbreder, M.; Wolter, S.; Heilemann, M.; Sauer, M. *Nature Protocols* **2011**, *6*, 991.

(86) Jones, S. A.; Shim, S.-H.; He, J.; Zhuang, X. *Nature Methods* **2011**, *8*, 499.

(87) Lippincott-Schwartz, J.; Manley, S. *Nature Methods* **2009**, *6*, 21.

(88) Rust, M. J.; Bates, M.; Zhuang, X. *Nature Methods* **2006**, *3*, 793.

(89) Owen, D. M.; Rentero, C.; Rossy, J.; Magenau, A.; Williamson, D.; Rodriguez, M.; Gaus, K. *Journal of Biophotonics* **2010**, *3*, 446.

(90) Muzzey, D.; van Oudenaarden, A. In *Annual Review of Cell and Developmental Biology* 2009; Vol. 25, p 301.

(91) Betzig, E.; Patterson, G. H.; Sougrat, R.; Lindwasser, O. W.; Olenych, S.; Bonifacino, J. S.; Davidson, M. W.; Lippincott-Schwartz, J.; Hess, H. F. *Science* **2006**, *313*, 1642.

(92) Huang, B.; Wang, W.; Bates, M.; Zhuang, X. *Science* **2008**, *319*, 810.

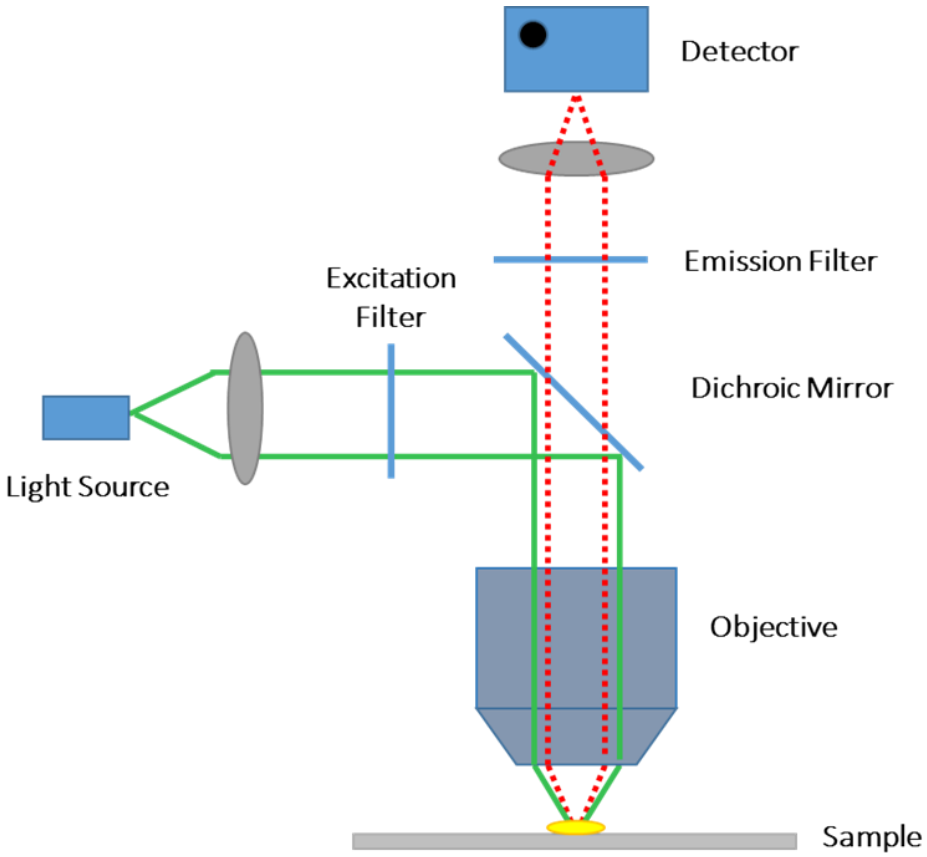

Figure 1.Schematic drawing of epi-fluorescence microscopy. The excitation light irradiates the specimen. The emission is collected by the objective and directed by a dichroic mirror towards the detector.

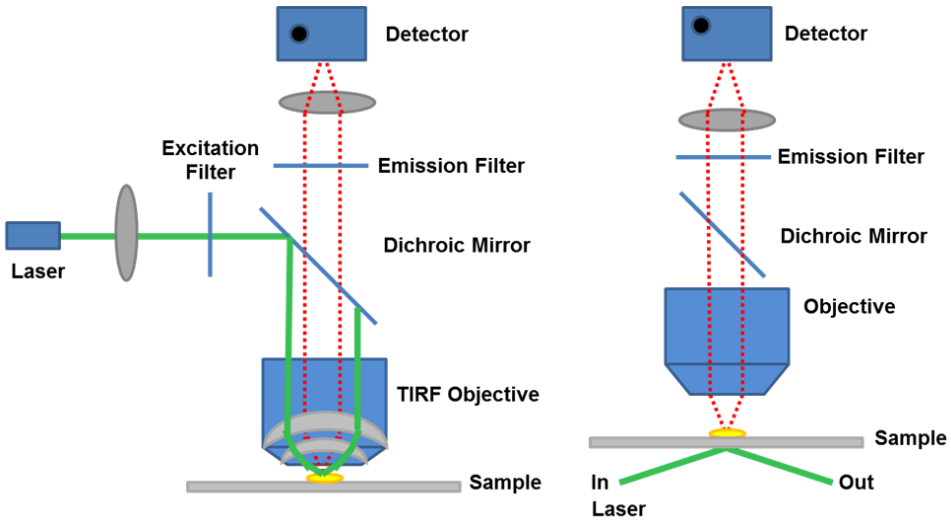

Figure 2. Schematic drawing of TIRFM. Objective type TIRFM (left). Prism type TIRFM (right).

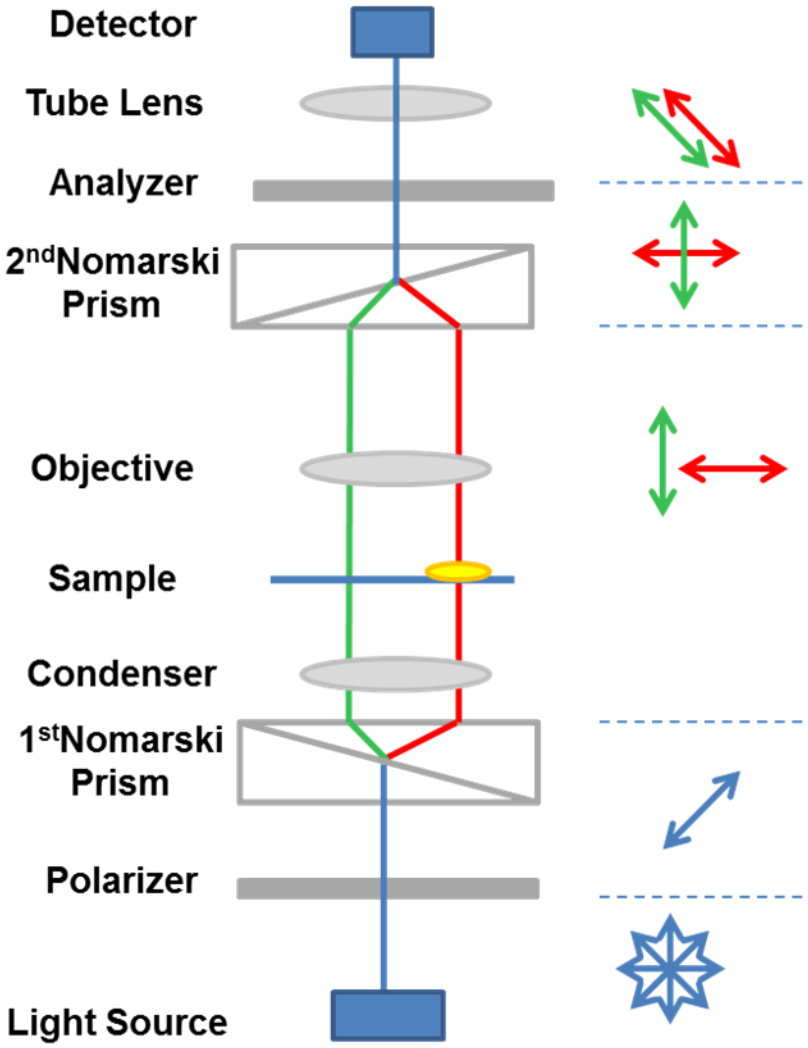

Figure 3.Schematic drawing of DIC microscopy.

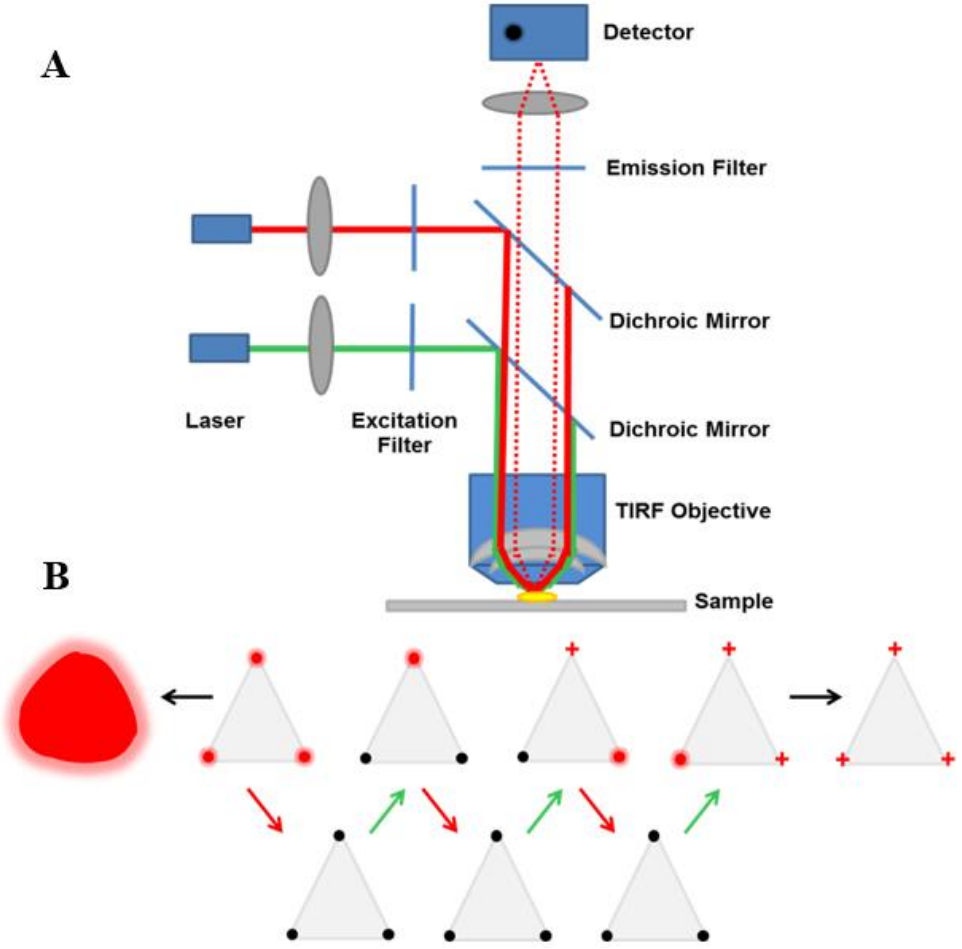

Figure 4. Mechanism of STORM. (A) Schematic drawing of STORM instrument on an objective type TIRFM microscope. (B) Principle of improved resolution in STORM. When three dyes are located within 250 nm, they cannot be resolved if they are excited simultaneously under a normal fluorescence microscope. In STORM, the three dyes are controlled to be excited one by one. The location of each dye can be determined through centroid fitting.

CHAPTER 2. ELECTROPHORETIC MIGRATION AND AXIAL DIFFUSION OF INDIVIDUAL NANOPARTICLES IN CYLINDRICAL NANOPORES

Rui Han, Gufeng Wang, Shengda Qi, Changbei Ma, and Edward S. Yeung

Published in the Journal of Physical Chemistry C

Abstract

Membranes with straight, vertical nanopores have found widespread applications in chemical and biological sciences, including separation, detection, catalysis and drug delivery. They can also serve as a model system to understand molecular behavior and fundamental mechanisms of separation, bridging the gap between conventional model systems such as flat surfaces and real chromatographic stationary phases such as micron-sized porous particles. We recently found that the axial motion of individual biomolecules inside nanopores can be significantly slower than in bulk solution. This suggests that either chromatographic adsorption was present and/or the viscosity inside the nanopores was unusually high. In this study, we measured the electrophoretic motion as well as the axial diffusion of individual nanoparticles in cylindrical alumina nanopores. We found that the electrophoretic mobilities and the diffusion coefficients of polystyrene nanoparticles were both smaller by a factor of 20~28 compared to bulk solution independent of particle size or pore diameter. The results confirm that the solution viscosity in nanodomains is anomalous.

Introduction

Molecular transport processes, e.g., diffusion, migration, and adsorption/desorption, at nano-confined environments can be different from those in bulk solution. The understanding of these

phenomena is important to separations, controlled drug release, heterogeneous catalysis, and trans-cell membrane biological processes, etc. Inorganic aluminum oxide membranes made by anodic oxidation are receiving increasing attention in recent years.[1, 2] The most attractive feature of these membranes is that they contain uniform, well-structured nanoscale pores that are aligned perpendicular to the membrane plane, i.e., there is little contribution from tortuosity. The diameter of these parallel cylindrical pores depends on the applied voltage during anodic oxidation and can be varied between 20 and 200 nm with a tight distribution.[2-6] In addition, these alumina membranes have high thermal and chemical resistance and excellent mechanical properties. For these reasons, they are interesting targets both in fundamental research and for real applications in chemistry,[7] biology,[8, 9] medicine,[10-12] and electronic engineering.[13]

Alumina membranes are especially important in separation science, e.g., serving as membrane filters[14] or as potential size-exclusion chromatography (SEC) stationary phases.[15] SEC is widely used for the separation and purification of macromolecules such as proteins, polysaccharides, and nucleic acids.[16] The underlying principle of SEC is that the elution time of macromolecules of different sizes through the stationary phase is dependent on different degrees of excursion into the pores due to accessibility and intraparticle obstruction. In addition to real applications, alumina membranes with cylindrical pores are important in chromatographic studies because they can serve as a model system to bridge the gap between conventional model systems, e.g., flat surfaces,[17-21] and real chromatographic materials e.g., micron-sized porous silica particles. In particular, the availability of nanopores with mono-dispersed size distribution allows one to correlate the pore size with the dynamic processes during separation for comparison with theory. The inner wall of the membrane can be further modified by plating a metal/metal oxides layer or by grafting self-assembled monolayers.[1, 22-25] Fine tuning the microenvironment within the pores will give us more

flexibility and power to control and understand the interfacial phenomena in these nanoscale domains.

Recent studies showed that diffusion and transport of macromolecules through porous materials can be substantially slower than in bulk solution.[26-31] A more recent study showed that when the inner wall of nanopores was treated to minimize adsorption, the diffusion coefficient of protein molecules was increased by two orders of magnitude as compared to that in similar sized untreated polycarbonate membrane pores, indicating that adsorption may be one of the factors that are contributing to the slow diffusion in the latter.[32] However, diffusion in the former was still significantly slower than that in bulk solution, implying that the viscosity may be higher in the microenvironment of nanometer sized pores. In this study, we investigated the electrophoretic migration as well as axial diffusion of single nanoparticles through the nanopores in alumina membranes. Single particle imaging allows the removal of ensemble average and accounts for the poly-dispersity of each type of particles. More importantly, unlike previous studies that measure only the net transport of molecules across similar membranes, each particle here is already inside the nanopore. No assumptions about accessibility and adsorption outside the pores are necessary. Since viscosity is a common parameter in electromigration and axial diffusion, we can directly assess its dependence on the local environment.

Experimental Section

Materials. Porous alumina membranes with pore diameters of 100 nm and 200 nm and a thickness of 60 μm were purchased from Whatman International (Maidstone, UK). The membranes were preconditioned in the relevant buffer for 30 min before being used in the diffusion and electrophoretic migration experiments. Indium tin oxide (ITO) coated coverslips (20 × 20 mm,

70-100 ohms, Structure Probe, Inc.) were used as the electrodes to apply electrical field across the porous membrane.

The 85 nm and 50 nm polystyrene particles were purchased from Duke Scientific (Fremont, CA). The actual diameters were 88 ± 8 nm and 51 ± 7 nm, respectively, according to the manufacturer. 100 nm polystyrene nanoparticles that were surface-activated with carboxylate groups were purchased from Invitrogen/Molecular Probes (Eugene, OR). The actual diameter was 100 ± 6 nm. The reported concentrations for the original 85 nm and 50 nm nanoparticle solutions were 3.0×10^{13} and 1.5×10^{14} particles/mL. The concentration of the 100 nm particles was 3.6×10^{13} particles/mL. The refractive index of all three nanoparticles was 1.59. Nanoparticles were diluted 10,000-fold in 25 mM pH 9.0 CHES buffer solution (25 mM CHES buffer solution adjusted to pH 9.0 with 1.0 M NaOH) before observation. Coumarin 540A (Exciton, Dayton, OH) was chosen as the electroosmotic flow (EOF) marker in capillary and in nanopore electrophoresis experiments.

Nanopore electrophoresis experimental setup. Figure 1a shows the schematic of the electrophoretic migration experiments in the nanopores. The alumina membrane was **s**andwiched between two ITO coated cover glasses. An 18 × 18 mm coverslip (Corning Co., NY) with a 6.0-mm hole drilled in the center served as the spacer and reservoir between the bottom ITO glass and the alumina membrane. The spacer and the bottom ITO glass were sealed with nail polish to prevent leaking. 20 µL CHES buffer solution was added in the reservoir before being covered by the membrane. 5 µL diluted nanoparticle solution was added on top of the membrane. The top ITO glass then covered the porous membrane. The top ITO glass and the membrane were separated by 2 pieces of 160-µm double-sided tape serving as spacers, leaving a buffer layer of 100 µm between

the ITO glass and the membrane. Conductive wires attached to the upper and bottom ITO glasses were connected to a DC power supply (Power Design Inc.) that had a precision of 0.001V.

Figure 1b shows the schematic of the observation geometry in the diffusion and electrophoretic migration experiments. The focal plane was set at 3 μm beneath the porous membrane/solution interface. The full width at half maximum (FWHM) of the focal depth was measured to be 1.67 μm (Supplementary Figure 1). This observation geometry (3 μm inside the membrane as compared to the 200 nm pore diameter) guaranteed that a diffusing particle could "sample" all radial positions many times before it escaped from the pore.

Single particle fluorescence microscopy. An upright Nikon 80i Eclipse microscope was used in the epifluorescence mode in acquiring particle images. In the electrophoretic migration and diffusion experiments, a 100× Plan Apo/1.40 oil immersion objective was used to focus the illumination light from a mercury lamp and to collect the fluorescence signal. In the studies of the distribution of particles in the whole membrane where a longer working distance was needed, a 40× air objective (Zeiss) was used. A Photometrics Evolve 512 camera (Photometrics, Tucson, AZ; cooled at -80 ^{O}C, 512 × 512 imaging array, 16 μm × 16 μm pixel size) or an Andore Ixon DV 897 camera (Belfast, Northern Ireland; cooled at -50 ^{O}C, 512 × 512 imaging array, 16 μm × 16 μm pixel size) was used to image individual nanoparticles. A digital rotary motor (Sigma Koki, Japan) coupled with the microscope stage was used to control the vertical position of the sample. The CCD camera and the stage were synchronized by a home-written C++ computer program.[33] MATLAB and NIH ImageJ programs were used to analyze the collected images and videos.

CE experimental apparatus. A Beckman Coulter MDQ System (Fullerton, CA) with a laser-induced fluorescence module was used in particle CE experiments. The excitation wavelength was

488 nm from an argon laser. The fused silica capillary was 50 cm in length (39 cm to detector) and 75 μm in inner diameter (Polymicro Technologies, Phoenix, AZ).

Before use, the capillary was conditioned with 1.0 M NaOH for 10 min, deionized water for 10 min, and then flushed with the relevant buffer for 30 min. Between two CE runs, the capillary was rinsed with 25 mM NaOH for 5 min, deionized water for 2 min and the relevant buffer for 10 min. In each CE run, the nanoparticle sample solution was injected at 0.5 psi for 30 s and then driven by 25 kV.

Coumarin 540A was used as the EOF maker. Coumarin 540A was dissolved in methanol as a 1.0 mM stock solution. In each CE run, it was used independently or added to the particle solution with a final concentration of 1.0 μM. The concentrations of 85 nm and 50 nm particles injected into the capillary were 3.0×10^{11} and 1.5×10^{12} particles/mL respectively.

Zeta potential. A Malvern Nano HT Zetasizer was used to measure the ζ-potentials of the particles. Particles were suspended in 25 mM pH 9.0 CHES buffer. Both 85 nm and 50 nm particle solutions were diluted to a final concentration of 3.0×10^{11} particles/mL. After vortexing for 5 min, the ζ-potential was measured and 20 scans were taken of each sample.

Results and Discussion

Enumeration of particles. Porous alumina membrane is a highly scattering medium. In order to avoid observation bias caused by scattering at different depths, the distribution of nanoparticles inside 200 nm nanopores was investigated. Briefly, 100 nm particle solution with a concentration of 3.6×10^{9} particles/mL was added to the reservoir and a 1.5-V electric voltage was applied for 180 s to expedite the migration of the particles into the cylindrical pores. The electric field was then turned off and the system was incubated for 300 s to reach distribution equilibrium. The

membrane was then scanned vertically with a 40 × air objective (NA = 0.75) to image the particles distributed inside the membrane. The particle numbers at each depth were counted and plotted in Figure 2. The distribution of the nanoparticles in the whole alumina membrane is nearly uniform, indicating all particles were counted and fluorescence signal loss due to scattering will not affect the enumeration of particles at different depths of the membrane. Figure 2 also shows that there are no obstructions inside the nanopores that would prevent the nanoparticles, especially the smaller ones used in subsequent experiments from passing all the way through. That is, the contribution from constriction[34] can be neglected.

Electrophoretic mobility of nanoparticles in bulk solution. Bulk electrophoretic mobilities of 85 nm and 50 nm nanoparticles were measured by using capillary electrophoresis in 25 mM CHES buffer adjusted to pH 9.0. The elution times for Coumarin 540A, 50 nm and 85 nm particles were 2.20 min, 4.88 min and 5.91 min, respectively (Figure 3). Coumarin 540A is a neutral dye that can be used to determine the electroosmotic mobility.[35] In the presence of nanoparticles, some adsorption took place to create a mixture of slower migrating complexes. The fastest migrating species in Figure 3 was the free dye. In the calculations, the equations below were used:

$$\mu_{EOF} = \frac{v_{EOF}}{E} \quad (1)$$

$$\mu_{App} = \frac{v_{App}}{E} \quad (2)$$

$$\mu_{Ep} = \mu_{App} - \mu_{EOF} \quad (3)$$

where μ_{EOF} is the electroosmotic mobility; μ_{App} and μ_{Ep} are the apparent and native electrophoretic mobilities of the nanoparticles, respectively; E is the electric field applied across the capillary column; v_{EOF} and v_{App} are the absolute velocities of the electroosmotic flow and the nanoparticles, respectively; v is calculated from:

$$v = \frac{L}{t} \quad (4)$$

where t is the time the particle spent travelling an effective length L.

The observed EOF is large and is in the order of 10^{-8} $m^2V^{-1}s^{-1}$, which is consistent with the literature values for silica surface.[36-38] The absolute value of the electrophoretic mobility of 85 nm particles is larger than that of 50 nm particles, causing the 85 nm particles to elute behind the 50 nm particles due to the opposite direction of the EOF. Their mobilities are -4.4×10^{-8} $m^2V^{-1}s^{-1}$ and -3.9×10^{-8} $m^2V^{-1}s^{-1}$, respectively. The ratio of mobilities is fairly consistent with the ζ-potential ratio (-48 mV for 85 nm and -37 mV for 50 nm particles, respectively), confirming that the electrophoretic mobility of the nanoparticles abides by the Smoluchowski equation[39] and is dictated by the surface charge:

$$\mu_{Ep} = \frac{q}{6\pi\eta R} \quad (5)$$

where η is the viscosity of the solvent; R is the radius of the particle and q is the surface charge on the particle.

Electrophoretic mobility of nanoparticles in nanopores. The electrophoretic mobility of nanoparticles in cylindrical nanopores can be estimated in a similar way using Equations 1-4. However, the measurements were more complicated for electrophoresis in the nanopores of a membrane filter that is only 60 μm thick. To accomplish this, we designed an experimental apparatus as illustrated in Figure 1. By watching the particles move vertically through a fixed depth inside the cylindrical nanopores under a known electric field, we were able to measure all of the variables in Equations 1-4.

In this setup, the effective length L is the depth of the focal plane of the microscope objective used in collecting the fluorescence signals from the particles. The depth of the focal plane is

characterized as the full width at half maximum (FWHM) of the point spread function (PSF) of the microscope. In practice, immobilized nanoparticles on a glass coverslip were scanned vertically and their *z*-intensity profiles were plotted. The FWHM of 40 *z*-intensity profiles of 85-nm and 50-nm particles each were analyzed and the average was determined to be 1.67 ± 0.2 μm. In the electrophoretic migration experiments, when a nanoparticle migrates into and then leaves the focal plane that is placed deep inside the membrane, it generates an intensity-time trace with an appearance of a boxcar function. To determine the time the particle spent in the focal plane, i.e., the duration over which a particle is "in focus", the threshold is further set at the half intensity maximum to judge whether the particle is in or outside the focal plane. By using this criterion, we can estimate the v_{App} of the particles. In effect, the calculation fits the PSF (the observation depth) to the stochastic motion that is characteristic of single particles so as to provide better statistics than if the depth of the nanoparticle was monitored over time.

To obtain the μ_{App} of the particles, the effective electric field applied across the cylindrical nanopores must be known. Due to the existence of the buffer reservoirs at both sides of the membrane, the voltage applied across the membrane does not equal the total voltage applied on the 2 ITO glasses. However, the effective voltage U_{eff} can be estimated according to Ohm's law:

$$U_{Eff} = U_{Total}\frac{R_2}{R_1 + R_2 + R_3} \qquad (6)$$

where U_{total} is the total voltage applied across the 2 ITO glasses; R_1, R_2, and R_3 are the electric resistances of the buffer on top of the membrane, in the membrane, and below the membrane, respectively. The electric resistance is proportional to the resistivity of the buffer ρ and the thickness of the buffer layer *L*, and is inversely proportional to the cross section of the buffer layer *S*:

$$R = \rho L / S \qquad (7)$$

In our experimental setup, the upper buffer layer had a cross section of 1.96 cm^2 (the ITO glass active area) and a thickness of 100 μm (height of the double-sided tape spacer minus the membrane thickness). The bottom layer had a cross section of 0.28 cm^2 (the size of the drilled hole) and a thickness of 120 μm (the thickness of the spacer). The membrane thickness was 60 μm. The effective area that can pass buffer is estimated to be 43% from SEM images of the porous membranes. Thus, for a piece of membrane with a diameter of 1.3 cm, the effective area was 0.57 cm^2. Since the same buffer was used throughout the vertical nanopore electrophoresis apparatus, the resistivity of the buffer cancels out in Equations 6 and 7. Combining Equations 6 and 7, we determined that U_{eff} is 18% of the total voltage applied on the 2 ITO glasses.

In the experiments, the focal plane was set at 3.0 μm beneath the membrane/buffer interface to avoid extra signal loss due to scattering while keeping the observation away from the entrance/exit of the nanopore so as to better reflect the migration in an "infinite" cylindrical tube. The CCD camera was kept on all the time to capture any particles that were migrating through the fixed focal plane. By using this sitting-and-watching approach, we recorded the electrophoretic migration times of 85 nm and 50 nm particles at several different voltages (Figure 4). For a typical single-particle electrophoretic migration intensity trace, please see Supplementary Figure 2. For each experimental condition, over 150 particles were analyzed.

From Equations 1-4, we were able to estimate the apparent electrophoretic mobility of particles in the nanopores (Figure 4). We note that unlike capillary electrophoresis, the migration times of individual particles showed a broad distribution. The stochastic behavior is typical of single-particle events and may come from 2 reasons: (1) the particle size and thus the surface charge of the particles varied from particle to particle. The manufacturer reported that the relative standard deviation for the particle size is 10~15%; and (2) the pore size varied from nanopore to

nanopore. From the SEM image of the alumina membranes, we estimated that the pore area variation is ~ 20% of the average pore area. These variations may contribute to the distribution of the electrophoretic migration times of the particles. Also, at each experimental condition, there were always a few particles that stayed in the focal plane for an extended period of time. We assume that these particles were either sterically hindered by irregular pore geometry or transiently adsorbed on the pore wall due to the same mechanism that causes the tailing problem in chromatography. To avoid their adverse effect on averaging, the median instead of the mean of the migration time distribution was used to calculate the particle migration velocity and mobility.

It is also noted that unlike capillary electrophoresis in silica columns, the particle migration direction is *opposite* to that of EOF direction in alumina nanopore electrophoresis. This is because silica surfaces are usually densely charged so that a large EOF flow is generated in such capillaries.[36-38] The result is that all particles will move with EOF in CE. In nanopores, the EOF generated by an alumina surface is much smaller compared to that generated by a silica surface.[36-38] The result is that the electric field drives the negatively charged particles going against the EOF toward the anode (from top to the bottom in Figure 1).

To confirm this, we measured the EOF in the nanopores using the same electrophoresis apparatus and the sitting-and-watching approach using Coumarin 540 dye. The focal plane was set right at the exit side of the membrane/buffer interface thus the total effective migration length was 60 μm. The neutral dye Coumarin 540A was used and was added to the bottom reservoir. Once the electric field was turned on, the acquisition of the images was also started. From the time it takes for Coumarin 540A to reach the focal plane at the opposite (top) side of the membrane, we were able to calculate the EOF mobility under that applied voltage (Supplementary Figure 3a). Two voltages, 1.5V and 1.0 V, were examined and the measured μ_{EOF} of 6.7×10^{-10} $m^2/s/V$ were

nearly identical, consistent with the literature reports. The fact that the same electroosmotic mobility was found at 2 different voltages indicate that the potential was applied correctly and neither the diffusion of coumarin nor surface charge on the membrane contributed to the observed μ_{EOF}. When no electric field was applied, no increase in the fluorescence signal was found at the focal plane. In fact, the observed fluorescence intensity decreased gradually over time as a result of photobleaching (Supplementary Figure 3b). This further confirms that the increase in dye concentration at the opposite side of the alumina membrane was not due to free diffusion of the molecules.

The estimated electrophoretic mobilities of the nanoparticles and the electroosmotic flow in the nanopores are listed in Table 1. In particular, for 1.0V or 1.5V applied on the ITO glasses, μ_{App} for either particle in either size pores were roughly same. Yet, these electrophoretic mobilities are significantly smaller than those measured in bulk experiments, i.e. capillary electrophoresis with a column diameter of 75 μm. The contributions of surface adsorption to the low mobilities in Table 1 can be assessed for differently sized nanoparticles moving in differently sized pores. The adsorption probability is proportional to the ratio of the surface area to the available volume (A/V, in units of nm^{-1}) inside the nanopores. For 85 nm particles in 100 nm and 200 nm pores, A/V is 1.09 and 0.026 respectively. For 50 nm particles, A/V is 0.060 and 0.022 respectively. That is, adsorption should affect each combination of particle and pore sizes significantly differently. Since all of the observed mobilities (for both particle sizes and both pore sizes) were similar, we can conclude that adsorption is not the primary reason for the decrease compared to bulk mobilities.

Diffusion of nanoparticles in nanopores. To fully understand the origin of slow migration of the nanoparticles in nanopores, we also investigated the axial diffusion behavior of the particles inside nanopores. The same sitting-and-watching approach was used except that no electric field

was applied and images were recorded by a CCD camera with an integration time of 50 ms for both 85 and 50 nm particles. The particles diffusing in and out of the focal plane are purely driven by thermal activity. The same fluorescence intensity fluctuation of the particles as a function of time was recorded (Supplementary Figure 4). To extract the diffusion coefficient of the nanoparticles in such a one-dimensional cylindrical tube, the autocorrelation function $G(\tau)$ of the fluorescence intensity fluctuation trace was calculated and fitted with the theoretical function of 1-D diffusion:[4]

$$G(\tau) = 1 + \frac{1}{N}\left(1 + \frac{4D\tau}{z_0^2}\right)^{-1/2} \qquad (8)$$

where N is the mean molecule number in the detection volume; D is the diffusion coefficient, and z_0 is the focal plane thickness. Fitting provides better statistics than simply monitoring the trajectory of individual particles over time.

By fitting Equation 8 (Figure 5) to more than 30 intensity fluctuation traces each containing 1000 consecutive images, we obtained the diffusion coefficients in 200 nm nanopores to be 2.4×10^{-13} m^2/s for 85 nm particles and 3.7×10^{-13} m^2/s for 50 nm particles (Table 2). These diffusion coefficients can alternatively be predicted by the Einstein–Stokes equation:

$$D = \frac{k_B T}{6\pi\eta R} \qquad (9)$$

where k_B is the Boltzmann constant and T is the temperature. The theoretical values in water (η=1) are 5.0×10^{-12} m^2/s for 85 nm particles and 8.5×10^{-12} m^2/s for 50 nm particles, and are 20 times and 23 times larger than the corresponding diffusion coefficients measured here in the nanopores.

Consistency of anomalous diffusion coefficients and electrophoretic mobilities in nanopores. It is interesting to note that the nanoparticles show both slow electromigration and

slow diffusion in nanopores. More importantly, the decreased factors are roughly the same for diffusion and migration and for either size of particles, pointing towards a common mechanism. Specifically, for 85 nm particles, electrophoretic migration slows down by a factor of ~28 while diffusion slows down by a factor of 20 (Tables 1 and 2). Similarly, the 50 nm particles have a mobility ~22 times smaller and a diffusion coefficient 23 times smaller.

We further note that the transit times through the focal plane in the electromigration experiments are much shorter than in the free diffusion experiments, being subsecond in Figure 4 vs. seconds in Figure 5. The contribution of surface adsorption to our measurements should thus be much less in the former case compared to the latter case. Adsorption can also be ruled out since the difference in A/V inside the nanopores did not result in a difference for the two particle sizes in two different pore sizes, *vide supra*. The fact that all motions show the same retardation compared to bulk solution indicates that the microenvironment inside the nanopores is different from that in the bulk solution.

It has been shown that the intraparticle obstruction factor in size-exclusion chromatography can result in up to a factor of 100 difference in apparent diffusion coefficients inside the pores versus in bulk.[40] Here, tortuosity and constriction can be rule out, *vide supra*. If the Smoluchowski equation (Equation 5) and Einstein-Stokes Equation (equation 10) both hold in the nanopore environment:

$$D_{Pore} = \frac{k_B T}{6\pi\eta_{Pore} R} \qquad (11)$$

$$\mu = \frac{q}{6\pi\eta_{Pore} R} \qquad (12)$$

where the subscript "*Pore*" denotes the apparent values measured in the nanopores, we can obtain the apparent viscosity η_{Pore} from both the electrophoretic migration and the diffusion experiments.

The conclusion is that the apparent viscosity in the nanopore environment is 20~28 times larger than that in bulk solution. Finally, this increase in viscosity is also in the same order as the factor of 100 increase observed for the diffusion of protein molecules in PEG-coated polycarbonate nanopores compared to bulk solution.[26]

Conclusion

The objective for this study is to find the origin of the extremely slow axial diffusion of molecules/particles in nanopores. We measured the electrophoretic motion of individual polystyrene nanoparticles in cylindrical alumina nanopores with different size combinations. The axial diffusion of the particles in the pores is also measured. It is found that the electrophoretic mobilities and the diffusion coefficients of particles were both substantially smaller compared to those in the bulk solution, independent of particle size or pore diameter. The effective A/V ratio inside the nanopores cannot account for the difference between the two particle sizes in two different pore sizes, indicating adsorption can also be ruled out. While this phenomenon requires further investigation, we suggest that the microenvironment in the nanopores is anomalous. The electrophoretic mobility and diffusion experiments both point to the scenario that the apparent macroscopic viscosity is anomalously large in the nanopores.

Acknowledgments

R.H and G.W contributed to the paper equally. The Ames Laboratory is operated for the U.S. Department of Energy by Iowa State University under Contract No. DE-AC02-07CH11358. This work was supported by the Director of Science, Office of Basic Energy Science, Division of Chemical Sciences.

References

(1) Masuda, H.; Fukuda, K. *Science* 1995, *268*, 1466.

(2) Nielsch, K.; Choi, J.; Schwirn, K.; Wehrspohn, R. B.; Gosele, U. *Nano Letters* 2002, *2*, 677.

(3) Hernandez, A.; Calvo, J. I.; Pradanos, P.; Palacio, L.; Rodriguez, M. L.; de Saja, J. A. *Journal of Membrane Science* 1997, *137*, 89.

(4) Hohlbein, J.; Steinhart, M.; Schiene-Fischer, C.; Benda, A.; Hof, M.; Hubner, C. G. *Small* 2007, *3*, 380.

(5) Velleman, L.; Triani, G.; Evans, P. J.; Shapter, J. G.; Losic, D. *Microporous and Mesoporous Materials* 2009, *126*, 87.

(6) Losic, D.; Cole, M. A.; Dollmann, B.; Vasilev, K.; Griesser, H. J. *Nanotechnology* 2008, *19*.

(7) Lee, H. J.; Yasukawa, T.; Suzuki, M.; Lee, S. H.; Yao, T.; Taki, Y.; Tanaka, A.; Kameyama, M.; Shiku, H.; Matsue, T. *Sensors and Actuators B: Chemical* 2009, *136*, 320.

(8) Venkatesan, B. M.; Dorvel, B.; Yemenicioglu, S.; Watkins, N.; Petrov, I.; Bashir, R. *Advanced Materials* 2009, *21*, 2771.

(9) Chen, P.; Gu, J. J.; Brandin, E.; Kim, Y. R.; Wang, Q.; Branton, D. *Nano Letters* 2004, *4*, 2293.

(10) Losic, D.; Simovic, S. *Expert Opinion on Drug Delivery* 2009, *6*, 1363.

(11) Gultepe, E.; Nagesha, D.; Sridhar, S.; Amiji, M. *Advanced Drug Delivery Reviews* 2010, *62*, 305.

(12) Adiga, S. P.; Jin, C. M.; Curtiss, L. A.; Monteiro-Riviere, N. A.; Narayan, R. J. *Wiley Interdisciplinary Reviews: Nanomedicine and Nanobiotechnology* 2009, *1*, 568.

(13) Chu, S. Z.; Wada, K.; Inoue, S.; Todoroki, S. *J. Journal of The Electrochemical Society* 2002, *149*, B321.

(14) Dileo, A. J.; Allegrezza, A. E.; Builder, S. E. *Biotechnology* 1992, *10*, 182.

(15) El-Safty, S.; Shenashen, M. A. *Analytica Chimica Acta* 2011, *694*, 151.

(16) Striegel, A. M. *Analytical Chemistry* 2005, *77*, 104 A.

(17) Ludes, M. D.; Anthony, S. R.; Wirth, M. J. *Analytical Chemistry* 2003, *75*, 3073.

(18) Ludes, M. D.; Wirth, M. J. *Analytical Chemistry* 2002, *74*, 386.

(19) Wirth, M. J.; Ludes, M. D.; Swinton, D. J. *Analytical Chemistry* 1999, *71*, 3911.

(20) Wirth, M. J.; Swinton, D. J. *Analytical Chemistry* 1998, *70*, 5264.

(21) Huang, X. Y.; Doneski, L. J.; Wirth, M. J. *Analytical Chemistry* 1998, *70*, 4023.

(22) Yamaguchi, A.; Uejo, F.; Yoda, T.; Uchida, T.; Tanamura, Y.; Yamashita, T.; Teramae, N. *Nature Materials* 2004, *3*, 337.

(23) Ku, A. Y.; Taylor, S. T.; Heward, W. J.; Denault, L.; Loureiro, S. M. *Microporous and Mesoporous Materials* 2006, *88*, 214.

(24) Harrell, C. C.; Lee, S. B.; Martin, C. R. *Analytical Chemistry* 2003, *75*, 6861.

(25) Choi, Y.; Baker, L. A.; Hillebrenner, H.; Martin, C. R. *Physical Chemistry Chemical Physics* 2006, *8*, 4976.

(26) Ma, C. B.; Yeung, E. S. *Analytical Chemistry* 2010, *82*, 478.

(27) Ma, C. B.; Yeung, E. S. *Analytical Chemistry* 2010, *82*, 654.

(28) Mirsaidov, U.; Comer, J.; Dimitrov, V.; Aksimentiev, A.; Timp, G. *Nanotechnology* 2010, *21*.

(29) Nagumo, R.; Takaba, H.; Nakao, S. I. *Chemical Physics Letters* 2008, *458*, 281.

(30) Kievsky, Y. Y.; Carey, B.; Naik, S.; Mangan, N.; ben-Avraham, D.; Sokolov, I. *The Journal of Chemical Physics* 2008, *128*, 151102.

(31) Rivera, D.; Harris, J. M. *Analytical Chemistry* 2001, *73*, 411.

(32) Ma, C. B.; Han, R.; Qi, S. D.; Yeung, E. S. *Journal of Chromatography A* 2012, *1238*, 14.

(33) Sun, W.; Wang, G.; Fang, N.; Yeung, E. S. *Analytical chemistry* 2009, *81*, 9203.

(34) Potschka, M. *Journal of Chromatography A* 1993, *648*, 41.

(35) Fang, N.; Zhang, H.; Li, J. W.; Li, H. W.; Yeung, E. S. *Analytical Chemistry* 2007, *79*, 6047.

(36) Ai, Y.; Yalcin, S. E.; Gu, D. F.; Baysal, O.; Baumgart, H.; Qian, S. Z.; Beskok, A. *Journal of Colloid and Interface Science* 2010, *350*, 465.

(37) Vajandar, S. K.; Xu, D. Y.; Markov, D. A.; Wikswo, J. P.; Hofmeister, W.; Li, D. Y. *Nanotechnology* 2007, *18*.

(38) Gupta, A.; Denver, H.; Hirsa, A. H.; Stenken, J. A.; Borca-Tasciuc, D. A. *Applied Physics Letters* 2007, *91*.

(39) Smoluchowski, M. *Annalen der Physik* 1906, *21*, 756.

(40) Richard, D. J.; Striegel, A. M. *Journal of Chromatography A* 2010, *1217*, 7131.

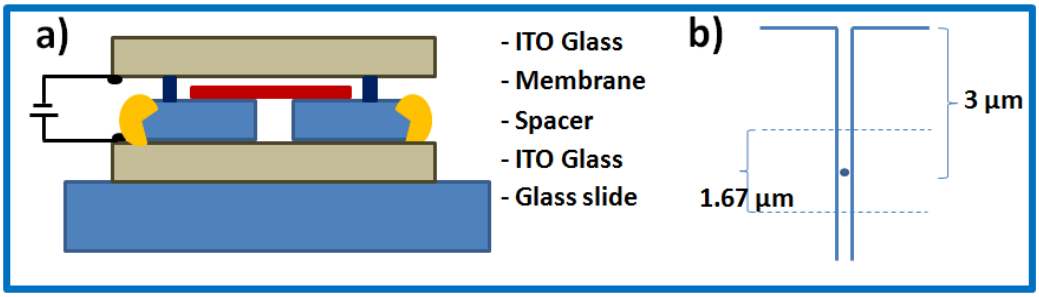

Figure 1. Schematic of the experimental setup for nanopore electrophoresis. (a) The sandwich setup for the electrodes and nanoporous membrane. (b) The observation geometry. The focal plane was set at 3 µm below the surface of the porous membrane and the aqueous solution. The full width at half maximum of the focal depth was measured to be 1.67 µm. The graph was drawn to scale.

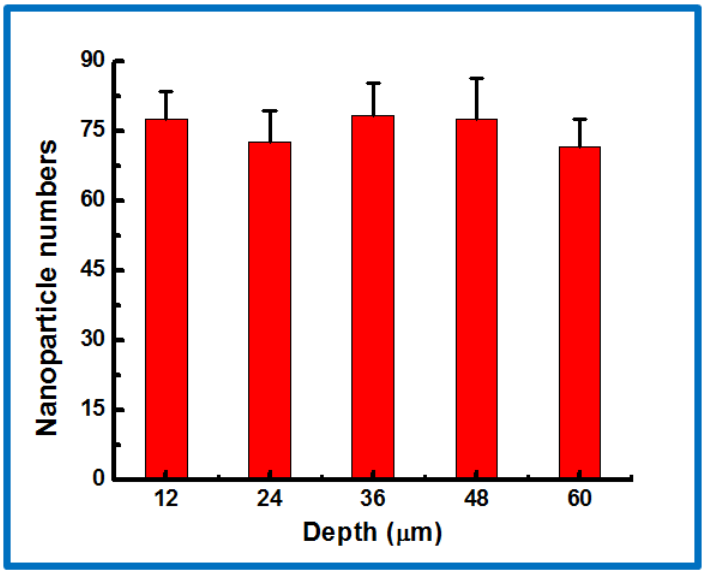

Figure 2. Vertical distribution of 100 nm particles in an alumina porous membrane with 200 nm pores after equilibrium was established. The particle numbers are the total counts at depths spaced every 12 μm.

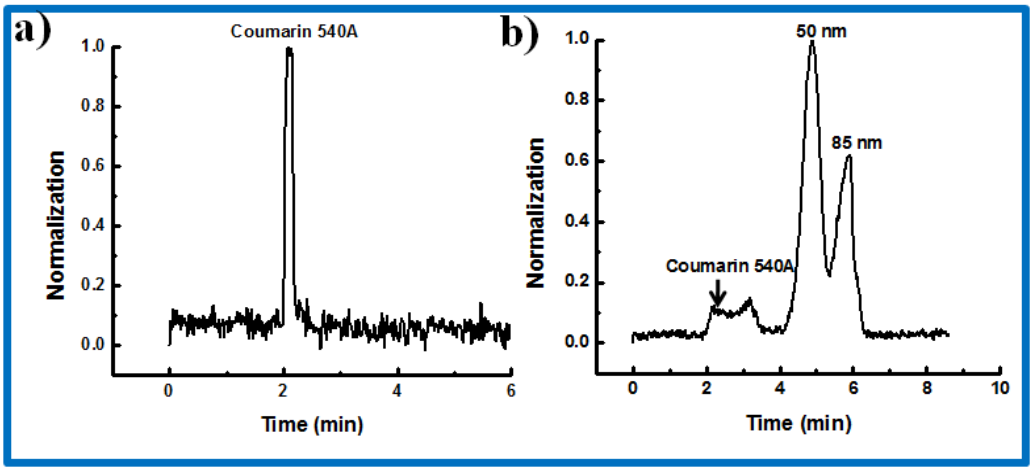

Figure 3. Capillary electropherograms of (a) coumarin 540A only, and (b) mixtures of coumarin 540A, 85 nm and 50 nm particles. Coumarin adsorbs onto the nanoparticles and slows down when placed in the same solution, so a distorted peak is observed in (b) compared to (a). The CE experiments were run in 25 mM CHES buffer at pH 9.0. The observed electrophoretic mobilities of the 85 and 50 nm particles are listed in Table 1.

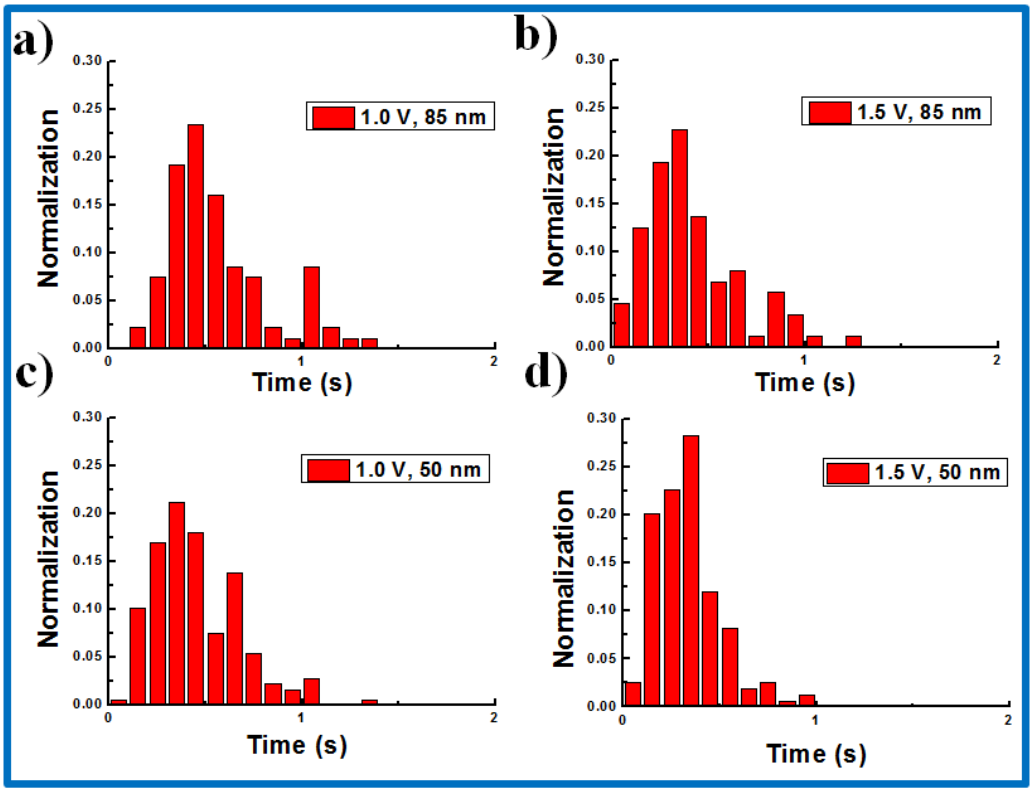

Figure 4. Histogram of electrophoretic migration times of 85 nm and 50 nm particles going through the focal plane of a 100× microscope objective (a distance of 1.67 μm) in 200 nm cylindrical nanopores. (a) and (b) are for 85 nm particles; (c) and (d) are for 50 nm particles. The indicated voltages are the total voltage applied across the 2 ITO glasses.

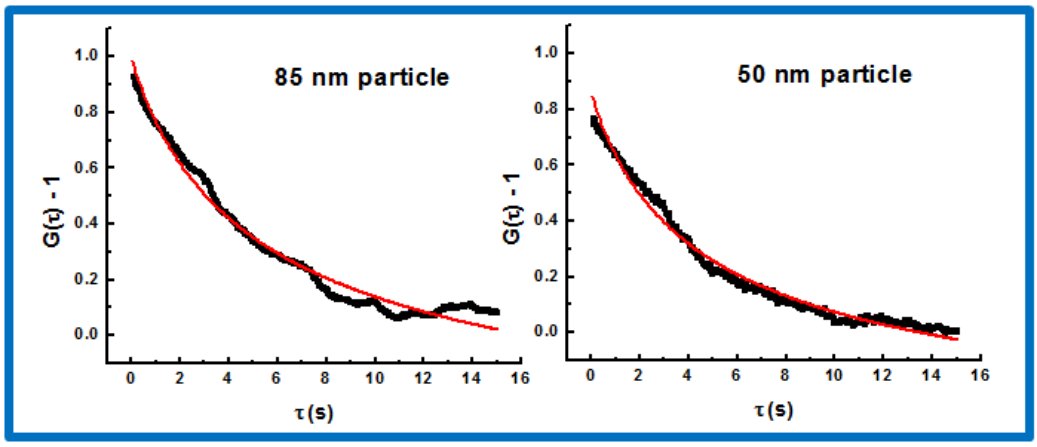

Figure 5. Autocorrelation functions and theoretical fittings of the fluorescence intensity fluctuation traces caused by single particles diffusing in one-dimensional cylindrical nanopores. (a) 85 nm particles. (b) 50 nm particles. The black curves are the experimentally obtained autocorrelation functions and the red curves are the theoretical fits.

Table 1. Electrophoretic mobilities ($m^2V^{-1}s^{-1}$) of nanoparticles and solution electroosmotic mobilites. By convention, the EOF direction is always positive. All velocities and electrophoretic mobilities are vectors.

	100 nm nanopores		**200 nm nanopores**		**Bulk**
	1.0 V	1.5 V	1.0 V	1.5 V	CE
85 nm particles					
μ_{Ep}^{Bulk}	-	-	-	-	-4.4×10^{-8}
μ_{App}^{Pore}	-1.1×10^{-9}	-1.1×10^{-9}	-0.87×10^{-9}	-0.68×10^{-9}	-
μ_{ep}^{Pore}	-1.8×10^{-9}	-1.7×10^{-9}	-1.5×10^{-9}	-1.3×10^{-9}	-
$\mu_{Ep}^{Bulk}/\mu_{Ep}^{Pore}$	25	26	29	33	-
50 nm particles					
μ_{Ep}^{Bulk}	-	-	-	-	-3.9×10^{-8}
μ_{App}^{Pore}	-1.4×10^{-9}	-1.2×10^{-9}	-0.95×10^{-9}	-0.78×10^{-9}	-
μ_{Ep}^{Pore}	-2.0×10^{-9}	-1.9×10^{-9}	-1.6×10^{-9}	-1.5×10^{-9}	-
$\mu_{Ep}^{Bulk}/\mu_{Ep}^{Pore}$	19	20	24	26	-
EOF					
μ_{EOF}	-	-	$+6.7\times10^{-10}$	-	$+7.0\times10^{-8}$

Table 2. Apparent axial diffusion coefficients of nanoparticles.

85 nm particle		
	Experimental data	Bulk theory
D (m^2s^{-1})	2.4×10^{-13}	5.0×10^{-12}
D^{Bulk} / D^{Pore}	20	-
50 nm particle		
	Experimental data	Bulk theory
D (m^2s^{-1})	3.7×10^{-13}	8.5×10^{-12}
D^{Bulk} / D^{Pore}	23	-

Supplementary Information

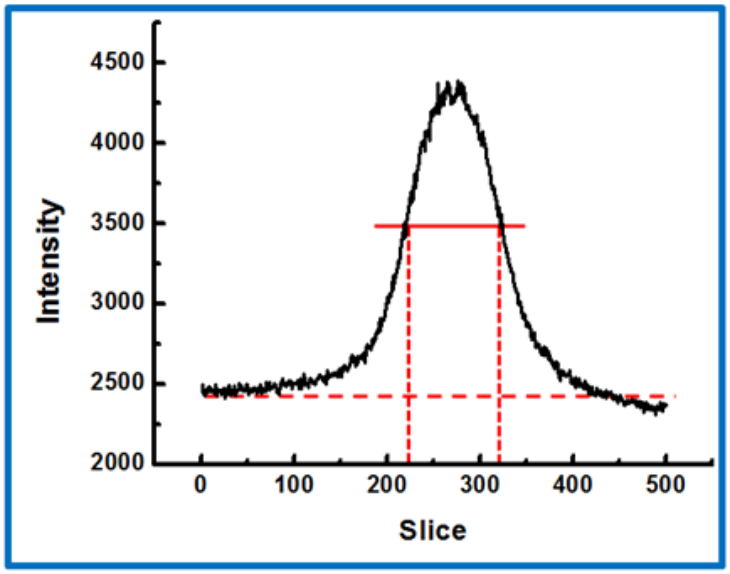

Supplementary Figure 1. An example of the fluorescence intensity as a function of axial position for 85 nm particles immobilized on the glass surface.

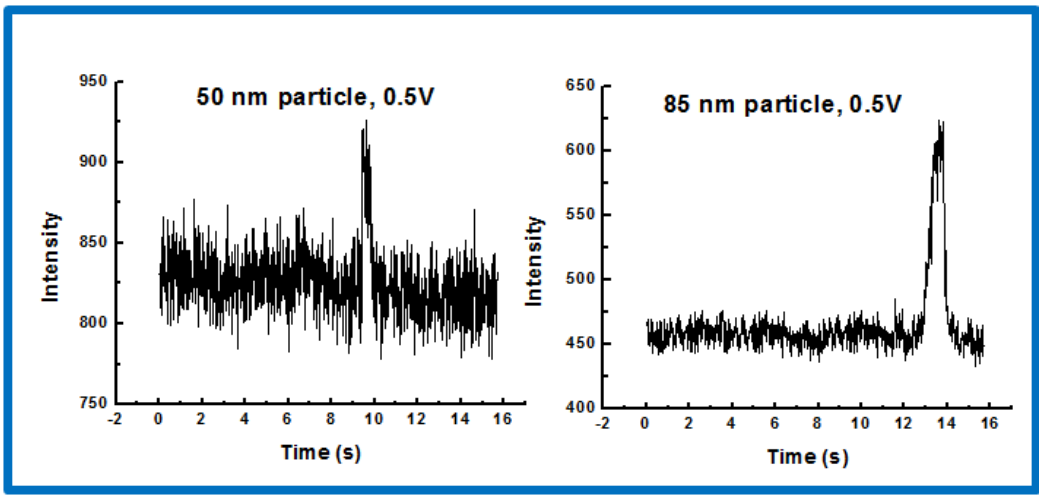

Supplementary Figure 2. Examples of fluorescence intensity-time traces of migrating nanoparticles passing through the microscope focal plane under an applied voltage. The camera gain was adjusted according to signal strengths for the best signal-to-noise ratio for particles with different sizes.

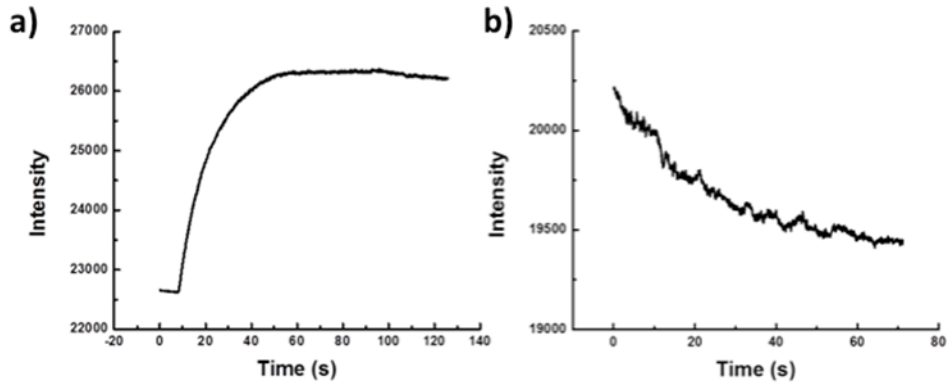

Supplementary Figure 3. a) Fluorescence intensity of Coumarin 540A migrating with the electroosmotic flow under 1.0 V applied voltage. . b) Fluorescence intensity of Coumarin 540A in control experiment, i.e., without applied voltage.

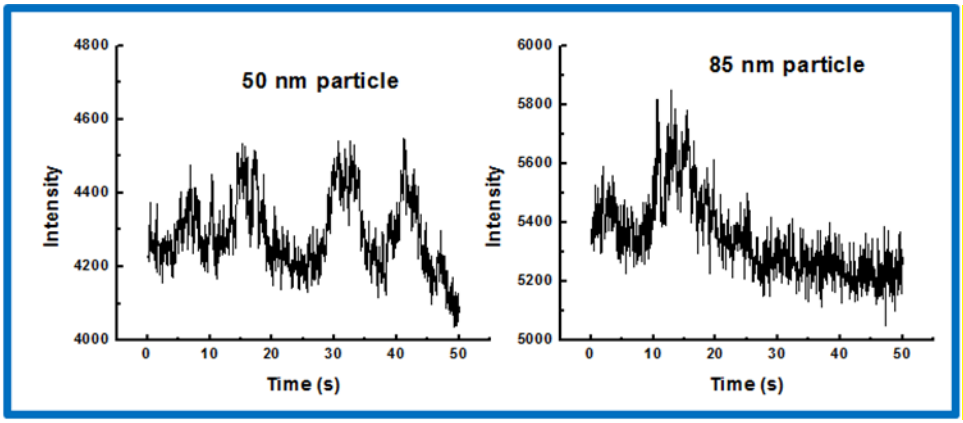

Supplementary Figure 4. Examples of fluorescence intensity-time traces of diffusing nanoparticles going into and out of the microscope focal plane inside cylindrical nanopores.

CHAPTER 3. GOLD NANOPARTICLES AS DRUG DELIVERY VEHICLE AND IMAGING CONTRAST PROBES IN STEM CELLS PROLIFERATION

Rui Han, Eun-ah Ye, Donald Sakaguchi, Ning Fang

A paper to be submitted

Abstract

Plasmonic gold nanoparticles (AuNPs) have been demonstrated to be stable and versatile optical imaging probes. Recently, we have developed differential interference contrast (DIC) microscopy based techniques to track single plasmonic nanoparticle in cellular environments. The present study demonstrates an effort to realize the full potential of new optical imaging techniques in stem cell research. AuNPs were dual-surface modified with basic fibroblast growth factor (bFGF) and cell penetrating peptide, and they served as both drug delivery carriers and optical imaging probes. The results showed that functionalized AuNPs were delivered to the stem cells efficiently and stimulate stem cell proliferation successfully.

Introduction

Because of strong localized surface plasmon resonance (LSPR) enhanced absorption and scattering, as well as biocompatibility and photo stability,[1-7] AuNPs have been widely used as optical imaging contrast agents and drug delivery carriers in biological and medical applications.[8-15] These research efforts generally consist of three main components: optical microscopy and spectroscopy, nanoparticle surface modification, and biological functions. Several optical microscopy techniques have been developed to visualize AuNPs in biological samples, including dark field microscopy,16-20 total internal reflection scattering microscopy (TIRSM),21-24

confocal microscopy,25-27 and differential interference contrast (DIC) microscopy.28-32 Among all of these imaging tools, DIC microscopy has been demonstrated to be especially suitable for biological imaging of AuNPs because it causes little disruption to cellular functions at a low level of illumination intensity and generates high contrast images for AuNPs with less interference from the surrounding. Furthermore, dual-wavelength DIC microscopy technique has been developed to differentiate AuNPs from other cellular features, such as endocytic vesicles in complex cellular environments.33-35 AuNPs show drastically different contrasts at the LSPR and non-LSPR wavelengths, while the rest of cellular features show similar contrasts at both wavelengths.

AuNPs can be readily surface-modified with peptides,[36-38] proteins,[39,40] and DNAs and massager RNAs(mRNAs)[41,42] for therapeutic and diagnostic purposes. For example, AuNPs were surface modified with TAT peptide, a cell penetration peptide from the HIV-1 protein TAT (residues 47-57: YGRKKRRQRRR), to facilitate the internalization of these particles into cells with high efficiency.[36,38,43] AuNPs modified with specific DNA to differentiate different cell types was also reported. Yang et al. reported they used DNA and AuNPs conjugated to identify cancer cells.[19]

Realizing the full potential of new physical science tools, such as the advanced imaging techniques, in biological and medical research is not a trivial task. The present study demonstrates an effort to maximize the capabilities of the DIC microscopy based plasmonic nanoparticle imaging techniques in stem cell research. More specifically, 60-nm AuNPs functionalized with basic fibroblast growth factor (bFGF) were delivered into adult hippocampal progenitor cells (AHPCs) to stimulate cell proliferation. The distributions of AuNPs in live and fixed cells were studied quantitatively.

bFGF is the primary inducer of mesoderm formation in embryogenesis, and it is involved in a variety of biological processes including cell proliferation, astrocytomas and angiogenesis, which makes bFGF a potent regulator of wound repair, angiogenesis, and neural outgrowth.[44-46] These functions are mediated by interactions with FGF receptors to activate the tyrosine kinase and bFGF signal pathway and subsequent alterations in gene expression within responsive cells.[47-50] The delivery of bFGF into cells has been accomplished by several different carriers, including mesoporous silica nanoparticles,[51,52] chitosan–fucoidan nanoparticles,[53] and polymer complex,[54] and AuNPs.[55] Szlachcic *et al*. used AuNPs to deliver bFGF into cancer cells, and they demonstrated that localized heating by irradiating AuNPs with near-infrared (NIR) light can destruct FGF receptors and eventually kill cancer cells[55].

As one of the heparin-binding growth factor (HBGF) family proteins, bFGF has a high affinity for heparin and similar molecules. Heparin and heparin like molecules are required for bFGF to bind with FGF receptors.[56] At least four distinct receptors for bFGF have been discovered (FGF receptor 1[57], FGF receptor 2[58], FGF receptor3[59], and FGF receptor 4[60]). Generally, these FGF receptors can be divided in two groups, high-affinity receptors and low-affinity receptors. bFGF binding with FGF receptor confined AuNPs conjugated with bFGF,[61] which enables us to determine spatial distribution of FGF receptor in adult hippocampal progenitor cells (AHPCs).

AHPCs are self-renewing, multi-potent neural progenitors that have the ability to differentiate into neurons, oligodendrocytes, and astrocytes. AHPCs continuously give rise to new neurons throughout life, which might be an important determinant of hippocampus-dependent function.[62] Identification and location of FGF receptor can supply more information to better understand the functional role of bFGF. Typically, the cellular localization of FGF receptor has been studied by immunohistochemistry and in situ hybridization.[50,63,64] In this work, we designed and tracked

multi-functional AuNPs to supply a potential method to locate FGF receptors in fixed and live AHPCs.

Experimental Section

Materials and chemicals. TAT peptide (residues 47-57: YGRKKRRQRRR; cat. no.60023-1) was purchased from Ana Spec (San Jose, CA). PEG-NHS ester disulfide (4,7,10,13,16,19,22,5,32,35,38,41,44,47,50,53-hexadecaoxa-28,29 dithiahexapentacontanedioic acid di-*N*-succinimidyl ester) and FGF receptor inhibitor SU-5402 were purchased from Sigma-Aldrich (St. Louis, MO). Human bFGF, with a molecular weight of 17.5 kDa and containing 154 amino acids, was purchase from Promega (Madison, WI). Human bFGF enzyme linked immunosorbent assay (ELISA) kit was purchased from Life Technologies (NY, USA.) The 60-nm citrate-capped gold colloidal solutions were purchased from BBI International (Cardiff, U.K.). The absorption spectra of the AuNP colloidal solutions were measured by a UV-Vis spectrophotometer (Varian Cary 300). AuNP colloidal's concentration and size distribution were verified by transmission electron microscopy, and the results agreed well with the manufacturer's data, which are 4.3175×10^{-11} mol/L and 60 ± 3 nm.

DIC microscope. An upright Nikon Eclipse 80i microscope was used in this work. The DIC mode used a pair of Nomarski prisms, two polarizers, a 100× / 1.40 numerical aperture (NA) Plan Apo oil immersion objective, and a 1.40 NA oil immersion condenser. Movies and images were captured with a Hamamatsu Orca Flash2.8 CMOS camera (1920 × 1440 imaging array with a pixel size of 3.63 μm × 3.63 μm). When the DIC microscope was operated at a single wavelength, a proper band pass filter was inserted in the light path of the microscope. Band pass filters with central wavelengths in the range of 450 - 700 nm and a full width at half-maximum (FWHM) of

10 nm were purchased from Thorlabs (Newton, NJ). When the DIC microscope was operated at two wavelengths simultaneously, a Photometrics DV2 two-channel imaging system (Tucson, AZ) with a 565 nm dichroic filter and two sets of proper filters were installed. Movies and images were analyzed with NIH ImageJ (http://rsbweb.nih.gov/ij/).

A computer-controlled rotary motor from Sigma Koki (model no. SGSP-60YAM) was coupled to the actuator of the microscope stage. The CMOS camera and the stage were synchronized by a home-written computer program. The motor speed and the camera's exposure time were optimized according to DIC image contrasts.

Dual modification of AuNPs with TAT and bFGF. Figure 1A showed the two-step scheme of the dual-surface modification of the 60-nm AuNPs with TAT peptide and bFGF through a PEG-NHS ester disulfide linker, which has both disulfide for chemisorption to the gold surface and a succinimidyl functional group for the facile covalent coupling of TAT and bFGF. It should be noted that the N-terminus of bFGF is an appropriate location for conjugation with PEG-NHS disulfide, which is on the opposite side of the binding sites for FGF receptor and heparin. This functionalization strategy does not affect bFGF's ability to bind heparin and activate FGF receptors.[61,65-67]

Briefly, 40 μL of 0.2-mM PEG-NHS ester disulfide solution prepared in 50-mM pH 7.2 borate buffer was added to 1.0 mL of the AuNP solution and mixed for 3 h. The solution was then cleaned up by centrifugation and resuspension in 2-mM borate buffer. 0.2 μg of TAT peptide and 20 μg of bFGF were added together to the AuNP solution and reacted at room temperature for 3 h. The solution was cleaned up again by centrifugation and resuspension in Earle's Balanced Salt Solution (EBSS, Invitrogen, Carlsbad, CA) several times to remove free TAT and bFGF and finally stored in 100 μL of EBSS solution at -20°C.

The concentrated bFGF-TAT-AuNP colloidal solution was diluted in the cell culture medium to a final concentration of ~2.6 $\times 10^9$ particles/mL. The final particle concentration was estimated from the number of dilutions, and it was assumed that no particle was lost during the modification procedure.

Figure 1B shows the UV-Vis spectrum of the original AuNP colloid solution and the bFGF-TAT-AuNP colloid solution in cell culture medium. The LSPR peak for the functionalized AuNP solution was found red-shifted by ~ 20 nm. The zeta potentials of bFGF-TAT-AuNPs in DI water and cell culture medium were measured to be +20.2 mV and +25.3 mV, respectively, with Nano-ZS90 Zetasizer (Malvern Instruments, United Kingdom).

Quantification of surface coverage of bFGF on AuNPs. The amount of bFGF bound to AuNPs was quantified by a colorimetric ELISA kit. The supernatant was taken out of the functionalized AuNP solution after centrifugation and diluted by 100,000 fold. The amount of unbound bFGF in the diluted supernatant was quantified with bFGF ELISA kit following the manufacturer's protocol, and then the total amount of bFGF in bFGF-TAT-AuNPs was calculated. Also the concentration of AuNPs is known, so the bFGF surface coverage on each AuNP can be calculated and the corresponding value is 250 bFGF molecules on one AuNP.

Cell culture. AHPCs were planted on the glass coverslips coated with poly-L-ornithine (10 μg/mL, Sigma-Aldrich) and laminin (10 μg/mL in Earle's Balanced Salt Solution, BD Biosciences, Bedford, MA) at an initial density of ~1,000 cells per coverslip. The AHPCs were propagated in complete medium containing Dulbecco's modified Eagle's medium/Ham's F-12 (DMEM/F-12, 1:1; Omega Scientific, Tarzana, CA) supplemented with N2 (Gibco BRL, Gaithersburg, MD), 20 ng/ml basic fibroblast growth factor (Promega Corporation, Madison, WI), and 2.5 mM L-glutamine (Gibco BRL, Gaithersburg, MD).[68]

Results and Discussion

Cytotoxicity of AuNPs. We first studied the cytotoxicity of AuNPs with different surface ligands to AHPCs. Figure 2 shows the cell viability after three-day incubation of AHPCs in seven culture conditions. The first four conditions were culture medium with bare-AuNPs, TAT-AuNPs, bFGF-TAT-AuNPs and TAT peptide which were substituted 20 ng/mL bFGF. Another three culture condition groups were control groups: Modified minimal essential culture medium (MM), culture medium of Dulbecco's modified Eagle's medium/Ham's F-12 without bFGF (DM), and ethanol. Here, it should be noted that MM culture medium is the culture medium with 20ng/mL bFGF, in which the AHPCs are stimulated to proliferate. In these experiments, AuNPs, TAT peptide, and bFGF, if present, were at the same total concentrations in the corresponding cell culture medium to ensure fair comparisons. Plot of culture condition cytotoxicity showed that after 24 h exposure to cells except ethanol culture condition, all the others culture conditions includes bFGF-TAT-AuNPs are essentially non-toxic to AHPCs.

Effects of bFGF-TAT-AuNPs on AHPCs proliferation and differentiation. To examine the proliferation effect bFGF-TAT-AuNPs to AHPCs and to optimize the bFGF-TAT-AuNPs culture amount, cells were treated with various concentration of bFGF-TAT-AuNPs. The amount of bFGF-TAT-AuNPs added to the culture medium matched the bFGF amount in normal MM culture condition (20ng/mL bFGF), and this concentration was recorded as 1×. AHPCs were cultured with 0.001×, 0.01×, 0.1×, 1×, 2×, and 5× fold bFGF-TAT-AuNPs for 96 hours, followed by AHPCs cultured in the previous culture condition were processed for immunocytochemistry. First, fixed cells were incubated in blocking solution (5% normal donkey serum, 0.4% bovine serum albumin, and 0.2% Triton X-100) followed by incubation with primary antibodies overnight

at 4°C. Then cells were incubated in the appropriate biotinylated secondary antibodies, followed by incubation with streptavidin-conjugated Cy3 and nuclei were stained with 4', 6-diamidino-2-phenylindole, dilactate (DAPI). Images of 12 microscopic fields (0.24 mm^2/field) from 4 parallel experiments in each culture condition were randomly taken to count the cells, as shown Figure 3. Figure 3B showed the statics cell number in each culture condition, and AVONA test showed no significant difference of concentration effect among 0.1×, 1×, 2× and 5× culture condition, thus here we chose 0.1× bFGF-TAT-AuNPs in all next experiments.

In Figure 4, six culture condition groups are shown to compare the proliferation efficiency of bFGF and bFGF-TAT-AuNPs. Figure 4C showed cell imaging of DM group, in which contained no bFGF, the cells cultured continually in four days increased much less slowly compared with Figure 4A, MM and Figure 4B, bFGF-TAT-AuNPs groups. Cell numbers in bFGF-TAT-AuNPs and MM culture medium were not significantly different, but it should be noted that bFGF in bFGF-TAT-AuNPs was 1/10 of bFGF in MM culture medium. As Wissink *et al.*[69] reported that one heparin can bind 8 to 13 bFGF molecules, and the bind possibility between bFGF and immobilized heparin is 1/1000, thus amount of free bFGF should be much higher than the heparins to get a saturation binding with heparin. However, 0.1×bFGF-TAT-AuNPs showed higher proliferation efficiency compared with MM groups. This may be explained by higher local bFGF concentration on one AuNP. The higher density of bFGF on one AuNP results a larger chance to bind with heparin, and thus brings higher proliferation efficiency in bFGF-TAT-AuNPs culture condition.[53,54,70-75]

We also compared differentiation effects of bFGF-TAT-AuNPs and bFGF to AHPCs. AHPCs were cultured for seven days (one differentiation cycle) and fixed, and then were stained with TUJ1 and RIP. TUJ1 (class III β-tubulin, mouse monoclonal IgG; R&D Systems) and RIP

(receptor interacting protein, mouse monoclonal IgG; Developmental Studies Hybridoma Bank) are both antibodies against phenotypic markers, TUJ1 for young neuronal cells and RIP for oligodendrocytes. To calculate the percentage of immunoreactive AHPCs stained with TUJ1 and RIP, the number of cells which were immuno-reactive for TUJ1 or RIP antibodies was divided by the total number of cells (DAPI-stained nuclei). Results in Figure 5 showed no significant difference on oligodendrocytes, however, bFGF-TAT-AuNPs and MM both showed lower percentage of TUJ1 labeled neuron cells, and otherwise, the differentiation efficiencies in the bare AuNPs and DM groups were not significantly different. These results indicated the bFGF-TAT-AuNPs effect on AHPCs differentiation is consistent with bFGF.

Effects of inhibitor. Determination of FGF receptor spatial distribution is acquired via locating bFGF-TAT-AuNPs based on binding of bFGF-TAT-AuNPs with FGF receptor. It's important to confirm the binding affinity between FGF receptor and bFGF-TAT-AuNPs was not affected by the conjugation of bFGF on AuNPs. Also as an additional factor to check bFGF-TAT-AuNPs effect on immunological response of AHPCs, inhibition experiment was also examined.

SU5402 is a pharmacological inhibitor of FGF receptor tyrosine kinases. It can specifically interact with the intracellular catalytic domain of FGF receptors irreversibly to block the bFGF signal activity,[76] which make it be a potential therapeutic agents for various human diseases.[77] In this experiment, 10 nM SU5402 was cultured with AHPCs, after four days culture, AHPCs were counted, as shown in Figure 6. The inhibitor effect did not show significant difference in both of bFGF and bFGF-TAT-AuNPs culture conditions. This may contribute to higher affinity between inhibitor and FGF receptors compared with bFGF-TAT-AuNPs and receptors. Binding interaction between inhibitor and FGF receptor is dominate in the binding competition of inhibitor and bFGF to FGF receptor. bFGF local density in bFGF-TAT-AuNPs is much higher than that in MM culture

medium, however, which did not enhance the affinity between bFGF-TAT-AuNPs and FGF receptor to a comparable level of the affinity between inhibitor and FGF receptor, which indicates there may be an opportunity to allow us to locate bFGF at its native status.

Wavelength-dependent DIC images of AuNPs. Identification of AuNPs in cells is based on their wavelength dependent image contrast by dual-wavelength DIC microscopy. Figure 7A and B showed AuNP and vesicle images on coverslip and in AHPCs. May due to the interaction between the particle and cell proteins or local culture medium, AuNPs DIC contrast is slightly weaker in cell (1.56 ± 0.26 at 540 nm, and 0.45 ± 0.18 at 700 nm) than on glass surface (1.67 ± 0.19 at 540 nm, and 0.58 ± 0.15 at 700 nm). Figure 7C shows DIC contrast spectra of vesicles, AuNPs, and aggregates. Here we measured AuNPs, vesicles and aggregates DIC contrast at 450 nm, 500 nm, 520 nm, 540 nm, 610 nm and 700 nm. The characteristic wavelength dependency is more evident in the DIC contrast spectra compiled in Figure 7C, the contrast difference among AuNPs, vesicles and aggregates is primal at 540 nm and 700 nm. Based on these findings, AuNPs can be identified in DIC microscopy at two wavelengths. Nikon DIC microscope was modified to catch images at two wavelengths simultaneously. The recombined beams after the second Nomarski prism is split into two channels by a beam splitter, each passing through a band-pass filter that selects the observation wavelength, and refocused to form two images on different portions of the same CCD camera chip. The two images are recorded simultaneously to minimize the external influence on the image quality. The contrast here is defined as the difference between the maximum and the minimum intensities over local background. After the bFGF was delivered to AHPCs, based on the various contrast of one particle at different wavelength channel, we can identify AuNPs from vesicles and aggregates. Moreover, 3D scans of fixed and live cells will

provide accurate information on the AuNPs location. This method allows us to count and localize AuNPs in fixed and live cells.

Counting particles in fixed and live cell. bFGF-TAT-AuNPs was first imaged in fixed AHPCs cells. The particles were added to a culture dish 2 hours after AHPCs were planted. Following four days culture, AHPCs were fixed and imaged. With the help of the 3D scanner, stacks of vertical sections of the cells were taken and each particle was counted at the location where contributed the best DIC contrast. Figure 9 showed the particle counting in fixed AHPCs. Images at four different depths were shown here as examples. It is challenging for traditional AuNPs counting method, such as TEM, ICP-MS, to achieve AuNPs counting in live cells. bFGF conjugated AuNPs bound with FGF receptor or heparin molecules, which will confine bFGF-TAT-AuNPs in a local area in cells, which supplied a good chance to locate the AuNPs with a 3D-scanner in live cells. Figure 10 showed the AuNPs counting in live AHPCs. AuNPs, vesicles and aggregates were marked respectively in Figure 10. AHPCs were cultured for 12 h, and were imaged in DIC microscopy with 3D-scanner. Scan speed was optimized to scan the whole cell effectively meanwhile to keep good AuNPs contrast. The total number of AuNPs in the cell shown in Figure 10 is 158. Also, it should be noted that in Figure 10B, the cell nucleus was also clearly imaged, which allowed us to distinguish if the particles were on the nucleus membrane. In this cell, several AuNPs were identified on the nucleus membrane.

Conclusion

In summary, the dual-wavelength DIC imaging method was used to locate, identify, and count AuNPs in fixed and live AHPCs. We have shown the biocompatibility (non-cytotoxicity and non-

immunogenicity) of AuNPs modified with bFGF. Furthermore, we demonstrated the application of bFGF conjugated AuNPs to proliferate AHPCs as an effective drug delivery carrier, which gives us a more widely biocompatible application in live cell, such as apply functionalizing AuNPs with various functions growth factor to characterize stem cells behaviors.

Acknowledgement

Thanks to Professor Donald S. Sakaguchi and Dr. Eun-ah Ye for AHPCs.

References

(1) Anker, J. N.; Hall, W. P.; Lyandres, O.; Shah, N. C.; Zhao, J.; Van Duyne, R. P. *Nature Materials* **2008**, *7*, 442.

(2) Jain, P. K.; Huang, X. H.; El-Sayed, I. H.; El-Sayed, M. A. *Accounts of Chemical Research* **2008**, *41*, 1578.

(3) Stewart, M. E.; Anderton, C. R.; Thompson, L. B.; Maria, J.; Gray, S. K.; Rogers, J. A.; Nuzzo, R. G. *Chemical Reviews* **2008**, *108*, 494.

(4) Chourpa, I.; Lei, F. H.; Dubois, P.; Manfait, M.; Sockalingum, G. D. *Chemical Society Reviews* **2008**, *37*, 993.

(5) Grant, S. A.; Spradling, C. S.; Grant, D. N.; Fox, D. B.; Jimenez, L.; Grant, D. A.; Rone, R. J. *Journal of Biomedical Materials Research Part A* **2014**, *102*, 332.

(6) Lewinski, N.; Colvin, V.; Drezek, R. *Small* **2008**, *4*, 26.

(7) Shukla, R.; Bansal, V.; Chaudhary, M.; Basu, A.; Bhonde, R. R.; Sastry, M. *Langmuir* **2005**, *21*, 10644.

(8) Levy, R.; Shaheen, U.; Cesbron, Y.; See, V. *Nano reviews* **2010**, *1*.

(9) Mandal, S.; Bakeine, G. J.; Krol, S.; Ferrari, C.; Clerici, A. M.; Zonta, C.; Cansolino, L.; Ballarini, F.; Bortolussi, S.; Stella, S.; Protti, N.; Bruschi, P.; Altieri, S. *Applied Radiation and Isotopes* **2011**, *69*, 1692.

(10) Pissuwan, D.; Niidome, T.; Cortie, M. B. *Journal of Controlled Release* **2011**, *149*, 65.

(11) Mandal, D. *Advances in Experimental Medicine and Biology* **2010**, 435.

(12) Mallick, K.; Witcomb, M. J. *Nanotechnology* **2010**, 225.

(13) Ghosh, P.; Han, G.; De, M.; Kim, C. K.; Rotello, V. M. *Advanced Drug Delivery Reviews* **2008**, *60*, 1307.

(14) De, M.; Ghosh, P. S.; Rotello, V. M. *Advanced Materials* **2008**, *20*, 4225.

(15) Venditti, I.; Fontana, L.; Fratoddi, I.; Battocchio, C.; Cametti, C.; Sennato, S.; Mura, F.; Sciubba, F.; Delfini, M.; Russo, M. V. *Journal of Colloid and Interface Science* **2014**, *418*, 52.

(16) Murphy, C. J.; Gole, A. M.; Stone, J. W.; Sisco, P. N.; Alkilany, A. M.; Goldsmith, E. C.; Baxter, S. C. *Accounts of Chemical Research* **2008**, *41*, 1721.

(17) Lee, C. W.; Chen, M. J.; Cheng, J. Y.; Wei, P. K. *Journal of Biomedical Optics* **2009**, *14*.

(18) Wagner, T.; Lipinski, H. G.; Wiemann, M. *Journal of Nanoparticle Research* **2014**, *16*.

(19) Yang, X. F.; Li, J.; Pei, H.; Zhao, Y.; Zuo, X. L.; Fan, C. H.; Huang, Q. *Analytical chemistry* **2014**, *86*, 3227.

(20) Lee, Y. K.; Kim, S.; Oh, J. W.; Nam, J. M. *Journal of the American Chemical Society* **2014**, *136*, 4081.

(21) Ueno, H.; Nishikawa, S.; Iino, R.; Tabata, K. V.; Sakakihara, S.; Yanagida, T.; Noji, H. *Biophysical Journal***2010**, *98*, 2014.

(22) Guffey, M. J.; Miller, R. L.; Gray, S. K.; Scherer, N. F. *Nano Letters* **2011**, *11*, 4058.

(23) Marchuk, K.; Fang, N. *Nano Letters* **2013**, *13*, 5414.

(24) Marchuk, K.; Ha, J. W.; Fang, N. *Nano Letters* **2013**, *13*, 1245.

(25) Eger, I.; Soares, M. J. *Journal of Microbiological Methods* **2012**, *91*, 101.

(26) Shah, N. B.; Dong, J. P.; Bischof, J. C. *Molecular Pharmaceutics* **2011**, *8*, 176.

(27) Su, T. Y.; Yonemaru, Y.; Yamanaka, M.; Lee, M. Y.; Lee, H.; Kawata, S.; Fujita, K.; Chu, S. W. In *Plasmonics: Metallic Nanostructures and Their Optical Properties X*; Stockman, M. I., Ed.; Spie-Int Soc Optical Engineering: Bellingham, 2012; Vol. 8457.

(28) Sun, W.; Wang, G. F.; Fang, N.; Yeung, E. S. *Analytical chemistry* **2009**, *81*, 9203.

(29) Shimizu, H.; Mawatari, K.; Kitamori, T. *Analytical chemistry* **2009**, *81*, 9802.

(30) Gu, Y.; Sun, W.; Wang, G. F.; Fang, N. *Journal of the American Chemical Society* **2011**, *133*, 5720.

(31) Gu, Y.; Di, X. W.; Sun, W.; Wang, G. F.; Fang, N. *Analytical chemistry* **2012**, *84*, 4111.

(32) Augspurger, A. E.; Stender, A. S.; Han, R.; Fang, N. *Analytical chemistry* **2014**, *86*, 1196.

(33) Sun, W.; Xiao, L.; Fang, N. *Methods in molecular biology* **2013**, *931*, 169.

(34) Luo, Y.; Sun, W.; Gu, Y.; Wang, G.; Fang, N. *Analytical chemistry* **2010**, *82*, 6675.

(35) Sun, W.; Wang, G.; Fang, N.; Yeung, E. S. *Analytical chemistry* **2009**, *81*, 9203.

(36) de la Fuente, J. M.; Berry, C. C. *Bioconjugate Chem.* **2005**, *16*, 1176.

(37) Tkachenko, A. G.; Xie, H.; Coleman, D.; Glomm, W.; Ryan, J.; Anderson, M. F.; Franzen, S.; Feldheim, D. L. *Journal of the American Chemical Society* **2003**, *125*, 4700.

(38) Tkachenko, A. G.; Xie, H.; Liu, Y. L.; Coleman, D.; Ryan, J.; Glomm, W. R.; Shipton, M. K.; Franzen, S.; Feldheim, D. L. *Bioconjugate Chemistry* **2004**, *15*, 482.

(39) Xu, Z. P.; Zeng, Q. H.; Lu, G. Q.; Yu, A. B. *Chemical Engineering Science* **2006**, *61*, 1027.

(40) Feng, J. J.; Zhao, G.; Xu, J. J.; Chen, H. Y. *Analytical Biochemistry* **2005**, *342*, 280.

(41) Park, S. Y.; Lytton-Jean, A. K. R.; Lee, B.; Weigand, S.; Schatz, G. C.; Mirkin, C. A. *Nature* **2008**, *451*, 553.

(42) Nam, J. M.; Park, S. J.; Mirkin, C. A. *Journal of the American Chemical Society* **2002**, *124*, 3820.

(43) Heitz, F.; Morris, M. C.; Divita, G. *British Journal of Pharmacology* **2009**, *157*, 195.

(44) Galzie, Z.; Kinsella, A. R.; Smith, J. A. *Biochemistry and Cell Biology* **1997**, *75*, 669.

(45) Nishimura, T.; Nakatake, Y.; Konishi, M.; Itoh, N. *Biochimica et biophysica acta* **2000**, *1492*, 203.

(46) Presta, M.; Dell'Era, P.; Mitola, S.; Moroni, E.; Ronca, R.; Rusnati, M. *Cytokine & Growth Factor Reviews* **2005**, *16*, 159.

(47) Powers, C. J.; McLeskey, S. W.; Wellstein, A. *Endocr-Relat Cancer* **2000**, *7*, 165.

(48) Wesche, J.; Haglund, K.; Haugsten, E. M. *Biochemical Journal* **2011**, *437*, 199.

(49) Khnykin, D.; Troen, G.; Berner, J. M.; Delabie, A. *The Journal of Pathology* **2006**, *208*, 431.

(50) Rohrer, B.; Tao, J.; Stell, W. K. *Neuroscience* **1997**, *79*, 775.

(51) Zhang, J.; Postovit, L. M.; Wang, D.; Gardiner, R. B.; Harris, R.; Abdul, M.; Thomas, A. *Nanoscale research letters* **2009**, *4*, 1297.

(52) Huang, Y.-C.; Yang, Y.-T. *Journal of Tissue Engineering and Regenerative Medicine* **2013**, n/a.

(53) Morotomi, T.; Wada, M.; Uehara, M.; Enjo, M.; Isogai, N. *Cells Tissues Organs* **2012**, *196*, 398.

(54) Lee, H.; Cusick, R. A.; Browne, F.; Kim, T. H.; Ma, P. X.; Utsunomiya, H.; Langer, R.; Vacanti, J. P. *Transplantation* **2002**, *73*, 1589.

(55) Szlachcic, A.; Pala, K.; Zakrzewska, M.; Jakimowicz, P.; Wiedlocha, A.; Otlewski, J. *International Journal of Nanomedicine* **2012**, *7*, 5915.

(56) Yayon, A.; Klagsbrun, M.; Esko, J. D.; Leder, P.; Ornitz, D. M. *Cell* **1991**, *64*, 841.

(57) Pasquale, E. B.; Singer, S. J. *Proceedings of the National Academy of Sciences of the United States of America* **1989**, *86*, 5449.

(58) Houssaint, E.; Blanquet, P. R.; Championarnaud, P.; Gesnel, M. C.; Torriglia, A.; Courtois, Y.; Breathnach, R. *Proceedings of the National Academy of Sciences of the United States of America* **1990**, *87*, 8180.

(59) Keegan, K.; Meyer, S.; Hayman, M. J. *Oncogene* **1991**, *6*, 2229.

(60) Partanen, J.; Makela, T. P.; Eerola, E.; Korhonen, J.; Hirvonen, H.; Claessonwelsh, L.; Alitalo, K. *The EMBO Journal* **1991**, *10*, 1347.

(61) Laurence, D.; Vivien, O.; Rachel, N. B.; Alison, B.; Ian, A. P.; Brahim, L.; David, G. F. *PLoS Biology* **2012**, *10*.

(62) Jessberger, S.; Gage, F. H. *Trends in pharmacological sciences* **2009**, *30*, 61.

(63) Steger, K.; Tetens, F.; Seitz, J.; Grothe, C.; Bergmann, M. *Histochemistry and Cell Biology* **1998**, *110*, 57.

(64) Wakulich, C.; Jackson-Boeters, L.; Daley, T. D.; Wysocki, G. P. *Oral Surgery, Oral Medicine, Oral Pathology, Oral Radiology, and Endodontology* **2002**, *93*, 573.

(65) Schlessinger, J.; Plotnikov, A. N.; Ibrahimi, O. A.; Eliseenkova, A. V.; Yeh, B. K.; Yayon, A.; Linhardt, R. J.; Mohammadi, M. *Molecular Cell*, *6*, 743.

(66) Raboudi, N.; Julian, J.; Rohde, L. H.; Carson, D. D. *Journal of Biological Chemistry* **1992**, *267*, 11930.

(67) Fernig, D. G.; Gallagher, J. T. *Progress in Growth Factor Research* **1994**, *5*, 353.

(68) Oh, J. S.; Recknor, J. B.; Recknor, J. C.; Mallapragada, S. K.; Sakaguchi, D. S. *Journal of Biomedical Materials Research Part A* **2009**, *91A*, 575.

(69) Wissink, M. J. B.; Beernink, R.; Poot, A. A.; Engbers, G. H. M.; Beugeling, T.; van Aken, W. G.; Feijen, J. *Journal of Controlled Release* **2000**, *64*, 103.

(70) Kimura, Y.; Hokugo, A.; Takamoto, T.; Tabata, Y.; Kurosawa, H. *Tissue Engineering Part C: Methods* **2008**, *14*, 47.

(71) Zhang, J.; Gardiner, R. B.; Mumin, A.; Harris, R. *MRS Online Proceedings Library* **2008**, *1132*, null.

(72) Ryu, W. H.; Huang, Z. N.; Prinz, F. B.; Goodman, S. B.; Fasching, R. *Journal of Controlled Release* **2007**, *124*, 98.

(73) Kusanagi, M.; Matsui, O.; Sanada, J.; Ogi, T.; Takamatsu, S.; Zhong, H.; Kimura, Y.; Tabata, Y. *Journal of Endovascular Therapy* **2007**, *14*, 785.

(74) Itoh, Y.; Matsusaki, M.; Kida, T.; Akashi, M. *Biomacromolecules* **2008**, *9*, 2202.

(75) Hirai, K.; Sakai, Y.; Kubo, H.; Tabata, Y.; Yamamoto, M. *The Effects of the Fibroblast Growth Factor with a Sustained Release Method on Wound Healing in Intestinal Anastomoses*; Medimond S R L: 40128 Bologna, 2010.

(76) Mohammadi, M.; McMahon, G.; Sun, L.; Tang, C.; Hirth, P.; Yeh, B. K.; Hubbard, S. R.; Schlessinger, J. *Science* **1997**, *276*, 955.

(77) Sun, L.; McMahon, G. *Drug Discovery Today* **2000**, *5*, 344.

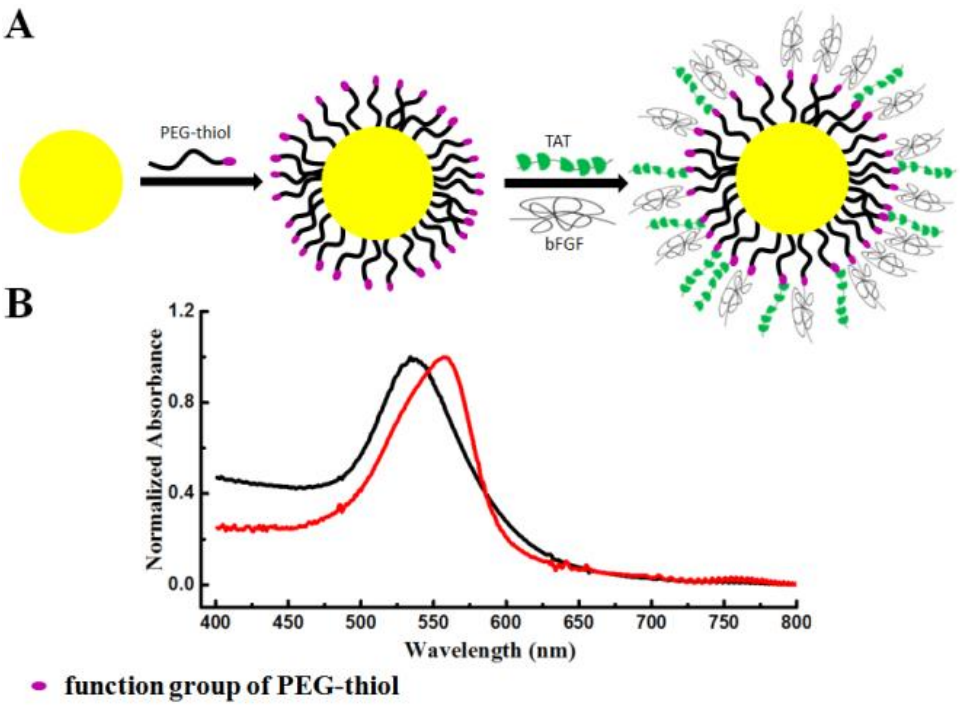

Figure 1.Surface modification of AuNPs. (A) Scheme of two-step functionalization of AuNPs with PEG-NHS disulfide, TAT, and bFGF. The scheme is not drawn to scale. (B) UV-Vis spectrum of 60-nm AuNPs (black) and bFGF-TAT-AuNPs (red).

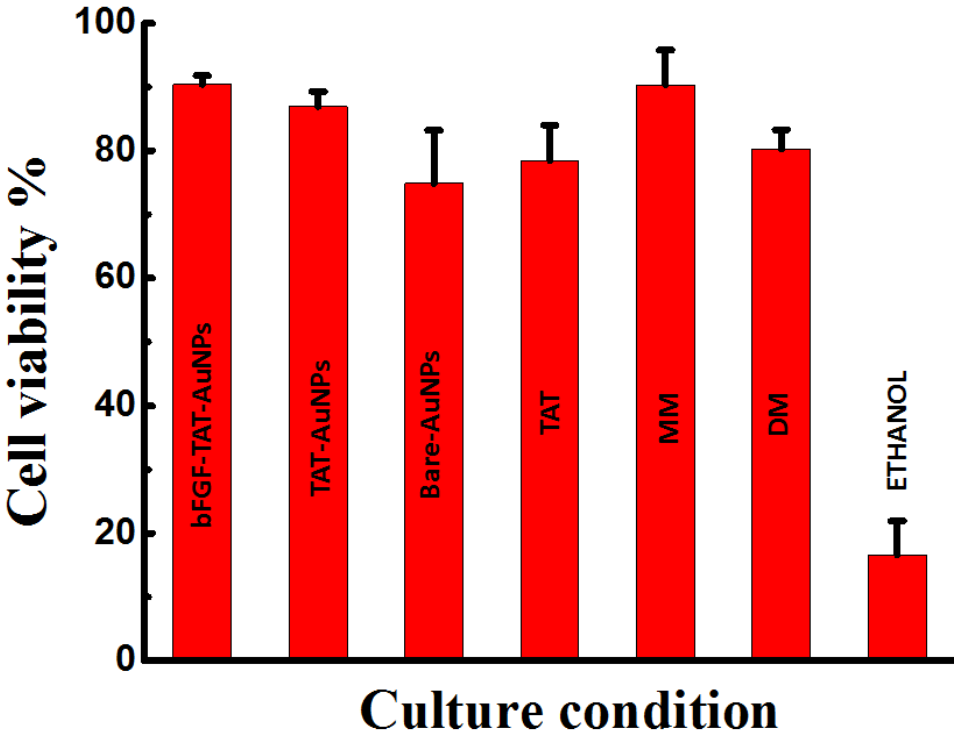

Figure 2.bFGF-TAT-AuNPs cytotoxicy experiment. AHPCs cultured in various conditions for two days in three parallel trials. Initial cell viability showed the AuNPs good compatibility with AHPCs.

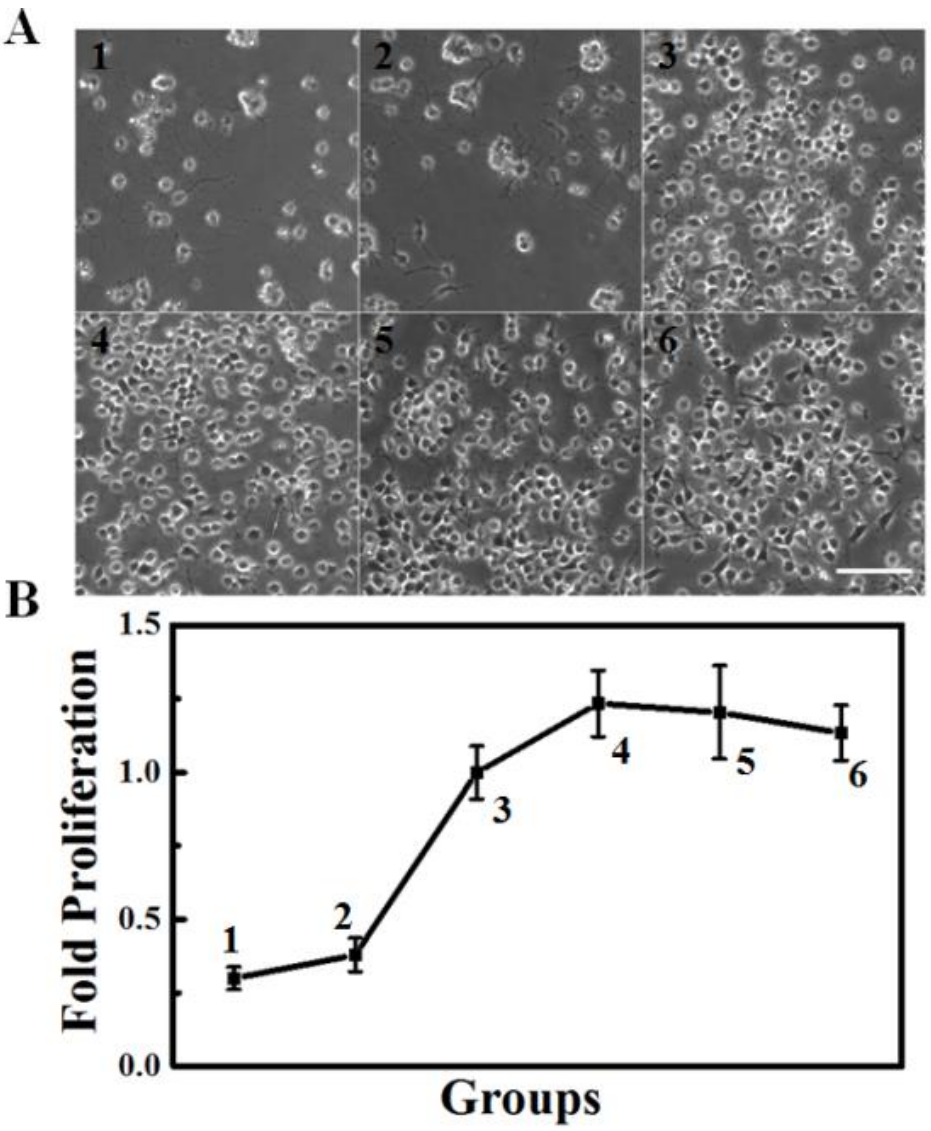

Figure 3.Optimize concentration of bFGF-TAT-AuNPs cultured with AHPCs. A) 1, 2, 3, 4, 5 and 6 showed the images of cell cultured with bFGF-TAT-AuNPs with concentration of 0.001×, 0.01×, 0.1×, 1×, 2×, 5×fold of 5μL bFGF-TAT-AuNPs to culture dish respectively. B) Statics cell numbers in the 6 groups in A. Results are analyzed from 4 trials.

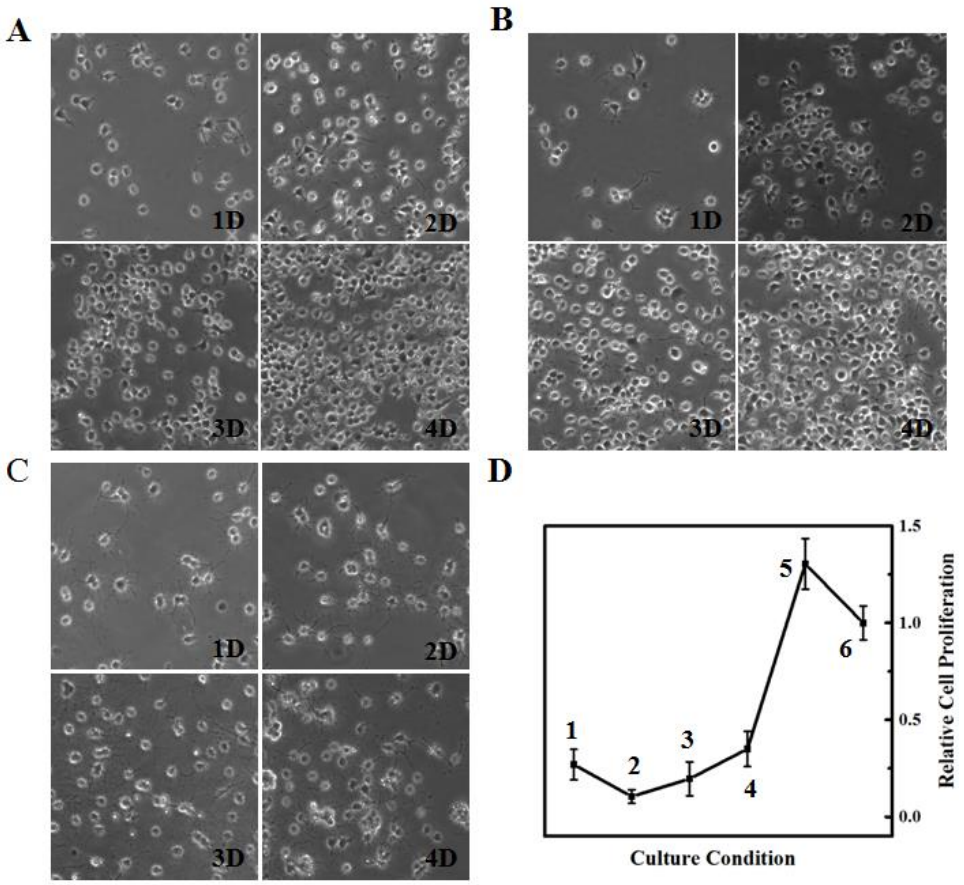

Figure 4. A, B and C are images of cells cultured with MM, bFGF-TAT-AuNPs, and DM cell culture medium respectively in four days. D) Statics of cell numbers at the fourth day, cultured with TAT, bare AuNPs, TAT-AuNPs, DM, bFGF-TAT-AuNPs and MM cell culture medium labeled with 1, 2, 3, 4, 5, and 6. All the data were analyzed from four trials.

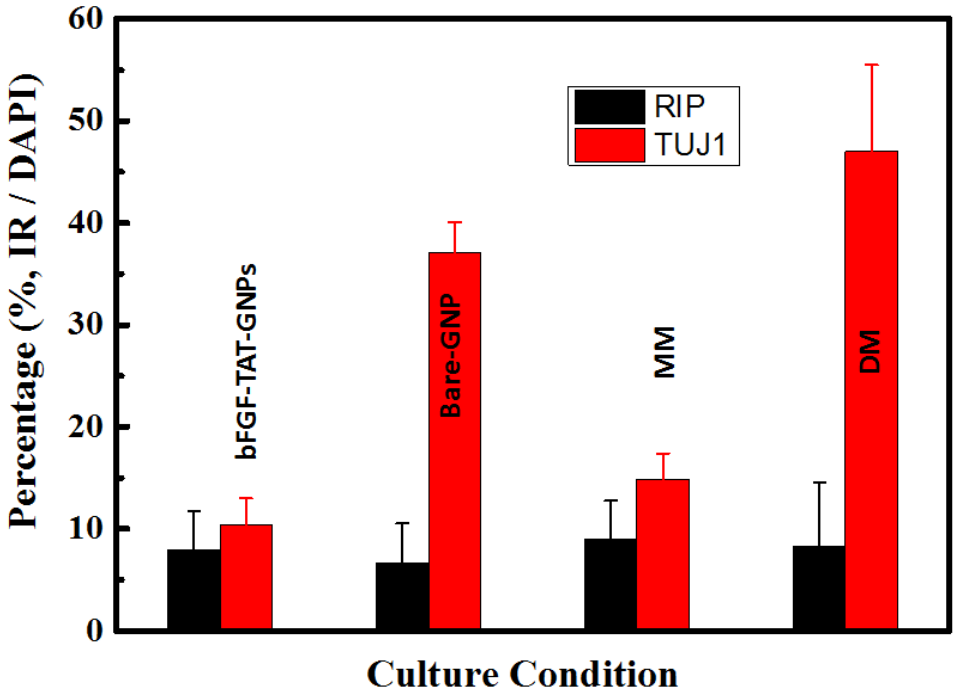

Figure 5.Differentiation of AHPCs in various culture groups. Bare AuNPs and DM group had no bFGF. Amount of bFGF in bFGF-TAT-AuNPs was 1/10 of bFGF amount in MM group.

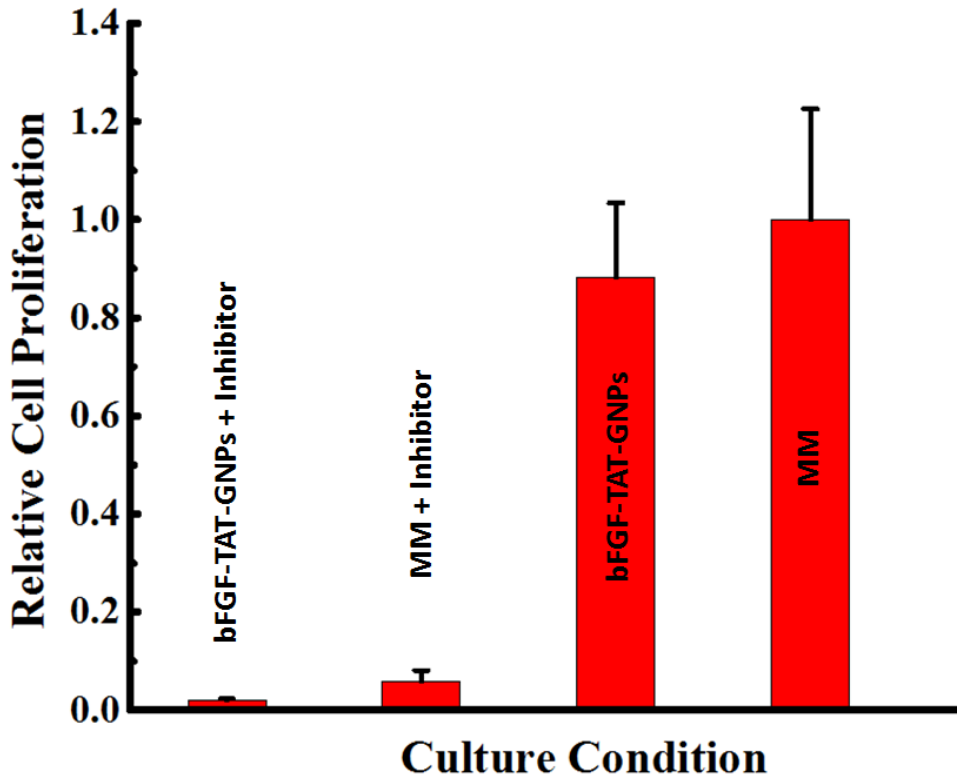

Figure 6. AHPCs co-cultured with FGF receptor inhibitor.

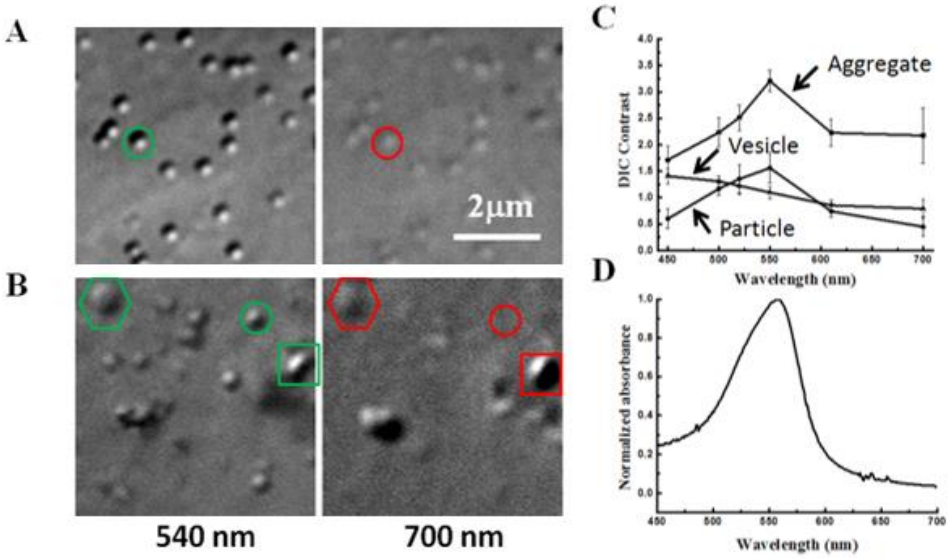

Figure 7. DIC images and contrast spectra of AuNPs, vesicles and aggregates. A and B are image of AuNPs(circle), vesicles (hexagon) and aggregates (square) on glass surface and in cell at 540 nm, and 700 nm. C) DIC contrast spectra of AuNPs, vesicles and aggregates. D) bFGF-TAT-AuNPs UV-Vis spectrum.

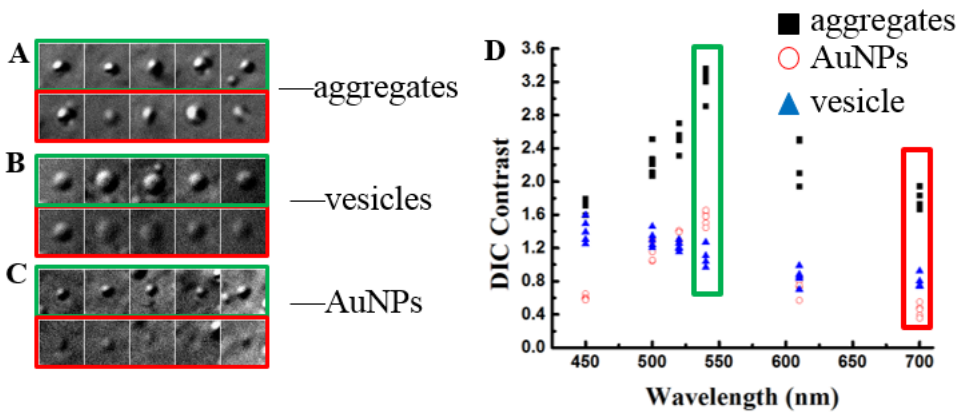

Figure 8. Five examples of A) aggregates, B) vesicle and C) AuNPs, at 540 nm (green) and 700 nm (red) in live AHPCs. D) DIC contrast spectrum of the images shown in A), B) and C) were arranged in one column for comparison.

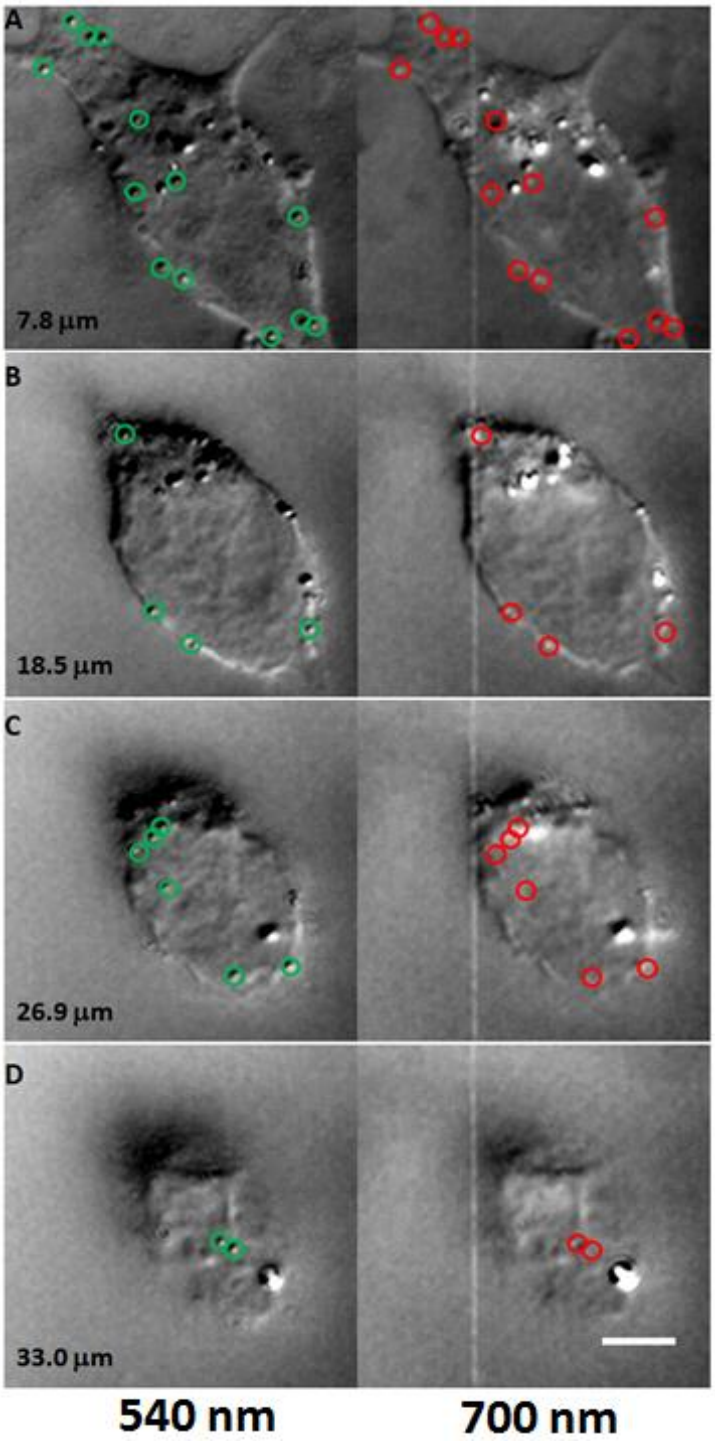

Figure 9.AuNPs counting in AHPCs. The depth showed in the left corner of each image. Total AuNPs in this cell is 35.

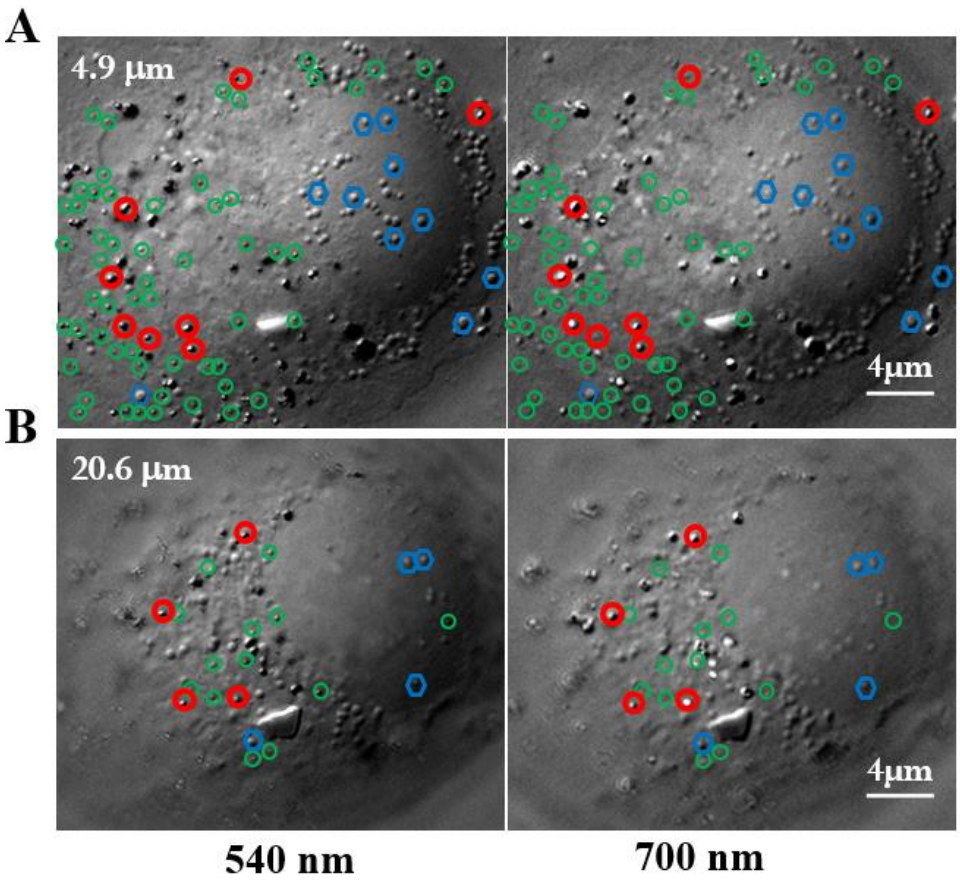

Figure 10. Images of AuNPs (green circle), aggregates (bold red circle), and vesicle (bold blue hexagon) in live AHPCs at depth A) 4.9 mm, and B) 20.6 mm in 540 nm and 700 nm.

CHAPTER 4. GEOMETRY-ASSISTED THREE-DIMENSIONAL SUPER-LOCALIZATION IMAGING OF SINGLE MOLECULE CATALYSIS ON MODULAR MULTILAYER NANOCATALYSTS

Rui Han, Ji Won Ha, Chaoxian Xiao, Yuchen Pei, Zhiyuan Qi, Bin Dong, Wenyu Huang, and Ning Fang

A paper to be submitted

Abstract

To establish structure-catalytic property relationships of heterogeneous catalysts, a detailed characterization of the three-dimensional (3D) distribution of active sites on a single catalyst is essential. Herein, we present single-particle catalysis of a modular multilayer catalytic platform that consists of a solid silica core, a mesoporous silica shell, and uniformly distributed Pt nanoparticles sandwiched in between these layers. We report on the first 3D high-resolution super-localization imaging of single fluorescent molecules produced at active sites on the core-shell model nanocatalysts. The 3D mapping is aided by the well-defined geometry and a correlation study in scanning electron microscopy and total internal reflection fluorescence and scattering microscopy. This approach can be generalized to study other nano- and mesoscale structures.

Introduction

Heterogeneous catalysis has been studied extensively by various surface science techniques on single crystal surfaces.[1-3] Many understandings have been achieved about the structure of active sites and the catalytic reaction mechanisms. However, most catalysts used in industry are metal nanoparticles (NPs) supported on three-dimensional (3D) porous supports.[4-6] The techniques that

can be used to understand the distribution of active sites on these 3D supports are very limited, especially if the characterization has to be carried out under reaction conditions.

High-resolution electron tomography is the most broadly used technique in measuring the distribution of metal NPs in 3D supports. For example, within individual Zeolite Y particles, the numbers, size distributions, and interparticle distances of Pt particles have been characterized.[7] The heterogeneities of Pt loading in the zeolite were discovered to vary up to a factor of 35 between different zeolite crystals, which clearly demonstrated the importance of catalyst preparation and characterization. Electron tomography was also able to measure the location and size distribution of Pd NPs on and inside carbon nanotubes of different internal diameters.[8]

Recent developments of *in situ* transmission electron microscopy (TEM) have opened up exciting new opportunities to acquire fundamental understanding of reaction mechanisms of heterogeneous catalysis.[9,10] However, its applicability is still greatly limited by technical challenges, such as the use of sophisticated sample holders, strict restrictions on experimental conditions, inability to capture chemical information of reagents and products, and relatively slow speed to carry out tomography scans.

In order to study the activity, selectivity, and mechanism of action of single nanocatalysts under real life *operando* conditions, single-molecule super-localization fluorescence microscopy has been employed to map individual fluorogenic turnover events on single nanocatalysts with nanoscale localization precision in the two-dimensional (2D) horizontal plane.[11-20] This fluorescence super-resolution mapping technique is advantageous over other spectroscopic techniques, such as electrochemical detection[21] and surface plasmon spectroscopy,[22,23] for acquiring detailed information on single nanocatalysts. Recent investigations have led to better understanding of the effects of facets,[11,24] defects,[16] and photogenerated reactive sites (electrons

and holes)[17] in single nanocatalysts. However, the 3D super-resolution mapping on single nanocatalysts is still elusive because the axial localization precision[25] (typically >50 nm) is often insufficient to resolve the axial distribution of fluorescent events on single nanocatalysts of up to a few hundred nanometers high.

In this communication, we report the first 3D super-resolution mapping of catalytic activities in a model multilayer catalytic platform under reaction conditions. This model platform (Figure 1A), which consists of Pt NPs sandwiched between an optically-transparent solid SiO_2 core (~200 nm in diameter) and a mesoporous SiO_2 shell (SiO_2@Pt@mSiO_2),[26] resembles the nanostructures of many intensively-investigated high-performance core-shell nanocatalysts.[27-34]

Results and Discussion

This type of multilayer nanocatalysts are attractive heterogeneous model catalysts for the following reasons: First, the catalytic activity can be tuned readily by controlling the number of the supported metal NPs. Second, the outer SiO_2 mesoporous shells isolate the catalytically active metal NPs and protect them from the possibility of sintering during catalytic reactions at high temperatures, while allowing reactant molecules to approach the surface of metal NPs through the pores. Third, spherical nanocatalysts can be employed as a 3D multilayer catalytic platform for systematic investigations to understand the factors (size, structure, molecular transport, etc.) affecting their catalytic properties and efficiency. There have been no reports to study the catalytic behavior of this type of multilayer nanocatalysts at the single-particle level. In this context, it is highly desirable to go beyond the averaging inherent in ensemble experiments and reveal catalytic properties of individual nanocatalysts during catalytic reactions.

The multilayer SiO_2@Pt@mSiO_2 nanocatalysts used in this study were synthesized according to literature procedures (see details in the Supporting Information, Figure S1).[26] As shown in Figure 1A, the Pt NPs with a diameter of 3.6 ± 0.7 nm are sandwiched between a SiO_2 sphere with an average diameter of 200 ± 20 nm and a SiO_2 shell with an average thickness of ~10 nm. SiO_2 was chosen as both core and shell material because it has excellent thermal stability, tunable surface functionality, and optical transparency in the UV-visible range. The UV-visible absorption spectra of the multilayer nanocatalysts and the SiO_2 spheres are shown in Figure S2. A peak is observed at around 275 nm in Figure S2A because of the presence of Pt NPs.[35]

To investigate the catalytic activity of the multilayer nanocatalysts, we used the fluorogenic oxidation reaction of non-fluorescent amplex red (10-acetyl-3,7-dihydroxyphenoxazine) to produce highly fluorescent resorufin (λ_{ex} = 563 nm; λ_{em} = 587 nm, at pH 7.5) at the single-molecule level (Figure 1B).[17] A sample slide was prepared by spin-casting the nanocatalyst solution on a poly-L-lysine functionalized fused quartz slide. The concentration of the nanocatalysts immobilized on the fused quartz slide was controlled to be ~1 μm^{-2} for single-particle catalysis. Two pieces of double-sided tape with a thickness of 25 μm were used as spacer between the fused quartz slide and a glass coverslip to form a sample flow chamber.

Single molecule imaging experiments were carried out under a prism-type total internal reflection (TIR) fluorescence microscope (Figure S3).[36] An evanescent field is created when the total internal reflection of an incident laser beam occurs at the solid/liquid interface. The evanescent field intensity decays exponentially with the vertical distance (up to a few hundred nanometers) from the interface.[37] This unique home-built prism-type TIR fluorescence microscope is capable of finding the optimum incident angle automatically by scanning a range of angles at intervals as small as 0.2°.[36] The optimum incident angle in our experiments was found to be ~68°,

which was close to the critical angle of 66° for the fused quartz/water interface, to result in a deep penetration depth and the highest possible signal-to-noise ratio (S/N) for single molecule detection.

A 532-nm green laser was used to excite the fluorescent resorufin product. Before initiating the fluorogenic oxidation reaction, the 532-nm laser beam was first shined onto the sample for 20 min to remove possible fluorescent dusts and impurities. Then the reactant-containing solution (0.4 μM amplex red, 20 mM H_2O_2, and 50 mM pH 7.5 phosphate buffer) was introduced over the nanocatalysts in the sample flow chamber. Fluorescent resorufin molecules were formed at many possible reactive Pt NPs on single nanocatalysts (Figures 1C and S4A) and detected by an electron multiplying charge-coupled device (EMCCD) camera. These experiments clearly demonstrated the nanocatalyst's activity for the fluorogenic reaction at the single-particle level.

We recorded movies of stochastic fluorescence bursts at many localized spots on the fused quartz surface with a temporal resolution of 100 ms. Figure 1D shows a segment of a typical fluorescence intensity trajectory from one spot highlighted in the orange frame in Figure 1C containing stochastic fluorescence ON-OFF signals. Each burst corresponds to a single resorufin molecule. It is evident in Figure 1D that these fluorescence bursts vary significantly in intensity with the S/N ranging from 3 to 12. This can be ascribed primarily to different vertical positions of these resorufin molecules on the surface of a 200-nm spherical nanocatalyst within the evanescent field, which extends only a few hundred nanometers into the sample.

The fluorescence image of a single resorufin molecule during one burst spreads over a few pixels as a point spread function (PSF) (Figure S4A). The center position of this PSF can be determined by 2D Gaussian fitting of its fluorescence profile (Figure S4B). The localization precision is typically in the range of a few nanometers to tens of nanometers depending on the signal to noise ratios (S/N) of individual fluorescence bursts. In addition, in order to correct for

sample drifting, two red-fluorescent beads with a diameter of 100 nm were used as position marker (Figures S4A and S5).

This commonly used localization method generates high-resolution 2D maps of individual turnover events on single nanocatalysts; however, it does not provide essential information related to the nanocatalysts' 3D structure. To surmount this limitation, we have made further efforts to develop a new approach for geometry-assisted 3D super-localization imaging of single fluorescent molecules in the evanescent field. The core idea is to take advantage of the uniform spherical shape of the nanocatalysts. The new approach consists of two key steps. First, the Pythagoras' theorem is used to convert 2D to 3D localization of each resorufin molecule on the nanocatalyst's spherical surface. Second, the volume intensity is used to determine whether a given product molecule is formed at the top or bottom half of a spherical nanocatalyst. (See the detailed procedure in the Supporting Information, Figure S6.)

Two sets of experiments have been performed to validate the method described above. The first set verifies that the intrinsic fluctuations in the molecular fluorescence emission do not significantly affect the accuracy in the vertical position determination. We plotted in Figure S7 the S/N distributions of resorufin molecules immobilized on a flat surface or produced catalytically on the spherical surface of the nanocatalysts under similar experimental conditions. The relative standard deviation (RSD) of the S/N distribution for the spherical surface case (~36%) is significantly larger than that for the flat surface case (~9%). The vertical distribution of resorufin molecules in the evanescent field is the main cause of this disparity, and it is also the more significant factor contributing to the recorded fluorescence intensity variations than the intrinsic fluctuations. Furthermore, it should be emphasized that the fluorescence intensity is only used to determine on which hemisphere a resorufin molecule is located, and this operation can tolerate

much larger uncertainties in the fluorescence intensity than those caused by the intrinsic fluctuations.

Another relevant point of discussion on uncertainty is about the resorufin molecules located in the middle section (equator) of a spherical nanocatalyst. These molecules have to be treated as one group because of the lack of resolving power to decide whether they are actually above or below the equator. The width of this middle section is estimated to be roughly ±10 nm when the RSD of the fluorescence intensity fluctuations is set to 10%. The complete analysis at different incident angles and intensity fluctuations can be found in the Supporting Information.

The second set of experiments was a correlation study of same nanocatalysts in scanning electron microscopy (SEM), TIR scattering microscopy, and TIR fluorescence microscopy (Figure 2). The position and diameter of each nanocatalyst were first measured in the SEM image (Figure 2A). Then we located the same nanocatalysts in the TIR scattering mode, which was converted from the TIR fluorescence mode by simply replacing the 532-nm long-pass filter for fluorescence emission with a 532-nm band-pass filter for laser excitation in front of the EMCCD camera. The 2D Gaussian fitting method was used again here to determine the center position of each nanocatalyst in the TIR scattering image (Figure 2B). Finally, we performed the fluorogenic oxidation reaction over the same nanocatalyst sample as described earlier, and recorded a series of movies showing stochastic fluorescence bursts in the same sample area. All five nanocatalysts labelled in Figure 2 were active for the catalytic reaction as the corresponding fluorescence bursts were found in the correlated TIR fluorescence image (Figure 2C). A MATLAB program was developed to carry out the data analysis for the entire imaging area (Figure S8). Through the careful correlation study, 3D super-resolution maps of resorufin molecules on single nanocatalysts can be generated reliably and accurately.

Figure 3 shows the 3D super-resolution map of single resorufin product molecules formed on NP 4 during the catalytic reactions. The diameter of NP 4 was measured to be 240 nm from the high-magnification SEM image (Figure 3A). As expected for this nanocatalyst with a high density of Pt NPs, a large number of turnover events were recorded within ~1 h. Figure 3B shows a broad distribution of the signal intensity, which is consistent with the intensity trajectory provided in Figure 1D. In the 2D super-resolution map (Figure 3C), a circular shape can be observed with an estimated diameter of 270 nm, which is consistent with the particle diameter of 240 nm plus the uncertainties in 2D localization. The center of the circle nearly overlaps with the geometric center of the nanocatalyst obtained from the correlated TIR scattering image (Figure 2B). Finally, the 2D coordinates of the resorufin molecules were projected onto the spherical surface to generate the final 3D super-resolution map (Figure 3D).

To further demonstrate the 3D super-resolution mapping, we synthesized similar nanocatalysts but with a very low density of Pt NPs (1-5 Pt NPs per particle) (Figure 4A). We performed the same fluorogenic reaction over the low Pt loading nanocatalysts under identical experimental conditions. As shown in Figure 4B, we found two distributions of fluorescence intensity of single product molecules on a nanocatalyst.

Figure 4C shows a 2D super-resolution map of single product molecules. Two groups of the turnover events can be observed on the 2D map. It can be found from the two intensity distributions (Figure 4B) that one group (black dots with higher fluorescence intensity) is positioned at the lower side of this nanocatalyst while the other group (red dots with lower fluorescence intensity) is located at the upper side. The observation of the two intensity groups serves as another piece of evidence that the fluorescence intensity can be used as the secondary criterion together with the primary criterion (2D location) to assign individual fluorescence bursts to the 3D spherical surface.

It can also be observed in Figure 4B that the shoulders of the two distributions overlap due to the intrinsic fluorescence fluctuations, causing common and expected uncertainty associated with single molecule imaging experiments.

Another example with three groups of localized fluorescence bursts is provided in Figure S9. These two examples clearly demonstrate the capability to conduct the 3D super-resolution mapping of single fluorescent molecules produced on a 3D nanocatalyst.

Conclusion

In conclusion, we report the first 3D super-resolution mapping of single fluorescent product molecules on single spherical multilayer nanocatalysts during catalytic oxidation reactions. The 3D imaging is aided by the nanocatalyst's well-defined geometry, a careful correlation study in SEM and TIR scattering and fluorescence microscopy, and an algorithm to convert 2D maps to 3D maps. This super-resolution mapping approach can be generalized to study other regularly-shaped nano- and mesoscale structures, if the actual shapes and dimensions can be established through correlated SEM or TEM images.

Single molecule catalysis with 3D super-localization imaging allowed us to better understand the catalytic properties and the identity of reactive sites of the multilayer nanocatalysts. Note that the SiO_2@Pt@mSiO_2 nanocatalysts are a highly modular 3D multilayer catalytic platform with controllable pore size, length, and active site location. We therefore expect that the sandwiched core-shell catalytic platform combined with the 3D super-localization imaging technique will enable us to address more fundamental challenges such as molecular transport phenomena in the porous catalytic nanostructures. Further studies to clarify the catalytic efficiency and characteristic

molecular transport phenomena in terms of the thickness of a shell and the size of pores in the highly modular catalytic platform are underway.

Acknowledgement

This work was supported by U.S. Department of Energy, Office of Basic Energy Sciences, Chemical Sciences, Geosciences, and Biosciences Division. The Ames Laboratory is operated for the U.S. Department of Energy by Iowa State University under contract no. DE-AC02-07CH11358.

References

(1) Sachtler, J. W. A.; Somorjai, G. A. *Journal of Catalysis* **1983**, *81*, 77.

(2) Zaera, F.; Somorjai, G. A. *Journal of the American Chemical Society* **1984**, *106*, 2288.

(3) Cremer, P. S.; Su, X. C.; Shen, Y. R.; Somorjai, G. A. *Journal of the American Chemical Society* **1996**, *118*, 2942.

(4) Iglesias-Juez, A.; Beale, A. M.; Maaijen, K.; Weng, T. C.; Glatzel, P.; Weckhuysen, B. M. *Journal of Catalysis* **2010**, *276*, 268.

(5) Barghi, B.; Fattahi, M.; Khorasheh, F. *Reaction Kinetics and Catalysis Letters* **2012**, *107*, 141.

(6) Thavornprasert, K.; Menorval, B. d. l. G. d.; Capron, M.; Gornay, J.; Jalowiecki-Duhamel, L.; Secordel, X.; Cristol, S.; Dubois, J. L.; Dumeignil, F. *Biofuels* **2012**, *3*, 25.

(7) Zecevic, J.; van der Eerden, A. M. J.; Friedrich, H.; de Jongh, P. E.; de Jong, K. P. *ACS Nano* **2013**, *7*, 3698.

(8) Ersen, O.; Werckmann, J.; Houllé, M.; Ledoux, M.-J.; Pham-Huu, C. *Nano Letters* **2007**, *7*, 1898.

(9) Harutyunyan, A. R.; Chen, G.; Paronyan, T. M.; Pigos, E. M.; Kuznetsov, O. A.; Hewaparakrama, K.; Kim, S. M.; Zakharov, D.; Stach, E. A.; Sumanasekera, G. U. *Science* **2009**, *326*, 116.

(10) Yoshida, H.; Kuwauchi, Y.; Jinschek, J. R.; Sun, K.; Tanaka, S.; Kohyama, M.; Shimada, S.; Haruta, M.; Takeda, S. *Science* **2012**, *335*, 317.

(11) Roeffaers, M. B. J.; Sels, B. F.; Uji-i, H.; De Schryver, F. C.; Jacobs, P. A.; De Vos, D. E.; Hofkens, J. *Nature* **2006**, *439*, 572.

(12) De Cremer, G.; Sels, B. F.; De Vos, D. E.; Hofkens, J.; Roeffaers, M. B. J. *Chemical Society Reviews* **2010**, *39*, 4703.

(13) Chen, P.; Zhou, X.; Shen, H.; Andoy, N. M.; Choudhary, E.; Han, K.-S.; Liu, G.; Meng, W. *Chemical Society Reviews* **2010**, *39*, 4560.

(14) Han, K. S.; Liu, G.; Zhou, X.; Medina, R. E.; Chen, P. *Nano Letters* **2012**, *12*, 1253.

(15) Xu, W.; Jain, P. K.; Beberwyck, B. J.; Alivisatos, A. P. *Journal of the American Chemical Society* **2012**, *134*, 3946.

(16) Zhou, X.; Andoy, N. M.; Liu, G.; Choudhary, E.; Han, K.-S.; Shen, H.; Chen, P. *Nature Nanotechnology* **2012**, *7*, 237.

(17) Ha, J. W.; Ruberu, T. P. A.; Han, R.; Dong, B.; Vela, J.; Fang, N. *Journal of the American Chemical Society* **2014**, *136*, 1398.

(18) Tachikawa, T.; Yonezawa, T.; Majima, T. *ACS Nano* **2012**, *7*, 263.

(19) Roeffaers, M. B. J.; De Cremer, G.; Libeert, J.; Ameloot, R.; Dedecker, P.; Bons, A.-J.; Bückins, M.; Martens, J. A.; Sels, B. F.; De Vos, D. E.; Hofkens, J. *Angewandte Chemie International Edition* **2009**, *48*, 9285.

(20) Blum, S. A. *Physical Chemistry Chemical Physics* **2014**.

(21) Xiao, X.; Pan, S.; Jang, J. S.; Fan, F.-R. F.; Bard, A. J. *The Journal of Physical Chemistry C* **2009**, *113*, 14978.

(22) Novo, C.; Funston, A. M.; Mulvaney, P. *Nature Nanotechnology* **2008**, *3*, 598.

(23) Tang, M. L.; Liu, N.; Dionne, J. A.; Alivisatos, A. P. *Journal of the American Chemical Society* **2011**, *133*, 13220.

(24) Tachikawa, T.; Yamashita, S.; Majima, T. *Journal of the American Chemical Society* **2011**, *133*, 7197.

(25) Deschout, H.; Zanacchi, F. C.; Mlodzianoski, M.; Diaspro, A.; Bewersdorf, J.; Hess, S. T.; Braeckmans, K. *Nature Methods* **2014**, *11*, 253.

(26) Xiao, C.; Maligal-Ganesh, R. V.; Li, T.; Qi, Z.; Guo, Z.; Brashler, K. T.; Goes, S.; Li, X.; Goh, T. W.; Winans, R. E.; Huang, W. *Chemsuschem* **2013**, *6*, 1915.

(27) Deng, Y.; Cai, Y.; Sun, Z.; Liu, J.; Liu, C.; Wei, J.; Li, W.; Liu, C.; Wang, Y.; Zhao, D. *Journal of the American Chemical Society* **2010**, *132*, 8466.

(28) Xu, Y.; Ma, J.; Xu, Y.; Xu, L.; Xu, L.; Li, H.; Li, H. *RSC Advances* **2013**, *3*, 851.

(29) Sekhar, A. C. S.; Meera, C. J.; Ziyad, K. V.; Gopinath, C. S.; Vinod, C. P. *Catalysis Science & Technology* **2013**, *3*, 1190.

(30) Joo, S. H.; Park, J. Y.; Tsung, C.-K.; Yamada, Y.; Yang, P.; Somorjai, G. A. *Nature Materials* **2009**, *8*, 126.

(31) Park, J.-N.; Forman, A. J.; Tang, W.; Cheng, J.; Hu, Y.-S.; Lin, H.; McFarland, E. W. *Small* **2008**, *4*, 1694.

(32) Yang, H.; Chong, Y.; Li, X.; Ge, H.; Fan, W.; Wang, J. *Journal of Materials Chemistry* **2012**, *22*, 9069.

(33) Ge, J.; Zhang, Q.; Zhang, T.; Yin, Y. *Angewandte Chemie International Edition* **2008**, *120*, 9056.

(34) Ma, Z.; Dai, S. *ACS Catalysis* **2011**, *1*, 805.

(35) Afolake, S.; Jacqueline van, M.; Chris, G. W. *Nanotechnology* **2012**, *23*, 035102.

(36) Sun, W.; Marchuk, K.; Wang, G. F.; Fang, N. *Analytical Chemistry* **2010**, *82*, 2441.

(37) Axelrod, D. In *Biophysical Tools for Biologists, Volume Two: In Vivo Techniques*; Correia, J. J., Detrich, H. W., Eds.; Academic Press: San Diego, 2008; Vol. 89, p 169.

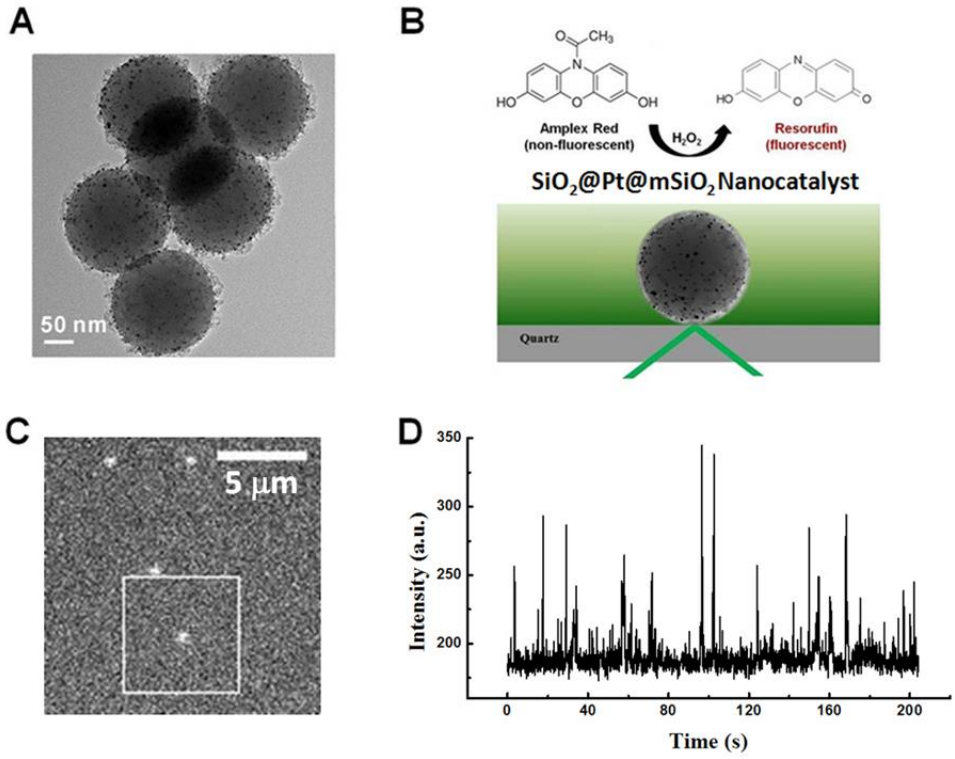

Figure 1. Single molecule catalysis of a fluorogenic oxidation reaction on single SiO_2@Pt@mSiO_2 nanocatalysts. (A) TEM image of Pt NPs confined between a SiO_2 sphere and a mesoporous SiO_2 shell. (B) Experimental scheme using total internal reflection fluorescence microscopy. Non-fluorescent amplex red is converted to highly fluorescent resorufin by a SiO_2@Pt@mSiO_2 nanocatalyst in the presence of H_2O_2. (C) Typical image of fluorescent product at localized spots during the catalytic reaction under 532-nm illumination. (D) Segment of a typical fluorescence intensity trajectory from the fluorescent spot highlighted in the orange frame in C. Temporal resolution was 100 ms.

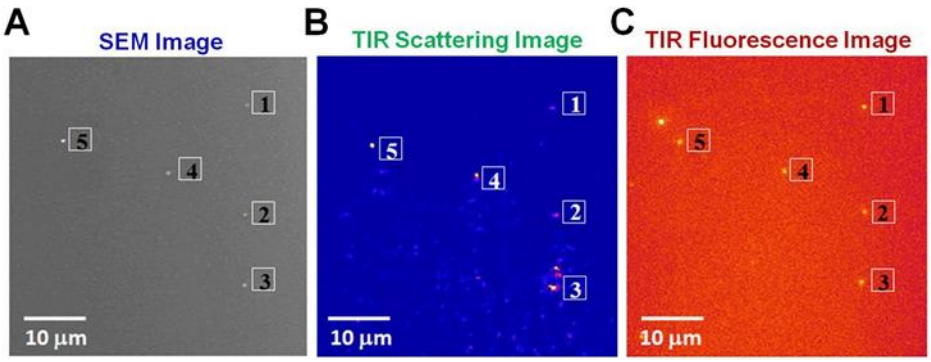

Figure 2. Correlation of SEM (A), TIR scattering (B), and TIR fluorescence (C) images of the same area showing five single SiO_2@Pt@mSiO_2 nanocatalysts (high Pt NPs loading).

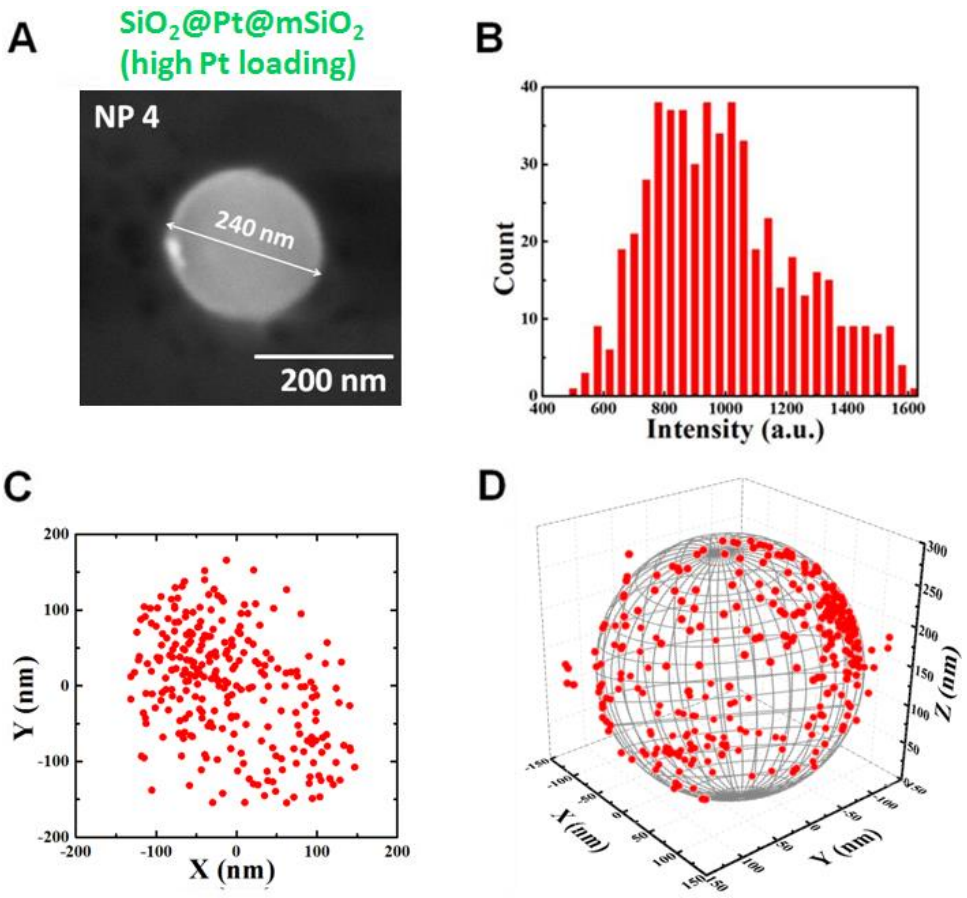

Figure 3. 3D super-localization imaging on a high Pt loading nanocatalyst. This particle is labelled as NP 4 in Figure 2. (A) High-magnification SEM image. (B) A broad fluorescence intensity distribution obtained from all the fluorescent molecules produced during a catalytic reaction. (C) 2D super-resolution map of single product molecules. The nanocatalyst's geometric center measured from the TIR scattering image is set to (0, 0). (D) 3D super-resolution map.

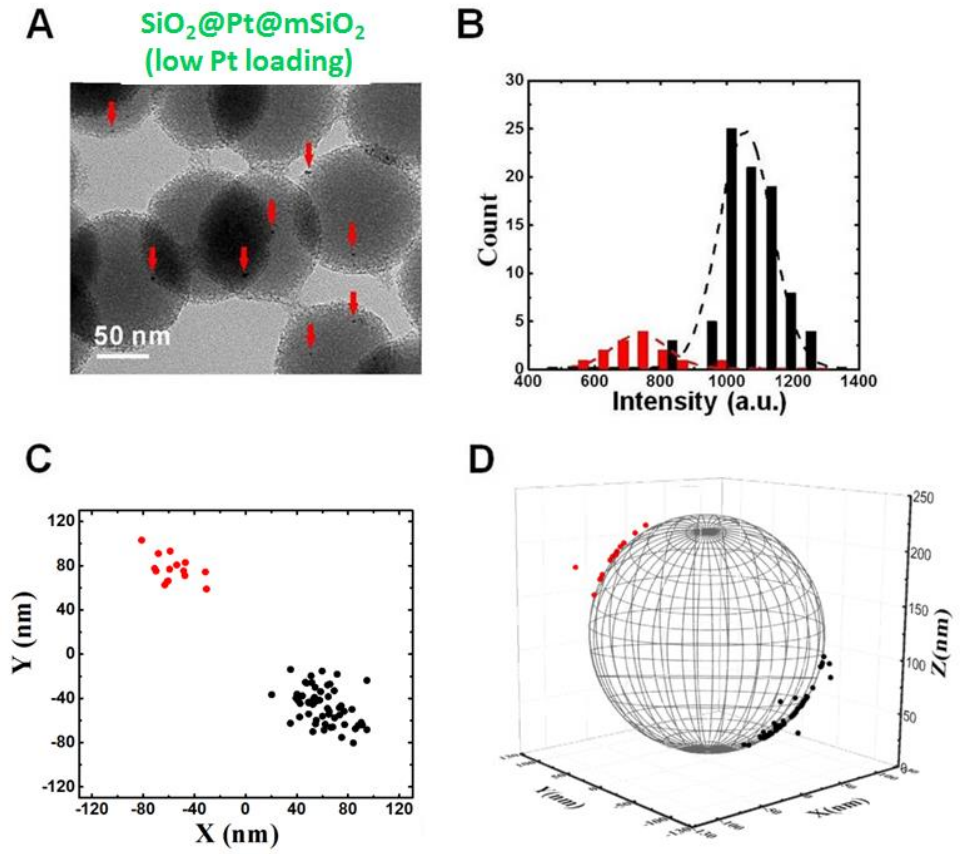

Figure 4. 3D super-localization imaging on the low Pt loading SiO_2@Pt@$mSiO_2$ nanocatalysts. (A) TEM image of the nanocatalysts. The red-arrows point out the Pt NPs. (B) Two groups of fluorescence intensity distribution. (C) 2D super-resolution map showing two separate groups on the nanocatalyst. (D) 3D super-resolution map. The nanocatalyst's diameter was estimated from the TEM image.

Supporting Information

Table of contents

1. Synthesis of Multilayer SiO_2@Pt@mSiO_2 Nanocatalysts

2. Characterization of SiO_2@Pt@mSiO_2 Nanocatalysts

3. Instrumentation for Single Molecule Fluorescence Experiments

4. Sample Preparation for Single Molecule Fluorescence Measurements

5. Single Molecule Fluorescence Measurements on SiO_2@Pt@mSiO_2 Nanocatalysts

6. Two-dimensional (2D) Super-localization of Resorufin Product Molecules

7. Sample Drift Correction during Catalytic Reactions

8. Details on Three-dimensional (3D) Super-localization Imaging

9. Signal-to-Noise Ratio Distribution of Single Resorufin Molecules on Fused Quartz Surface

10. Estimate Resolution near the Particle's Equator in the Evanescent Field

1. Synthesis of multilayer SiO_2@Pt@mSiO_2 nanocatalysts. SiO_2 spheres with an average diameter of 200(±20) nm are synthesized by using the Stöber method.[219,220] Pt nanoparticles (NPs) were synthesized by the methanol reduction of chloroplatinic acid (H_2PtCl_6) in the presence of polyvinylpyrrolidone. NH_2 groups were introduced to SiO_2 surface by polymerizing 3-aminopropyltriethoxysilane (APTS) to enhance the binding between Pt NPs and SiO_2 spheres as shown Figure S1. Finally, we used tetraethyl orthosilicate (TEOS) as the SiO_2 precursor, and hexadecyltrimethylammonium bromide (C_{16}TAB) as the templating agent to grow SiO_2 shell on the surface of the Pt-NP-loaded SiO_2 spheres.[221] Here we used 1 mol/L NaOH to etch the samples at room temperature for two hours to get a more porous shell structure to introduce a more efficient diffusion rate. After etched with NaOH, the particles were calcinated at 550 °C for 6 h to remove protection ligands on Pt NPs and in nanopores, and then the particles were reduced with H_2 flow (H_2/He = 5/45 mL/min) for 1 h to activate the surface of Pt NPs for catalysis.

2. Characterization of SiO_2@Pt@mSiO_2 nanocatalysts. In the present study, two kinds of SiO_2@Pt@mSiO_2 nanocatalysts were used: high SiO_2@Pt@mSiO_2 (high loading of Pt NPs on the silica core) and low SiO_2@Pt@mSiO_2 (low loading of Pt NPs on the silica core). The amount of Pt NPs loaded on the spherical silica core in the high SiO_2@Pt@mSiO_2 nanocatalysts was 2.5 wt%. In the low SiO_2@Pt@mSiO_2 nanocatalysts the density of Pt NPs supported on one silica core was controlled to be about 1-5 Pt NPs.

A UV-Vis spectrophotometer (Varian Cary 300) was used to characterize the optical properties of the SiO_2@Pt@mSiO_2 nanocatalysts. The absorption spectrum of SiO_2@Pt@mSiO_2 nanocatalysts is shown in Figure S2A. SiO_2 sphere's absorption spectrum is provided in Figure S2B as control. The absorption peak for Pt NPs can be detected at 275 nm for the high

SiO_2@Pt@mSiO_2 sample, while this peak disappears in the absorption spectrum for the low SiO_2@Pt@mSiO_2 sample.

3. Instrumentation for single molecule fluorescence experiments. A homebuilt prism-based total internal reflection fluorescence (TIRFM) microscope (Figure S3) was introduced to perform single molecule experiments. A Sutter MP-285 motorized 3D translational stage (Novato, CA) replaced the original microscope stage to reduce the sample drifting. An adjustable 250-mW maximum 532-nm continuous wave (CW) laser was used as the excitation source. The excitation laser beam was first pointed to a periscope, passed through a Uniblitz mechanical shutter (model LS2Z2, Vincent Associates, Rochester, NY) and a focusing lens (15-cm focal length), and then directed toward the mirror of a galvanometer optical scanner (model 6220, Cambridge Technology, Cambridge, MA). The focusing lens was used to control the laser spot size in the imaging area. The mirror galvanometer was coupled to a high precision motorized linear stage (model MAA-PP, Newport, Irvine, CA) and directed the focused laser beam through the equilateral prism to the interface at different incident angles.

4. Sample preparation for single molecule fluorescence measurements. The SiO_2@Pt@mSiO_2 nanocatalysts were spin-coated on a poly-L-lysine (Sigma, P8920) functionalized fused quartz slide (SPI, West Chester, PA) and particle density was controlled to be ~1 particle/μm^2. Then 10 µL of 100-nm fluorescent polystyrene beads (Duke Scientific, Fremont, CA; 10,000-fold dilution in ethanol from the purchased solution) was also introduced on the same fused quartz slide as reference particles.[222] The poly-L-lysine solution (0.1% w/v in H_2O) was first diluted 10-fold with DI water. The pre-cleaned fused quartz slides were immersed into the diluted poly-L-lysine solution for 10 min. Then the slides were washed with DI water and dried

with N_2 gas. At last, a flow chamber was formed by using 25-μm double side tapes as spacer between the fused quartz slide and a glass coverslip.

5. Single molecule fluorescence measurements on SiO_2@Pt@mSiO_2 nanocatalysts. Single-molecule fluorescence experiments were carried out on a prism-type total internal reflection fluorescence (TIRFM) microscope. To reduce the background noise, the flow chamber and the buffer solutions were photobleached overnight under UV light. A 532-nm CW laser beam (100 mW) was focused onto the sample to excite resorufin product. Before initiating the fluorogenic oxidation reaction, the flow chamber was left on the imaging stage for 20 min to reduce sample drift, and in the meantime, the 532-nm laser beam was turned on to remove fluorescent dusts and impurities in the sample. Then the reactant-containing solution (0.4 μM amplex red, 20 mM H_2O_2 in 50 mM pH 7.5 phosphate buffer) was introduced to the flow chamber. The fluorescence images were captured by a Plan Fluor 100x/NA 1.49 objective and Andor iXon EM+ 897 camera (Belfast, Northern Ireland; 16 μm x 16 μm pixel size, 512 × 512 imaging array). A high quality long pass 532 nm filter (532 LP, Chroma Technology Corp) was mounted in the front of camera to block the scattering signal and unwanted background. We recorded movies of stochastic fluorescence bursts at many localized spots on the fused quartz surface with a time resolution of 100 ms. The collected movies and images were analyzed by a MATLAB Gaussian peak fitting program and NIH ImageJ (http://rsbweb.nih.gov/ij/).

6. Two-dimensional (2D) super-localization of resorufin product molecules. We recorded movies of fluorescent busts at many localized spots on the fused quartz surface with the temporal resolution of 100 ms for 1 h. We then used a home-written MATLAB program to analyze a movie record. The fluorescence intensity trajectories were extracted from localized fluorescence spots individually across the entire movie. Each trajectory from a SiO_2@Pt@mSiO_2 nanocatalyst

contains many stochastic fluorescence bursts over time. We identified the corresponding image frames of each burst in the trajectory. For each burst, all image frames contributing to the fluorescence burst were combined to form a single image. We then determined the center position of the product molecule by 2D Gaussian fitting of the single image using the MATLAB program. The accuracy of the center position was determined according to Thompson and coworkers.[223] An example of 2D localization is provided in Figure S4.

7. Sample drift correction during catalytic reactions. We performed the single molecule experiment for 1h with continuously pumped fresh solution to a flow chamber. During this recording period, the stage inevitably drifted slightly. To determine the accurate center position of single resorufin molecules produced on the SiO_2@Pt@mSiO_2 nanocatalysts, it is crucial to correct sample drifting by using reference particles in the same image area as shown in Figure S4A. In the present study, we used polystyrene fluorescence beads with a diameter of 100 nm (R100, Duke Scientific Corp.) as reference particles for sample drift correction.

The common practice is to use one reference particle for sample drift correction. However, in our experiments, we discovered that the sample could also rotate slightly while sitting on the stage for hours. Therefore, it is necessary to use two reference particles. The distributions of the positions of target particles with one or two reference particles are shown in Figures S5B and S5C, respectively. The spread in Figure S5C is clearly smaller than that in Figure S5B, suggesting the corrections with two reference particles are more precise.

8. Details on three-dimensional (3D) super-localization imaging. The 3D super-localization imaging of single fluorescent molecules is shown in Figure S6. Because the emission wavelength (532 nm) is larger than the particle size (~200 nm in diameter), we can consider single molecule 2D distribution is the projection of 3D space distribution and vice versa, as shown in

Figure S6C. When the 2D distribution is projected to the nanocatalyst, each single molecule should be on or near the particle surface, by using volume intensity to distinguish the molecule is at the top semi-sphere or bottom semi-sphere, we can get the 3D location of each molecule on the particle.

There are key steps as following: 1) the center position (*a*) of a SiO_2@Pt@mSiO_2 nanocatalyst is determined first from the scattering measurement. 2) The radius (*r*) of the same SiO_2@Pt@mSiO_2 nanocatalyst was measured from the SEM images. 3) The center position (*b*) of each single product molecule is found by 2D Gaussian fitting. 4) The distance (*d*) from the particle center *a* to the molecule center *b* is calculated. 5) The height (*h*) is calculated by Pythagoras's theorem ($r^2=h^2+d^2$). 6) The volume intensity is used to determine whether the single product molecule is formed at the top (b_1) or at the bottom (b_2). Steps 3-6 are repeated for each fluorescent product molecule, and finally, a 3D super-localization map is created.

9. Signal-to-Noise ratio distribution of single resorufin molecules on fused quartz surface. We performed a control experiment to check the distribution of signal-to-noise ratio of single resorufin molecules on the fused quartz slide surface. This control experiment was performed under identical experimental conditions. Resorufin was dissolved in a phosphate buffer (pH 7.5). The concentration of the resorufin solution introduced into the flow chamber was 0.5 nM, and flow rate was set to 10 μL/min. The resorufin product (pKa = 5.8) is negatively charged in the solution with pH 7.5. Figure S7A shows a 3D plot of single resorufin molecules attached on flat fused quartz surfaces. Figure S7B shows a typical fluorescence intensity trajectory of single resorufin molecules produced during a fluorogenic catalytic reaction. Signal-to-noise ratios of single resorufin molecules on surface and single catalyzed resorufin molecules were counted to generate statistic histograms as shown in Figures S7C and S7D. A large range of signal-to-noise ratios of

single catalyzed resorufin product may be ascribed to different vertical positions of these resorufin molecules produced on a 200-nm spherical nanocatalyst in the evanescent field extending only a few hundred nanometers (typically, 200-250 nm) into the sample.

10. Estimate resolution near the particle's equator in the evanescent field. The depth of the evanescent field (d) is defined by eq. 1 for a given interface as it depends theoretically on θ, the wavelength (λ) of the incident light, and the reflective indices of the two media (fused quartz n_1=1.47 and water n_2=1.33) at the interface.

$$d(\theta) = \frac{\lambda}{4\pi\sqrt{(n_1 \sin\theta)^2 - n_2^{\,2}}} \tag{1}$$

The critical angle for this fused quartz/water interface is ~66°. The evanescent field intensity (I) exponentially decays with the vertical distance (z) from the interface and drops to 1/e of the value at the interface over the depth (d):

$$I_{(z)} = I_{(0)}\, e^{-z/d(\theta)} \tag{2}$$

Eq. 3 is derived from eq. 2 for normalized intensity.

$$z = -d(\theta) \log I_{(z)} \tag{3}$$

The error propagation can therefore be calculated with eq. 4:

$$\Delta z = 0.434 d(\theta) \frac{\Delta I_{(z)}}{I_{(z)}} \tag{4}$$

Table 1 shows the calculated Δz at various incident angles and penetration depths, when the uncertainty in single molecule fluorescence intensity at the temporal resolution of 100 ms is set to 10% ($\Delta I_{(z)} / I_{(z)} = 10\%$). The incident angle was set to around 68° to result in Δz = ~10 nm.

Table 1. Δz at various penetration depths and $\Delta I_{(z)}/I_{(z)} = 10\%$

θ(°)	$d(\theta)$ (nm)	Δz (nm)
67	264.8	11.5
68	186.0	8.1
69	152.4	6.6
70	132.89	5.8
71	119.81	5.2
73	110.3	4.8
73	103.1	4.5
74	97.5	4.2
75	92.9	4.0

Reference

(1) X.Fang, Z. L., M.-F. Hsieh, M. Chen, P. Liu, C. Chen, N. Zheng *ACS Nano* **2012**, *6*, 4434.

(2) Y. Huang, J. E. P. *Colloids Surf. A* **2010**, *360*, 175.

(3) Xiao, C.; Maligal-Ganesh, R. V.; Li, T.; Qi, Z.; Guo, Z.; Brashler, K. T.; Goes, S.; Li, X.; Goh, T. W.; Winans, R. E.; Huang, W. *ChemSusChem* **2013**, *6*, 1915.

(4) Ha, J. W.; Ruberu, T. P.; Han, R.; Dong, B.; Vela, J.; Fang, N. *Journal of the American Chemical Society* **2014**, *136*, 1398.

(5) Thompson, R. E.; Larson, D. R.; Webb, W. W. *Biophys J* **2002**, *82*, 2775.

Supporting Figures

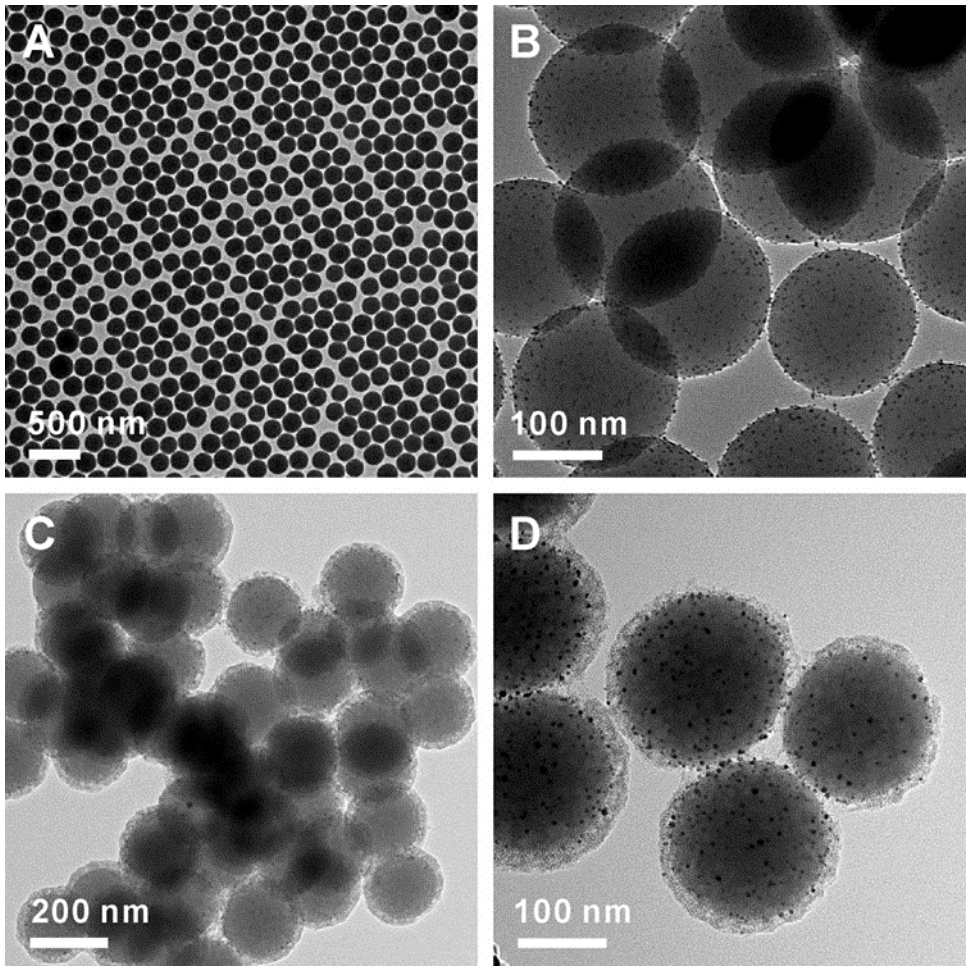

Figure S1. Synthesis of SiO_2@Pt@mSiO_2 nanocatalysts. (A) TEM image of 200(±20)-nm silica spheres. (B) TEM image of Pt NPs (2.9 ± 0.3 nm) loaded onto silica spheres. (C) SiO_2@Pt@mSiO_2 nanocatalysts after calcination and reduction. (D) A nanocatalyst showing Pt NPs confined between a SiO_2 sphere and a porous SiO_2 shell. The inset shows the size distribution of Pt nanoparticles (3.6 ± 0.7 nm) after calcination and reduction.

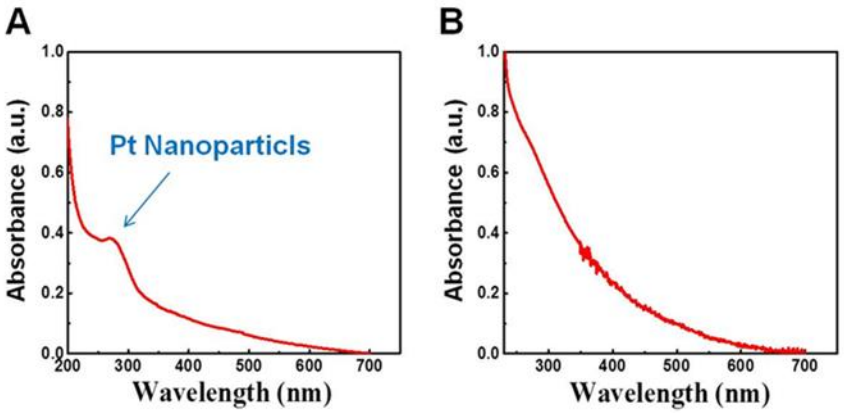

Figure S2. UV-VIS absorption spectra of the SiO_2@Pt@mSiO_2 nanocatalysts with high Pt NP loading (A) and silica spheres only (free of metal) from the same batch (B).

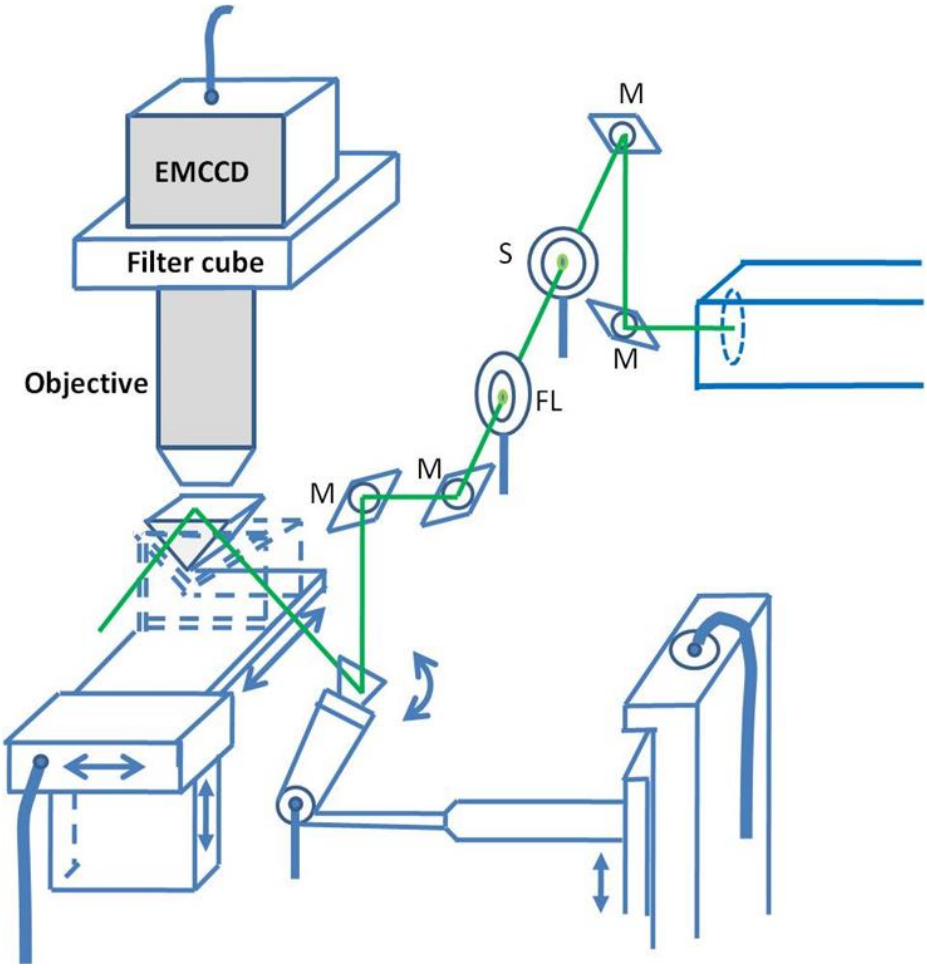

Figure S3. Schematic diagram of the automated, scanning-angle, prism-type total internal reflection microscope: M, mirror; S, mechanical shutter; FL, focusing lens.

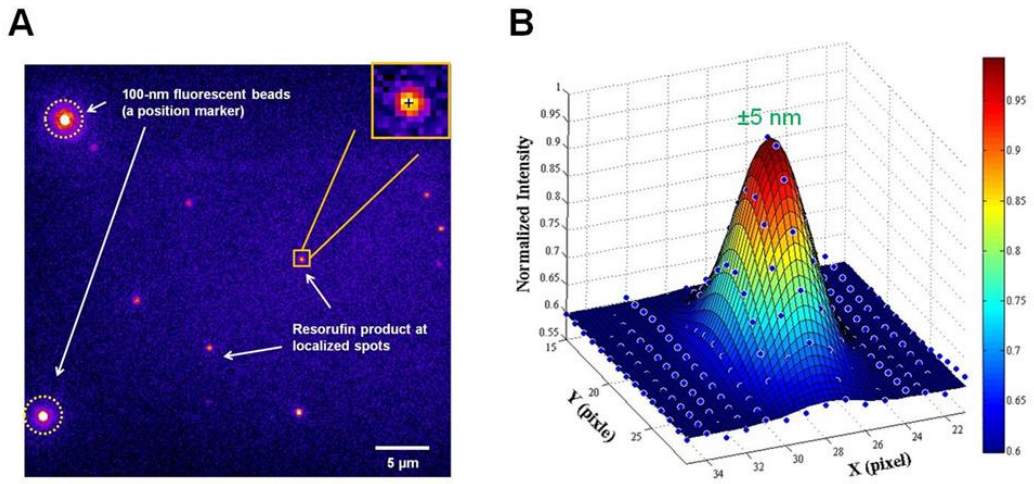

Figure S4. Determination of the center position of single product molecule. (A) A typical fluorescence image to show anchors (or position markers) and single product molecules at many localized spots. In this study, fluorescent nanoparticles (100 nm in diameter) circled with the dashed yellow were used as position markers. The center position of single product molecule was determined by 2D Gaussian fitting of its fluorescent image. (B) 3D representation of the single product molecule squared with orange in (A). The center position of this typical fluorescence image can be determined with nanometer accuracy (±5 nm). The accuracy of the center position was determined according to Thompson and co-workers (ref. 5).

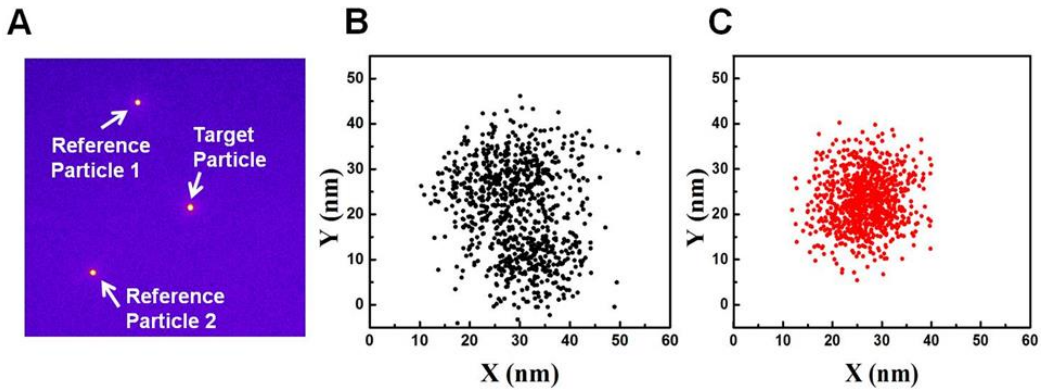

Figure S5. Correction for sample drifting by using polystyrene fluorescence beads (100 nm in diameter) as reference anchors. (A) A fluorescence image showing three fluorescent beads. (B) Distribution of the location of a target particle using one reference particle to correct for sample drifting. (C) Distribution of the location of a target particle using two reference particles to correct for sample drifting. It is evident that using two reference particles simultaneously generates more accurate and precise localization data than using only a single reference particle.

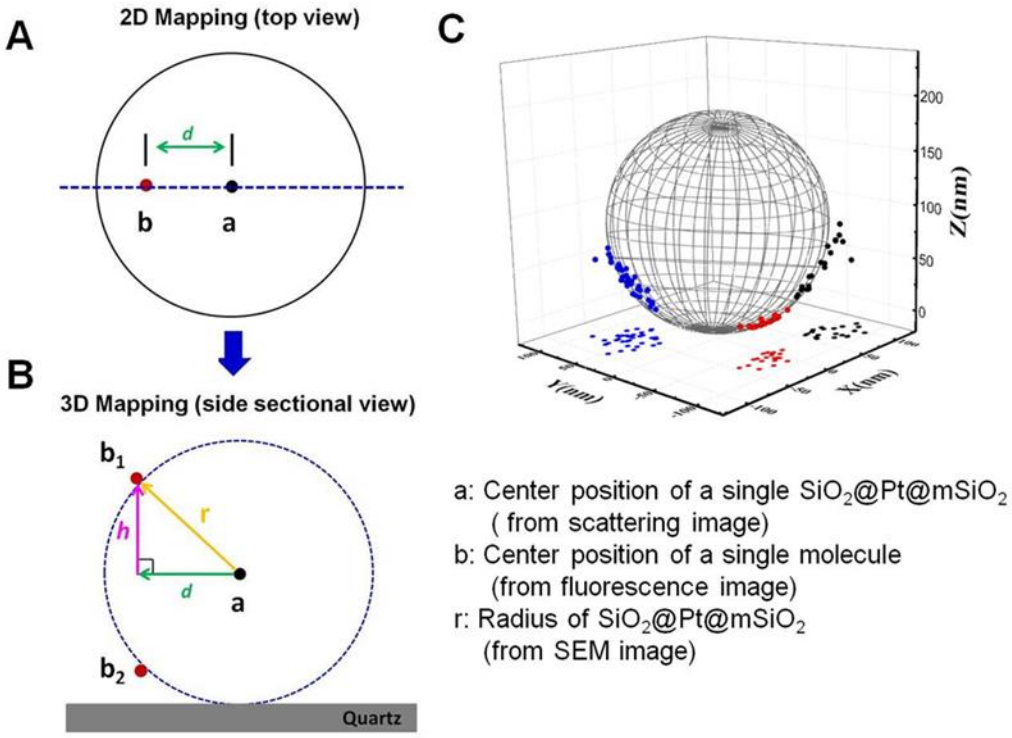

Figure S6. 3D Super-localization of single fluorescent molecules produced on a SiO_2@Pt@mSiO_2 nanocatalyst. First, we determine the 2D location of each resorufin molecule by 2D-Gaussian fitting (A). Second, we convert 2D to 3D super-localization image by using Pythagoras theorem formula (B, C). More detailed steps are as follows: 1) We determine the center position (*a*) of a single SiO_2@Pt@mSiO_2 nanocatalyst. 2) We determine a radius (*r*) of the same SiO_2@Pt@mSiO_2 nanocatalyst. 3) We locate the center position (*b*) of each single product molecule by 2D Gaussian fitting. 4) We calculate the distance (*d*) from the particle center *a* to the molecule center *b*. 5) The height (*h*) is calculated by Pythagoras theorem formula ($r^2=h^2+d^2$). 6) From the volume intensity we determine whether the single product molecule is formed at the top (b_1) or at the bottom (b_2). Therefore, we finally obtain the 3D super-localization image mapping all of the single product molecules on a spherical nanocatalyst (C).

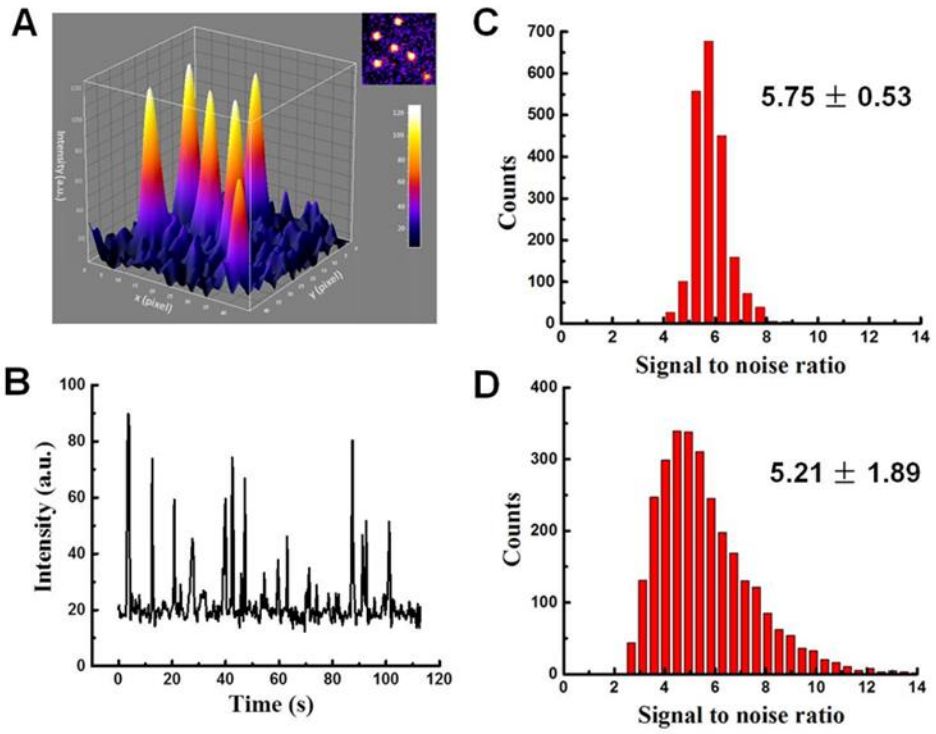

Figure S7. Signal-to-noise ratio distributions of single resorufin molecules on surface and single resorufin molecules produced during a catalytic reaction. (A) 3D surface plot of single resorufin molecules on a fused quartz surface. The inset is a 2D image of single resorufin molecules in the same area. (B) Typical fluorescence intensity trajectory of single resorufin molecules produced during a fluorogenic catalytic reaction. (C, D) Statistic distributions of signal-to-noise ratio of single resorufin molecules on a flat fused quartz surface (C) and single resorufin molecules produced on the surface of a nanocatalyst (D). The median and standard deviation for each case are 5.75 (±0.53 or 9.2%) and 5.21 (±1.89 or 36.3%), respectively. The much wider distribution of resorufin molecules on the surface of spherical nanocatalysts suggests that the vertical position is a more significant factor than the molecular fluorescence fluctuations in determining the signal-to-noise ratio.

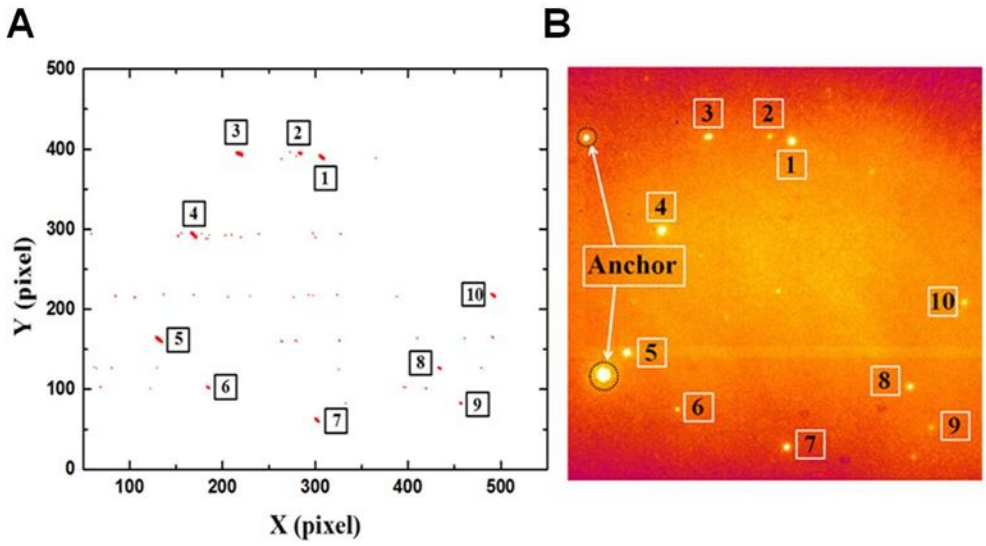

Figure S8. The data analysis using a home-made MATLAB program for 2D Gaussian fitting. (A) Super-localization of the center position of single product molecules using the automatic Gaussian fitting program. (B) The original fluorescence image used for the data analysis in (A).

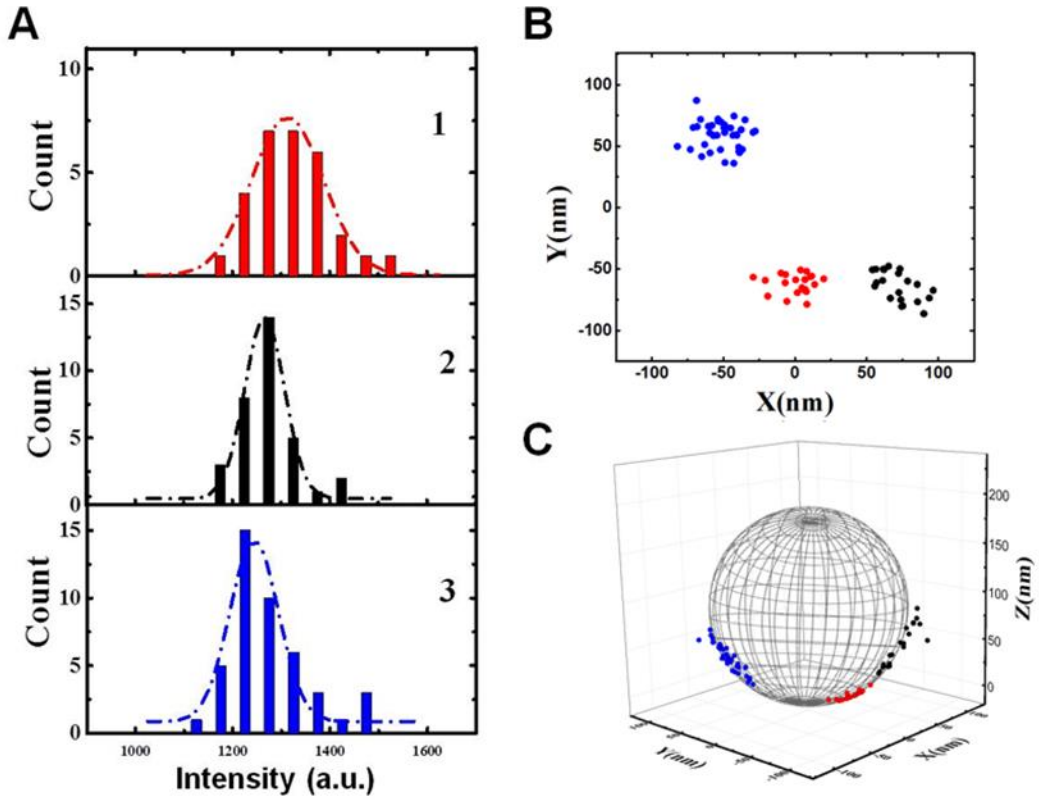

Figure S9. Another example of 3D super-localization imaging on the low SiO_2@Pt@mSiO_2 nanocatalyst. (A) Three intensity distributions of single product molecules. (B) 2D super-localization image mapping single product molecules formed on the nanocatalyst during catalytic reactions. Three separate groups are shown on the nanocatalyst. (C) 3D super-localization image of single product molecules displayed in 3D space.

CHAPTER 5. GENERAL CONCLUSIONS

Application of single molecule and single nanoparticles imaging have been studied in separation, in catalysis, in living cell based on DIC, TIRFM, epi-fluoresence microscopy in this thesis.

First, wild field microscopy-based single polystyriene beads is studied in alumina porous membrane. In this work, we measured the electrophoretic motion of individual polystyrene nanoparticles in cylindrical alumina nanopores with different size combinations. The axial diffusion of the particles in the pores is also measured. It is found that the electrophoretic mobilities and the diffusion coefficients of particles were both substantially smaller compared to those in the bulk solution, independent of particle size or pore diameter. The effective A/V ratio inside the nanopores cannot account for the difference between the two particle sizes in two different pore sizes, indicating adsorption can also be ruled out. While this phenomenon requires further investigation, we suggest that the microenvironment in the nanopores is anomalous. The electrophoretic mobility and diffusion experiments both point to the scenario that the apparent macroscopic viscosity is anomalously large in the nanopores.

Second, by using DIC microscopy, the gold nanopartricle as a carrier to delivery drug into stem cell is studied. In this work, we have presented dual-view wavelength method to indentify AuNPs, and count/locate the particles in fixed/live AHPCs cells. We also have demonstrated biocompatibility of AuNPs modified with bFGF, such as non-cytotoxity and non-immunogenicity. Furthermore, we also have shown the application of bFGF conjugated AuNPs to proliferate AHPCs as a effective drug delivery carrier, which gives us a more widely biocompatible application in live cell, such as apply functionalizing gold nanoparticles with various functions growth factor to characterize stem cells behaviors.

Last, based on a Multilayer Nanocatalysts, three-dimensional super-localization imaging of single molecule catalysis was studied. In conclusion, we report the first 3D super-resolution mapping of single fluorescent product molecules on single spherical multilayer nanocatalysts during catalytic oxidation reactions. The 3D imaging is aided by the nanocatalyst's well-defined geometry, a careful correlation study in SEM and TIR scattering and fluorescence microscopy, and an algorithm to convert 2D maps to 3D maps. This super-resolution mapping approach can be generalized to study other nano- and mesoscale structures, as long as the actual shapes and dimensions can be established through correlated SEM or TEM images. Single molecule catalysis with 3D super-localization imaging allowed us to better understand the catalytic properties and the identity of reactive sites of the multilayer nanocatalysts. Note that the SiO_2@Pt@mSiO_2 nanocatalysts are a highly modular 3D multilayer catalytic platform with controllable pore size, length, and active site location. We therefore expect that the sandwiched core-shell catalytic platform combined with the 3D super-localization imaging technique will enable us to address more fundamental challenges such as molecular transport phenomena in the porous catalytic nanostructures. Further studies to clarify the catalytic efficiency and characteristic molecular transport phenomena in terms of the thickness of a shell and the size of pores in the highly modular catalytic platform are underway.